UNIVERSITY OF CALIFORNIA SAN DIEGO

Regulation of Neuronal Network Dynamics through Ionic and Synaptic Homeostasis

A dissertation submitted in partial satisfaction of the
requirements for the degree of

Doctor of Philosophy

in

Neurosciences with a Specialization in Computational Neurosciences

by

Oscar Christian González

Committee in charge:

Professor Maxim Bazhenov, Chair
Professor James Brewer
Professor Gert Cauwenberghs
Professor Eric Halgren
Professor Duygu Kuzum
Professor Brad Voytek

2019

The Dissertation of Oscar Christian González is approved, and it is acceptable in quality and form for publication on microfilm and electronically:

Chair

University of California San Diego

2019

DEDICATION

To my niece and nephew Liliana and Gabriel González

EPIGRAPH

The world is a construct of our sensations, perceptions, memories. It is convenient to regard it as existing objectively on its own. But it certainly does not become manifest by its mere existence. It becoming manifest is conditional on very special goings-on in very special parts of this very special world, namely on certain events that happen in a brain.

Erwin Schrödinger

TABLE OF CONTENTS

LIST OF ABBREVIATIONS

4AP	4-aminopyridine
ACh	acetylcholine
ACSF	artificial cerebrospinal fluid
AED	anti-epileptic drugs
AMPA	α-amino-3-hydroxy-5-methyl-4-isoxazolepropionic acid
AQP4	aquaporin-4
Arc / Arg3.1	activity regulated cytoskeletal-associated protein
ATP	adenosine triphosphate
ATPase	adenosine triphosphatase
BBB	blood-brain-barrier
BDNF	brain derived neurotrophic factor
BOLD	blood-oxygen level-dependent signal
CamKII	calcium / calmodulin – dependent kinase II
ChETA	channelrhodopsin 2 with E123T mutation
ChR2	channelrhodopsin 2
CX43 / 30	connexin protein 43 / 30
DC	direct current
DMN	default mode network
EAAT2	excitatory amino acid transporter 2
EC	entorhinal cortex

EEG	electroencephalogram
fMRI	functional magnetic resonance imaging
GABA	γ-aminobutyric acid
$g_{D/S}$	dendritic / somatic conductance
HSP	homeostatic synaptic plasticity / scaling
HYP	hypersynchronous
I^A or I_A	A-current; transient potassium current
I^h or I_h	h-current; hyperpolarization activated depolarizing mixed cation current
I^{Int}	intrinsic currents
I^{KCa}	calcium-activated potassium current
I^{KNa}	sodium-activated potassium current
I^{Kv}	voltage-activated delayed-rectifier potassium current
I^{leak}	leak current
IN	inhibitory interneuron
I^{Na}	voltage-activated sodium current
I^{NaP}	persistent (slowly inactivating) sodium current
I^{pump}	potassium / sodium pump current
I^T	T-current; transient low voltage activated calcium current
KCC2	potassium-chloride co-transporter isoform 2
K_{ir}	Inwardly-rectifying potassium current
K_v	voltage-gate potassium channel
LFP	local field potential
LVF	low-voltage, fast

mTLE	mesial temporal lobe epilepsy
nACh	nicotinic acetylcholine
NKCC1	sodium-potassium-chloride co-transporter isoform 1
NMDA	N-methyl-D-aspartate
PLI	phase-locking index
PN	excitatory principal neuron
PSD-95	post-synaptic density protein-95
PTE	post-traumatic epilepsy
PV	parvalbumin
PY	excitatory pyramidal neuron
SCP	slow cortical potentials
SOM	somatostatin
TBI	traumatic brain injury
TGFβR1	transforming growth factor β receptor 1
TNFα	tumor necrosis factor-α
TTX	tetrodotoxin
$V_{D/S}$	dendritic / somatic voltage

LIST OF FIGURES

ACKNOWLEDGEMENTS

I would like to start by thanking my advisor, Maxim Bazhenov, for his guidance, insights, believing in me and taking me on as a graduate student, giving me the occasional push I needed to achieve my goals, and providing me with many opportunities to meet and work with many amazing researchers throughout my graduate career. Thank you to the members of my committee Drs. James Brewer, Gert Cauwenberghs, Eric Halgren, Duygu Kuzum, and Brad Voytek for your insightful meetings and conversations, and the amazing career advice. I would like to thank my colleagues Drs. Giri Krishnan and Yury Sokolov with whom I worked on many projects. I would also like to thank all current and past members of the Bazhenov lab for their help, insights, and research over the course of my graduate career. I would like to thank Drs. Terrence Sejnowski, Igor Timofeev, Massimo Avoli, Hyle Park, Devin Binder, Masum Hasan, Zahra Shiri, Sylvain Williams, and Sylvain Chauvette for their collaboration on these and other projects, their research, and their insights. Many thanks to my high school biology teacher Dr. Dee Ann Matthews for encouraging me to pursue a Ph.D. in neuroscience. Thanks to the all the students I had the privilege to work with and mentor throughout grad school: Mara Casebeer, Julio Dominguez, Flavia Huerta, Jacob Stein, Kenny Pham, Paul Cowen, Rocio Iliana, and John Pangilinan.

The staff at both UC Riverside and UC San Diego have been incredibly helpful and supportive. I would especially like to thank Perla Fabelo, Erin Gilbert, and Linh Vandermar for assisting me with the administrative aspects of grad school and for always taking the time to just chat.

To my peers / lab mates / and dearest friends Ryan Golden, Erik Delanois, Tim Tadros, Aiswarya Akumalla, Tiffany Glenn-Hall, and Tim Myers, thank you for the insightful

conversations, encouragement, support, and teaching me the importance of healthy work-life balance. Tiffany and Tim, you both helped me a lot during my transition from undergrad to grad school and during the stressful transition between universities and grad programs. Ryan and Erik, you guys really helped me through the rougher parts of grad school, when I felt helpless and burnt out. You both were able to remind me of the importance of taking a break from my work and relaxing, even if those breaks were brought upon by one of you taking away my computer or dragging me to social events. Ryan, I cannot express how thankful I am for all that you have done for me over the past few years. I don't know how I could have survived the last few years of grad school without your friendship. You have become one of my closest friends and I have absolutely no doubt in my mind that you will be incredibly successful. I truly can't wait to collaborate with you and form our "joint" lab. It is truly difficult to imagine having accomplished what I have without all of you. You all inspire me to push myself further, and better myself as both a scientist and person. I look forward to your many successes and our future collaborations.

Graduate school can be a very trying time. We strive for perfection but are met with constant failure which makes us question our intelligence and impacts our self-confidence and self-worth. Because of this, many of us, myself included, are afflicted with imposter syndrome. I can openly admit to having struggled with this throughout the entirety of grad school. I often found myself turning to members of my cohort for support. I was uniquely fortunate and honored to have had two cohorts. I would like to thank my UC Riverside cohort especially Teresa Wen and Dustin Brewton who helped me develop a strong starting point in grad school. I would also like to thank UC San Diego cohort especially Junmi Saikia, Kevin White, and Ryan Golden for always being there for me, supporting me, and helping me break out of my shell and finish my degree on such a high note.

I would like to thank my parents, Gema and Oscar González, for their constant love and support, and for always encouraging me to pursue careers that make me truly happy. To my brother Adrian and sister-in-law Laurie, in addition to your constant love and support, you both have given me two very special gifts my nephew Gabriel and niece Liliana. Thank you both for always being there for me and reminding me to relax and have fun. To my sister Samantha (Sam), thank you for always supporting me and being such a good friend. I am incredibly proud of the young woman you have become and of all you have accomplished. You mean the world to me, even if I don't always say it. I would also like to thank my grandparents Elisa and Jose Garcia, and Maria and Francisco González. They came to this country with the hopes of providing a better life for their children, one with more opportunities than they were offered in México. Through their sacrifices, they were able to do just that, which ultimately provided me with this amazing opportunity to pursue my passion and be a first-generation Ph.D. student. To my abuelito Francisco, not a day goes by that I don't miss you. No matter what I did, you were always one of my biggest supporters and for that I am eternally grateful. I love you all very much.

Thank you to my extended family, especially Jacob Freeman, Shane Nystrom, Brandon Ricafrente, Grace Toy, Lupe Rodriguez, and my many cousins, uncles and aunts for their love and support. Throughout the years you all have helped me in various ways, and I love you all very much. To Betty and Amelia, you have both been amazing friends and co-workers to my mom and have known me since I was a baby. I have always considered you both family and you both supported and encouraged me just like my family. Thank you for everything! Finally, I would like to thank my K9 companion, Newton, for his unconditional love and always knowing how to cheer me up.

This research was supported by grants provided by the National Institute of Health (R01 EB009282, R01 NS081243, and MH099645), the Office of Naval Research Multidisciplinary University Research Initiative (N000141310672, and N000141612829), and the Canadian Institutes of Health Research (201403M0P-325213, and 201403M0P-324941). Additionally, I received financial support through the National Science Foundation Graduate Research Fellowship Program under grant DGE-1326120.

Chapter 1, in part, is a reprint of the material as it appears in Ionic and Synaptic Mechanisms of Seizure Generation and Epileptogenesis 2019. González, Oscar C.; Krishnan, Giri P.; Timofeev, Igor; Bazhenov, Maxim. The dissertation author was the primary author of this paper.

Chapter 2, in full, is a reprint of the material as it appears in Modeling of Age-Dependent Epileptogenesis by Differential Homeostatic Synaptic Scaling 2015. González, Oscar C.; Krishnan, Giri P.; Chauvette, Sylvain; Timofeev, Igor; Sejnowski, Terrence; Bazhenov, Maxim. The dissertation author was the primary author of this paper.

Chapter 3, in full, is a reprint of the material as it appears in Role of KCC2-Dependent Potassium Efflux in 4-Aminopyridine-Induced Epileptiform Synchronization 2018. González, Oscar C.; Shiri, Zahra; Krishnan, Giri P.; Myers, Timothy L.; Williams, Sylvain; Avoli, Massimo; Bazhenov, Maxim. The dissertation author was the primary author of this paper.

Chapter 4, in full, is a reprint of the material as it appears in Origin of Slow Spontaneous Resting-State Neuronal Fluctuations in Brain Networks 2018. Krishnan, Giri P.; González, Oscar C.; Bazhenov, Maxim. The dissertation author was the primary co-author of this paper.

VITA

2012 Bachelor of Science, University of California Riverside

2012 – 2016 Neurosciences Graduate Study, University of California Riverside

2019 Doctor of Philosophy, University of California San Diego

PUBLICATIONS

Hasan Md.M., González O.C., Myers T.L., Bazhenov M., Park H. "Non-Contact Detection of Neural Activity During Seizure Activation in Mouse Hippocampus using Backscattered Intensity of Optical Coherence Tomography." *In preparation.*

González O.C., Krishnan G.P., Sokolov Y., Bazhenov M. "Can Sleep Protect Memories from Catastrophic Forgetting?" *bioRxiv 569038;* DOI: https://doi.org/10.1101/569038.

González O.C., Krishnan G.P., Timofeev I., Bazhenov M. "Ionic and Synaptic Mechanisms of Seizure Generation and Epileptogenesis." *Neurobiology of Disease,* 130:104485.

Myers T.L., González O.C., Stein J.B., Bazhenov M. (2018) "Characterizing Concentration Dependent Neural Dynamics of 4-Aminopyridine-Induced Epileptiform Activity." *Epilepsy Journal,* 4:128; DOI:10.4172/2472-0895.1000128.

Krishnan G.P., González O.C., Bazhenov M. (2018). "Origin of Slow Spontaneous Resting-State Neuronal Fluctuations in Brain Networks." *Proceedings of the National Academy of Sciences,* 201715841; DOI:10.1073/pnas.1715841115.

González O.C., Shiri Z., Krishnan G.P., Myers T.L., Williams S., Avoli M., Bazhenov M. (2018). "Role of KCC2-Dependent Potassium Efflux in 4-Aminopyridine-Induced Epileptiform Synchronization." *Neurobiology of Disease,* 109:137–147.

González O.C., Krishnan G.P., Chauvette S., Timofeev I., Sejnowski T., Bazhenov M. (2015). "Modeling of Age-Dependent Epileptogenesis by Differential Homeostatic Synaptic Scaling." *Journal of Neuroscience,* 35(39):13448 –13462.

FIELDS OF STUDY

Major Field: Neurosciences
Specialty: Computational Neurosciences

Studies in Computational Neurosciences
Professor Maxim Bazhenov

ABSTRACT OF THE DISSERTATION

Regulation of Neuronal Network Dynamics through Ionic and Synaptic Homeostasis

by

Oscar Christian González

Doctor of Philosophy in Neurosciences with a Specialization in Computational Neurosciences

University of California San Diego, 2019

Professor Maxim Bazhenov, Chair

The regulation of transmembrane ionic and synaptic currents is crucial for maintaining physiological neural activity and allow brain networks to be resilient to external perturbations. To this effect, the brain implements many homeostatic mechanisms by which it can control neuronal excitability and communication by maintaining ionic concentration gradients and synaptic strengths within a physiological range. Indeed, there exist many membrane-bound transporter proteins which function to move ions across the plasma membrane to re-establish resting ionic gradients following changes in neuronal spiking. Similarly, the nervous system has developed homeostatic mechanisms by which it can regulate the strength of synaptic connections by augmenting the number of excitatory post-synaptic receptors present in an activity-dependent

manner. It is traditionally thought that a breakdown of these mechanisms may underlie various neurological and psychiatric disorders. Though much has been learned about ionic and synaptic regulation of single neuron activity, how these homeostatic mechanisms give rise to or influence physiological and pathological brain states remains to be fully understood. Here we explore the roles of ionic and synaptic homeostasis in the regulation of network dynamics. We begin by first demonstrating that in the pathological brain (i.e. one riddled with K-channelopathies or suffering traumatic brain injury) these network stabilizing mechanisms can overcompensate for the chronic network perturbations resulting in hyperexcitability and lowered thresholds for seizure generation. We then demonstrate that the regulation of ionic concentration gradients in the healthy brain can give rise to infra-slow network fluctuations, which may underlie various brain-state transitions and cognitive states. Together these studies highlight the importance of proper ionic and synaptic regulation for the maintenance of physiological activity and transitions to pathological states and provides new insight into the development of interventions that can be used to treat epileptic seizures.

Chapter 1: Introduction

Ionic dynamics and seizures

Transmembrane ion currents and neuronal resting potentials are maintained and regulated by ion concentration gradients between the intra- and extracellular space. As such, their relative concentration gradients influence neuronal and network-wide excitability. Because of this crucial role in the regulation of excitability, there exist many mechanisms for maintaining and re-establishing the resting ion concentration gradients (Somjen, 2002; Frohlich et al., 2008b; Wei et al., 2014a). Breakdown in ion concentration homeostasis has been associated with various neurological disorders including epilepsy and seizure generation (Grisar et al., 1992; Frohlich et al., 2008b; Cressman et al., 2009; Ullah et al., 2009; Frohlich et al., 2010; Avoli and de Curtis, 2011; Filatov et al., 2011; Krishnan and Bazhenov, 2011; Wei et al., 2014a; Hamidi and Avoli, 2015; Krishnan et al., 2015; González et al., 2018). Much attention has been focused on the role of K^+ concentration regulation in seizure onset due to its involvement in the repolarization phase of the action potential and, therefore, overall excitability (Mitterdorfer and Bean, 2002; Bean, 2007; Pathak et al., 2016). Early hypotheses regarding the generation of seizure activity were centered around the idea that elevated extracellular K^+ concentrations ($[K^+]_o$) resulted in network hyperexcitability (Fertziger and Ranck, 1970; Frohlich et al., 2008b). This so-called "K^+ accumulation hypothesis" suggested that increases in $[K^+]_o$ could cross a critical concentration threshold initiating a positive feedback loop and thereby increasing neuronal excitability, which in turn further increased $[K^+]_o$. An increase in $[K^+]_o$ to 8–16 mM *in vitro* (Traynelis and Dingledine, 1988) has been shown to lead to the generation of paroxysmal activity in the hippocampal formation. *In vivo* experiments have shown that seizures develop when perfusion with high K^+ medium occurs for at least 10 min (Zuckermann and Glaser, 1968).

This initial hypothesis was met with some skepticism because increased $[K^+]_o$ by itself was not a sufficient factor in triggering seizures. In fact, there was a lack of evidence for the existence of a $[K^+]_o$ threshold necessary for seizure generation, and the increase of $[K^+]_o$ during seizure activity results in a depolarization block and seizure termination (Frohlich et al., 2008b; Seigneur and Timofeev, 2010).

Though this hypothesis quickly fell out of fashion it has since made a resurgence following the development of new technologies and methods to more precisely probe $[K^+]_o$ dynamics both *in vivo* and *in vitro*, and the development of more detailed biophysical computational models (Kager et al., 2000; Somjen, 2002; Somjen et al., 2008). *In vitro* experiments in mouse hippocampal brain slices have demonstrated that increases in K^+ concentration in bath applied artificial cerebrospinal fluid (ACSF) can result in epileptiform discharges and seizure-like activity resembling inter-ictal spiking and ictal events in epileptic patients (Filatov et al., 2011). The mechanism by which accumulation of $[K^+]_o$ leads to depolarization and hyperexcitability is most likely through the change in the reversal potential of currents mediated by K^+ ion, as predicted by the Nernst equation, which leads to a reduction of the hyperpolarizing outward going K^+ currents. Therefore, increased $[K^+]_o$ leads to neuronal depolarization likely through its direct effects on leak currents (Pedley et al., 1976; Seigneur and Timofeev, 2010). An increase in $[K^+]_o$ also produces a depolarizing shift in the reversal potential of the hyperpolarization-activated depolarizing mixed cation (Na^+/K^+) current (I_h) that contributes to the generation of seizure activity (Timofeev et al., 2002b). As previously stated, K^+ channel activation is associated with the repolarization phase of the action potential thereby regulating neuronal excitability. Increases in $[K^+]_o$ would depolarize the reversal potential of these channels and render them ineffective. In doing so, the neurons will have prolonged periods

of Na^+ and Ca^{2+} channel activation leading to prolonged depolarizations and increased excitability.

Previous computational studies have shown that biophysical models of a cortical network with dynamic K^+ concentrations resulted in a "multistability-mediated dynamic repertoire" in which the neuronal network could exist in a number of stable states including physiological/resting activity, asynchronous tonic firing, and synchronous bursting (Frohlich et al., 2010). These results suggest that brain networks could exist in at least two primary states, either a physiological or pathological activity state (figure 1.1). Both of these states could be represented as local minima of the network dynamics to which the network activity would converge depending on the initial state of the network (Frohlich et al., 2010).

Under this framework, a stable state (like resting or seizure state) has a region called the "basin of attraction," that represents the values of biophysical parameters (such as ion concentration, synaptic activity, etc.), in which network activity remains within the same state. Thus, a larger basin of attraction for the physiological state compared to the pathological state would represent a more resilient network activity state since a larger perturbation of parameter values (such as ion concentration changes due to external input) would be required to switch from physiological to pathological state (figure 1.1, bottom). In contrast, if the basin of attraction of physiological and pathological conditions are similar, then a smaller input can switch from a physiological to a pathological or seizure state. As such, in a normal "healthy" brain, this would produce a physiological activity state that would not easily transition to a pathological seizure state. The basin of attraction for the pathological activity state, in a healthy network, would be characterized by a relatively shallow and narrow basin of attraction (figure 1.1, bottom). It was suggested that in a pathological network, one with mis-regulated K^+ concentrations for example,

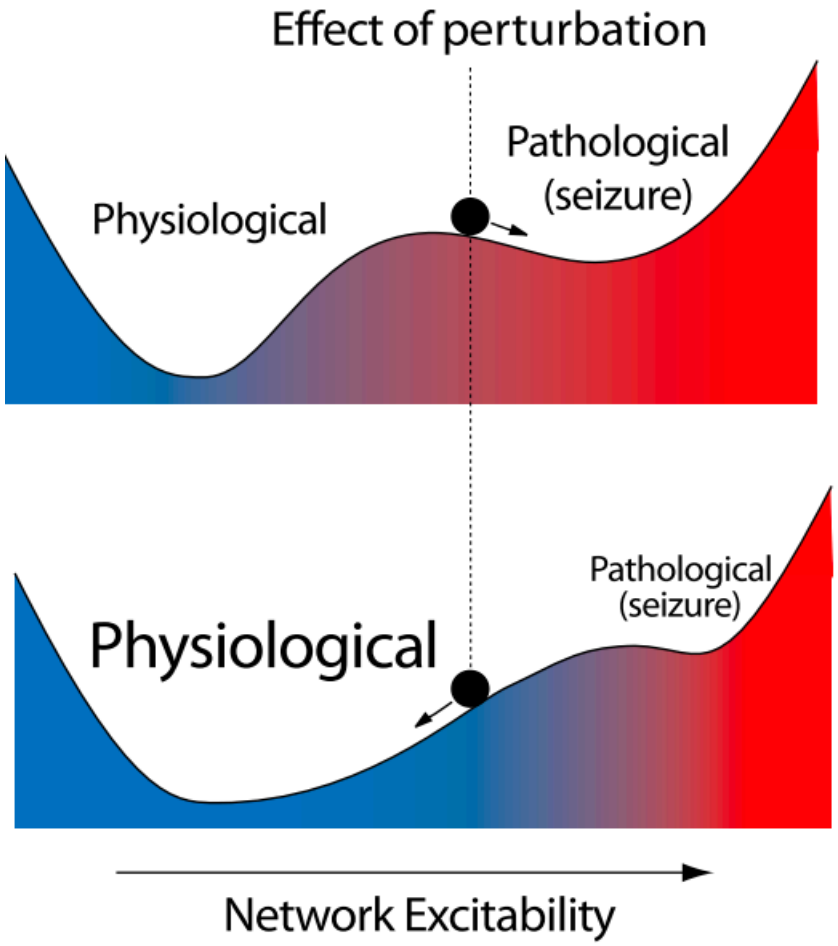

Figure 1.1 Bistability between physiological and pathological network states Illustration of the bistability between the physiological and pathological network states. Top panel shows the basin of attractions for both states in a network which can easily transition to a seizure state. Bottom shoe the basins of attraction for a "healthy" network in which network larger network perturbations are required for transitioning from physiological to pathological seizure states. Figure adapted from (Frohlich et al., 2010).

the basin of attraction for the physiological state may be less broad and more shallow, while the pathological domain of attraction may become broader (Frohlich et al., 2010). As a result, the amount of perturbation necessary to transition network activity from the physiological to the pathological domain in the pathological network would be less than needed for the "healthy" network (figure 1.1, top). Therefore, it would facilitate transitions between the two states resulting in the occurrence of recurrent seizures.

Spontaneous transitions between the physiological and pathological network states can also be thought of in terms of intermittency known from dynamical systems theory; that is, the irregular

switching between semi-periodic and chaotic dynamics (Velazquez et al., 1999; Zalay et al., 2010). This idea was explored in a hippocampal network model of coupled cognitive rhythm generators (CRGs) and the results were further validated by *in vitro* experiments on acute mouse hippocampal brain slices under low Mg^{2+} / high K^+ conditions (Zalay et al., 2010). Within a range of network parameters, the system remains in a high-complexity phase-space region characterized by irregular and interictal-like activity. Because of the presence of an unstable saddle-type fixed point, the network could intermittently escape the high-complexity region and approach the periodic-like ictal saddle. The decay constant of the network controls the occurrence of the intermittent spontaneous transitions between interictal periods and pathological ictal activity (Zalay et al., 2010). Biologically, reduction of this constant could correspond to increased or prolonged post-synaptic excitability, which can manifest as a result of impaired $[K^+]_o$ regulation.

In this model, the transitions from an interictal to an ictal orbit is accompanied by a reduction of the Lyapunov exponent, indicative of a reduction in the divergence of nearby phase-space trajectories, a loss of chaotic behavior and an increase in periodicity (Zalay et al., 2010). A similar reduction in high-complexity / chaotic dynamics was also observed at the transition from interictal to ictal periods in the acute brain slices (Zalay et al., 2010). This change in network behavior was suggested to be caused by attractor crisis-induced intermittency in which the boundary of the basin of chaotic attractor (interictal dynamics) crossed or came into contact with the stable manifold of the saddle (ictal dynamics) (Velazquez et al., 1999; Zalay et al., 2010). The state-space trajectory can, therefore, intermittently enter the area near the low-complexity saddle resulting in transient periodic activity before returning to the higher-complexity attractor. It should be noted that the duration of this transient periodic ictal activity in the model was on the order of a few seconds while biological seizures can vary from a few

seconds to minutes (Zalay et al., 2010). The authors suggest that the longer timescales of biological seizures may result from a time constant longer than most ion channel kinetics. It is possible that the infra-slow time scale of resting-state $[K^+]_o$ fluctuations (Krishnan et al., 2018), which can be exacerbated by mis-regulation of $[K^+]_o$, may lead to the periods of increased post-synaptic excitability resulting in an intermittency between the different dynamical states, thereby facilitating the transitions between physiological and pathological states of the network.

Because of its role in regulating neuronal excitability, K^+ concentration dynamics have been the focus of many seizure related studies. It should be noted that other ionic species have not been as well studied and most likely influence the properties and susceptibility of seizures. Previous work has shown changes to the various ion concentrations prior to and during seizure events (McCreery and Agnew, 1983; Somjen, 2002; Huberfeld et al., 2007; Viitanen et al., 2010). Indeed, extracellular sodium concentrations ($[Na^+]_o$) have been shown to reduce during seizures (Somjen, 2002). This is presumably accompanied by increases in intracellular Na^+ concentration ($[Na^+]_i$). Additionally, intracellular chloride concentration ($[Cl^-]_i$) has been shown to change in response to and influence seizure-like activity (Lillis et al., 2012). $[Ca^{2+}]_o$ dramatically drops during seizure activity from about 1.2 mM to 0.6 mM (Heinemann and Lux, 1977; Pumain et al., 1983). At such low levels of $[Ca^{2+}]_o$ the synaptic transmission becomes greatly impaired (Somjen, 2002; Crochet et al., 2005; Seigneur and Timofeev, 2010). Therefore, synchronization via chemical synaptic mechanisms during seizures is dramatically reduced or absent within the population of neurons directly contributing to the seizure activity. At $[Ca^{2+}]_o$ below 1.0 mM, hemichannels open (Thimm et al., 2005) creating conditions for paroxysmal synchronization of neuronal activities via electrical synapses (Timofeev et al., 2012).

The role of ionic concentration dynamics in seizure termination and postictal depression was explored in computational models in (Krishnan and Bazhenov, 2011). In this cortical network model, in addition to including $[K^+]_{o/i}$ dynamics, the dynamics for $[Na^+]_{o/i}$, $[Cl^-]_i$, and $[Ca^{2+}]_i$ were also represented as dynamic variables controlled by various biophysical mechanisms. A brief depolarizing direct current (DC) input was capable of inducing seizure-like activity which exhibited sustained transitions between periods of tonic firing and synchronized bursting which outlasted the stimulus input but eventually resulted in the termination of the seizure-like activity (figure 1.2) (Krishnan and Bazhenov, 2011). It was again proposed that these transitions in activity states resulted from a bistability in the network dynamics for a range of $[K^+]_o$ (Frohlich and Bazhenov, 2006; Frohlich et al., 2010). During tonic firing, the efflux of K^+ overwhelmed the K^+ regulatory mechanisms allowing $[K^+]_o$ to reach higher values. Once $[K^+]_o$ reached a high enough value, the network activity transitioned to synchronized bursting. During the bursting periods, the $[K^+]_o$ decreased due to lower overall firing (bursting includes higher frequency firing and quiescent periods, figure 1.2A). The $[K^+]_o$ reduced until reaching a low enough value at which a return to the tonic spiking regime occurred (figure 1.2) (Krishnan and Bazhenov, 2011). As a consequence of the repeated tonic and bursting periods, within an episode of seizure, the $[K^+]_o$ fluctuates as observed in experiments (Heinemann and Lux, 1977).

During these seizure-like events, $[Na^+]_i$ and $[Cl^-]_i$ increased gradually due to the higher firing rates of excitatory and inhibitory neurons, respectively. $[Na^+]_i$ progressively increased during the seizure-like event, while $[Cl^-]_i$ showed a fast increase during seizure initiation and then remained relatively elevated (Krishnan and Bazhenov, 2011), which is in agreement with several experimental paradigms (Somjen, 2002; Lillis et al., 2012). These modeling studies suggested that progressive accumulation of $[Na^+]_i$ would lead to stronger activation of the Na^+/K^+

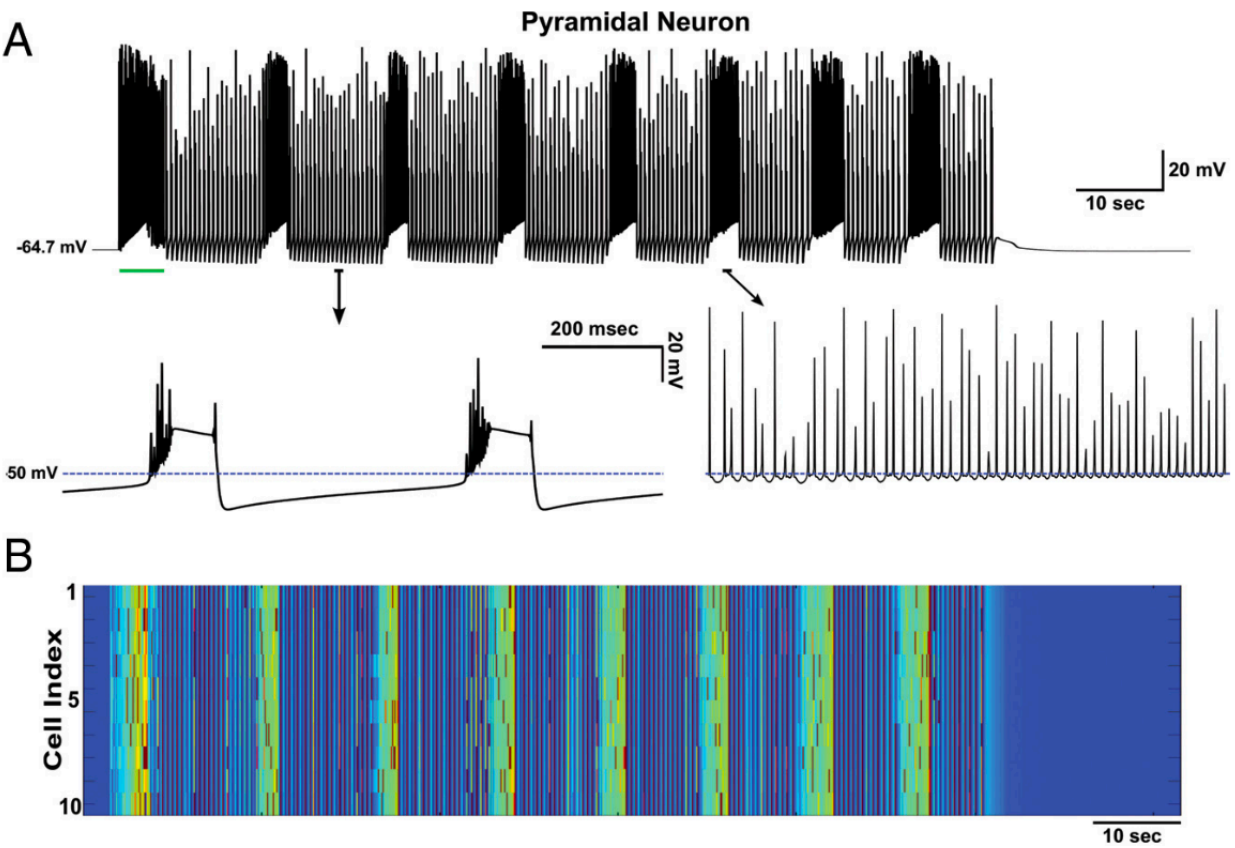

Figure 1.2 Tonic-clonic seizure transitions and spontaneous termination. A, Membrane potential of a single excitatory pyramidal neuron from the network B. A transient DC input (green line) resulted in a depolarization of the neurons and generation of seizure-like activity which continued past the stimulation offset. The resulting seizure-like discharge exhibited several state transitions between tonic (asynchronous firing) and clonic (bursting) periods before spontaneous termination. The bottom plots show activity during bursting (left) and tonic (right) periods. **B,** Heatmap showing membrane voltage of all pyramidal neurons in the network. Shows highly synchronized firing during bursting episodes. Figure adapted from (Krishnan and Bazhenov, 2011).

ATPase; this in turn would lead to an increase of the Na^+/K^+ ATPase outward current (at each cycle Na^+/K^+ ATPase removes 3 Na^+ ions and brings in 2 K^+ ions, thus creating an outward current). The resulting hyperpolarization of membrane voltage would trigger termination of seizure and initiate the postictal depression state (figure 1.2) (Krishnan and Bazhenov, 2011). Postictal depression following most seizure events was suggested to be a result of the prolonged elevation of $[Na^+]_i$ and continued Na^+/K^+ ATPase activity, which would lead to the progressive decrease in $[K^+]_o$ past its baseline level, a finding that has been previously reported experimentally (Jensen and Yaari, 1997). The role of the Na^+/K^+ ATPase in the generation of

seizure activity has been explored in previous work (Grisar et al., 1992; Krishnan et al., 2015; Wei et al., 2014b). Recent computational and experimental studies have also linked oxygen dynamics to impairments in Na^+/K^+ ATPase activity leading to the onset of seizures and cortical spreading depression (Ingram et al., 2014; Wei et al., 2014a).

Astrocytes play a major role in the regulation of the extracellular milieu. Indeed, astrocytes have been shown to contribute to the tight regulation of the extracellular ion concentrations and neurotransmitters at the synapse (Coulter and Steinhauser, 2015; de Lanerolle et al., 2010; Kjaerby et al., 2017; Patel et al., 2019; Poskanzer and Yuste, 2016; Tian et al., 2005). Two primary mechanisms by which astrocytes regulate $[K^+]_o$ include: 1) K^+ uptake and 2) spatial buffering through the astrocytic syncytium. $[K^+]_o$ uptake has been suggested to involve the Na^+/K^+ ATPase, sodium-potassium-chloride co-transporter isoform 1 (NKCC1), and inwardly rectifying K^+ (K_{ir}) channels (Coulter and Steinhauser, 2015; de Lanerolle et al., 2010; Patel et al., 2019; Somjen, 2002). The most predominant mechanism for astrocytic K^+ uptake seems to be through K_{ir} channels (Olsen and Sontheimer, 2008; Patel et al., 2019; Steinhauser et al., 2012). As such, many studies have focused on altered expression or impaired K_{ir} channels as a key factor in impaired $[K^+]_o$ regulation and seizure generation (Olsen and Sontheimer, 2008; Patel et al., 2019; Steinhauser et al., 2012). $K_{ir}4.1$ is the main K_{ir} subunit expressed in astrocytes and has been shown to be down-regulated in patients suffering mesial temporal lobe epilepsy (mTLE) (Heuser et al., 2012). Additionally, deletion of the astrocytic specific $K_{ir}4.1$ channel results in spontaneous recurrent seizures in mice (Chever et al., 2010; Djukic et al., 2007; Haj-Yasein et al., 2011). Down-regulation of $K_{ir}4.1$ channels has also been observed following traumatic brain injury (TBI) (D'Ambrosio et al., 2005; D'Ambrosio et al., 1999). TBI commonly presents with increased blood-brain-barrier (BBB) permeability. Dysfunction of the BBB results

in extravasation of serum albumin which can directly activate transforming growth factor-β receptor 1 (TGFβR1) leading to the down-regulation of $K_{ir}4.1$ channels, excitatory amino acid transporter 2 (EAAT2), and gap junction protein connexin 43 (CX43), and alters the expression and trafficking of aquaporin-4 (AQP4) channels all of which have been shown to contribute to the regulation of $[K^+]_o$ and extracellular glutamate concentrations (Braganza et al., 2012; Coulter and Steinhauser, 2015; Friedman et al., 2009; Seiffert et al., 2004; Stewart et al., 2010; van Vliet et al., 2007).

Altered spatial buffering through the astrocytic syncytium has been suggested to influence seizure initiation (Coulter and Steinhauser, 2015; Giaume et al., 2010; Steinhauser et al., 2012). Once K^+ enters astrocytes through $K_{ir}4.1$ channels, K^+ is redistributed via gap junctions throughout the astrocytic syncytium (Coulter and Steinhauser, 2015). As previously mentioned, serum albumin activation of TGFβR1 has been shown to result in reduced CX43 expression. CX43, along with CX30, are the two primary connexin protein subunits comprising the gap junctions which form the astrocytic syncytium (Coulter and Steinhauser, 2015; Wallraff et al., 2006). Altered CX43 expression may result in impaired intracellular ionic coupling between astrocytes, thereby affecting K^+ spatial buffering, extracellular glutamate uptake, transport of important metabolites, and impair Ca^{2+} wave propagation (Coulter and Steinhauser, 2015; Wallraff et al., 2006). It should be noted that both increases and decreases in CX43/30 expression have been observed in human patients and animal models of epilepsy (Coulter and Steinhauser, 2015; Giaume et al., 2010; Steinhauser et al., 2012). As such, how the differential expression of CXs affects hyperexcitability and seizure generation remains to be fully understood.

The movements of the charges associated with the high neuronal activity (particularly during seizures) result in the generation of weak electric fields which may play a role in the modulation of neuronal excitability and synchrony (Anastassiou and Koch, 2015; Frohlich and McCormick, 2010; Qiu et al., 2015; Shivacharan et al., 2019; Zhang et al., 2014). It has been shown that these weak endogenous electric fields can cause changes in the resting membrane potential of the closely located neurons (Anastassiou and Koch, 2015; Frohlich and McCormick, 2010). Recent studies have demonstrated that the propagation speed (~ 0.1m/s) of pharmacologically-induced seizure-like activity in hippocampal tissue is strongly influenced by the weak endogenous electric field coupling (Qiu et al., 2015; Shivacharan et al., 2019; Zhang et al., 2014). Indeed, the speed of seizure propagation, as measured both in animal models and in epileptic patients, could not be explained by the ionic diffusion alone, as diffusion rates are much slower (Shivacharan et al., 2019). Furthermore, propagation speed of seizure-like activity was unaffected in conditions of reduced synaptic transmission suggesting that it is mediated by non-synaptic mechanisms (Qiu et al., 2015; Shivacharan et al., 2019; Zhang et al., 2014). In a recent study, it was shown that cutting the hippocampus and separating the two halves by 400μm prevented the propagation of seizure-like activity between the two halves (Shivacharan et al., 2019). Interestingly, when the two sides were put back together, the spontaneous seizure-like activity was able to propagate between the two cut sections with a propagation speed of (~ 0.09m/s). Application of an external electric field, that was calibrated to negate the endogenous electric field generated during seizure-like activity, prevented the propagation of the seizure-like activity (Shivacharan et al., 2019). These data suggest that weak endogenous electric fields generated during epileptic seizures can aid in the recruitment of the neighboring neuron populations and thereby propagation of the seizure-like activity.

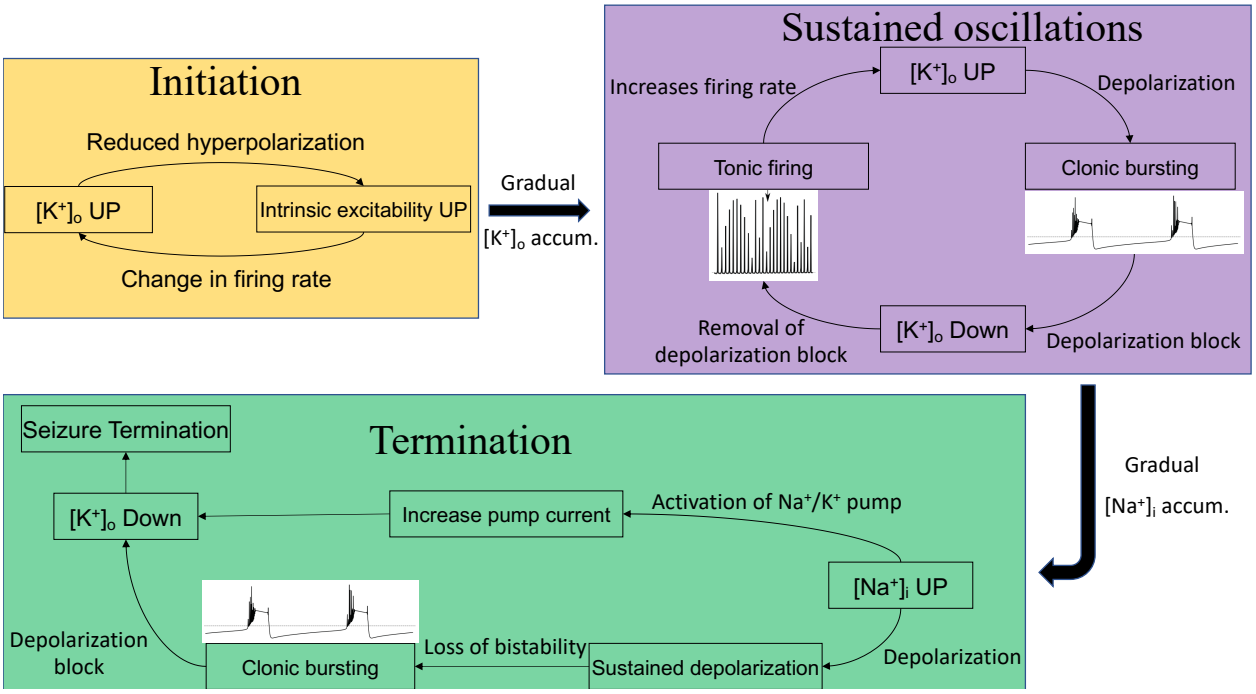

Figure 1.3 Interaction between seizure initiation, propagation, and termination. This figure shows the interaction between the different stages of seizure initiation, propagation and termination and the interactions between ion concentrations and network states. Orange panel shows the positive feedback loop between $[K^+]_o$ and network excitability initiating seizures. The gradual accumulation of $[K^+]_o$ caused by the feedback loop (orange) allows the network to progressively depolarize until the network enters a state of sustained oscillations between tonic firing and clonic bursting. Purple panel shows how $[K^+]_o$ fluctuations give rise to the bistability between tonic firing and clonic bursting during the progression of a seizure. As the network cycles through these two bistable states, there is a gradual accumulation of $[Na^+]_i$. This accumulation results in the loss of the bistability between the tonic/clonic states and triggers seizure termination. Green panel outlines how accumulation of $[Na^+]_i$ results in the loss of the tonic/clonic bistability and activation of the Na^+/K^+ ATPase leading to the termination of the seizure and postictal depression.

Thus, the intricate interactions between various ionic species in the brain may underlie the transitions and maintenance of seizure onset, progression, and termination. These interactions are summarized in figure 1.3. As the maintenance of the relative ionic concentration gradients is a critical component in the resilience of a network against transitions to pathological seizure states, it is not surprising that there are exist many homeostatic mechanisms implemented in the brain to maintain ion concentrations within a physiological range. Therefore, impairments in these homeostatic mechanisms, such as the Na^+/K^+ ATPase and the KCC2 co-transporter, would increase seizure susceptibility and development of epilepsy.

Epilepsy

Epilepsy remains one of the most common neurological disorders worldwide (Lukawski et al., 2018). Epilepsy is used to describe a number of neurological disorders characterized by spontaneous, recurrent seizures. These seizures manifest as either convulsive or non-convulsive events with varied effects on the level of consciousness during an attack. Seizures are associated with large increases in neuronal firing, and exhibit periods of synchronous bursting and asynchronous firing (Bazhenov et al., 2004; Timofeev and Steriade, 2004; Frohlich et al., 2008b; Frohlich et al., 2010; Krishnan and Bazhenov, 2011; González et al., 2015; Hamidi and Avoli, 2015; González et al., 2018; Lukawski et al., 2018). Roughly 70% of patients suffering from epilepsy have seizures, which are well controlled through pharmacological interventions (Timofeev et al., 2013; Lukawski et al., 2018). For the remaining 30% of patients, their seizures are categorized as pharmaco-resistant or intractable and require more extreme interventions such as resection of epileptic foci to find relief. Additionally, patients who respond well to medications can develop a resistance to chronic use of specific medications and require new cocktails of pharmacological agents or higher doses which can manifest other neurological deficits including memory issues, migraines, and other cognitive impairments (Brodie and French, 2000; Brodie and Kwan, 2001; Ortinski and Meador, 2004; Perucca and Tomson, 2011; Perucca and Gilliam, 2012). In light of the advancements in the treatment of epilepsy and seizure prevention, the underlying mechanisms that give way to epilepsy and seizure generation remain poorly understood.

Determining the underlying mechanisms of epileptogenesis and seizure generation is complicated by the diverse etiologies involved in epilepsy (D'Adamo et al., 2013; Lukawski et al., 2018). Epileptogenesis is a set of processes taking place in acquired epilepsies between the

initial insult and the onset of epilepsy (Timofeev et al., 2013). Epilepsy can be divided into two main categories: acquired and genetic epilepsies. Many different insults to the brain can lead to the immediate (hours to days) or delayed (months to years) generation of seizures and potential development of epilepsy (Topolnik et al., 2003b; Houweling et al., 2005; Nita et al., 2006; Timofeev et al., 2010; Timofeev et al., 2013). TBI, stroke, infections, and tumors are commonly associated with the development of acquired epilepsy (Timofeev et al., 2013; Lukawski et al., 2018). TBI remains one of the most common factors leading to epileptogenesis. Penetrating brain wounds commonly result in epileptogenesis with a delay period of months to years following the initial insult (Kollevold, 1976; Dinner, 1993; Temkin et al., 1995; Annegers et al., 1998; Topolnik et al., 2003a; Jin et al., 2006; Nita et al., 2007; Avramescu and Timofeev, 2008; Chauvette et al., 2016). Indeed, 80% of patients suffering severe TBI exhibit paroxysmal activity within 24 hours of injury (Kollevold, 1976; Dinner, 1993). The severity of the trauma has been suggested to play an important role in the susceptibility to the development of paroxysmal activity (Houweling et al., 2005; Frohlich et al., 2008a; Volman et al., 2011a; Volman et al., 2011b; González et al., 2015). Post-traumatic seizures are a risk factor in adults, but it may be less likely for infants (Angeleri et al., 1999). Young children display mainly early seizures, but adolescents and adults become epileptic after some latent period (Asikainen et al., 1999). In a more recent study (Christensen et al., 2009) assessed the risk of developing epilepsy in children and young adults suffering from TBI. It was found that the risk of epilepsy was dependent on the severity of the trauma and the age of patient at the time of injury with patients who were older at the time of trauma were more likely to develop chronic epilepsy. Though the exact mechanism leading to the development of TBI-induced epilepsy remains poorly understood, it has been suggested that homeostatic synaptic plasticity may be a key culprit in this form of

epileptogenesis. Understanding the molecular, cellular and network processes accompanying epileptogenesis will lead to an understanding of the development of epilepsy characterized by unprovoked seizures. Prevention of epileptogenesis will therefore prevent epilepsy.

Idiopathic epilepsies have been associated with various genetic mutations (D'Adamo et al., 2013; Lukawski et al., 2018). Many studies have shown that genetic mutations leading to impaired ion channel expression and regulatory proteins lead to hyperexcitability and epileptic seizures (Ottman et al., 2004; Singh et al., 2006; Nobile et al., 2009; D'Adamo et al., 2013; Dazzo et al., 2015; Lascano et al., 2016). Indeed, studies on excised tissue from epileptic patients have shown impaired Na^+/K^+ ATPase activity, potassium-chloride co-transporter isoform 2 (KCC2) expression, K^+ channel activity, and nicotinic acetylcholine (nACh) channel activity (Huberfeld et al., 2007; Buchin et al., 2016; Lukawski et al., 2018). Specifically, K^+-channelopathies have been linked to many forms of intractable epilepsy (D'Adamo et al., 2013). As K^+ channels are a key regulator of intrinsic neuronal excitability, disruption or impairment of these channels can lead to hyperexcitability and reduce the threshold for seizure initiation. In addition to mutations causing impairments of specific K^+ currents, genetic mutations affecting proteins which regulate or influence K^+ channel kinetics have also been shown to cause increased propensity for seizure onset (Ottman et al., 2004; Nobile et al., 2009; Dazzo et al., 2015). Similar to TBI-induced epilepsy, the exact biophysical mechanisms leading to seizure generation and potential development of epilepsy in these forms of genetic epilepsies remains to be fully understood.

K-channelopathy-related epilepsy and KCC2 co-transporter

Various channelopathies have been associated with increased seizure susceptibility and epileptogenesis (D'Adamo et al., 2013; Lascano et al., 2016). K^+-channelopathies are

characterized by mutated or misregulated K^+ channels resulting in network hyperexcitability. The term K^+-channelepsy has been coined to describe a number of neurological disorders which exhibit increased propensity for epileptogenesis due to underlying K^+ channel impairments (D'Adamo et al., 2013). K^+ channels represent one of the most diverse and largest family of ion channels, and as such, we will focus here on impairment of the K^+ channels which mediate the outward going A-current (I_A).

The outward going I_A has been shown to influence action potential firing by modulating the inter-spike interval in response to prolonged subthreshold current injections (Mitterdorfer and Bean, 2002; Bean, 2007; Pathak et al., 2016). The I_A, along with the dendrotoxin sensitive K^+-type D-current (I_D), have been shown to account for much of the hyperpolarizing K^+-currents present during the repolarization phase of mammalian action potentials within regions of the cortex and hippocampus (Bean, 2007). I_A is mediated by multimeric channels, which are comprised of voltage-gated K^+ (K_V) channel K_V1 and K_V4 α-subunits in combination with modulatory β-subunits (Singh et al., 2006; D'Adamo et al., 2013). Mutations in these α-subunit families have been shown to exist in a population of patients exhibiting pharmaco-resistant epilepsy (Singh et al., 2006; D'Adamo et al., 2013). Attenuation of I_A, as a result of these mutations, has been shown to increase the likelihood for seizure generation (Singh et al., 2006). Furthermore, mutations resulting in impaired expression of I_A regulating proteins, such as the leucine-rich glioma-inactivated 1 (LGI1) gene, have been shown to result in the rapid inactivation of I_A and the development of paroxysmal activity (Ottman et al., 2004; Nobile et al., 2009; Dazzo et al., 2015).

The robust convulsive compound 4-aminopryidine (4AP) is a strong I_A antagonist (Avoli and de Curtis, 2011). Indeed, application of 4AP leads to the transition from

physiological/resting activity to pathological seizure-like discharges both *in vitro* and *in vivo* (Fragoso-Veloz et al., 1990; Avoli et al., 1996; Lopantsev and Avoli, 1998; Levesque et al., 2013). It should be noted that the direct knockout of the $K_V4.2$ α-subunit was unable to generate spontaneous recurrent seizures, though it did increase the susceptibility for seizure onset in response to additional convulsive pharmacological compounds (Barnwell et al., 2009). In light of these findings, the previously proposed mechanism for 4AP-induced ictogenesis in which reduction of I_A promotes seizure by directly increasing neuronal excitability has come into question (Galvan et al., 1982; Gustafsson et al., 1982; Yamaguchi and Rogawski, 1992). As such, the exact mechanism by which altered I_A activity leads to the development of spontaneous seizures and epileptogenesis remains to be fully understood.

The balance between excitatory and inhibitory activity is required for the maintenance of stable physiological network activity. Seizures have been traditionally believed to be caused by a breakdown of this balance favoring the reduction of inhibition and subsequent run-away excitability (Ben-Ari et al., 1979; Dingledine and Gjerstad, 1980; Schwartzkroin and Prince, 1980). Recent work has shown that increase in inhibitory $GABA_A$ receptor signaling may underlie seizure generation (Sessolo et al., 2015; Yekhlef et al., 2015; Shiri et al., 2016). Typically, during seizures most pyramidal neurons are depolarized and, due to depolarization block, their firing is dramatically reduced, but the interneuron firing and therefore overall $GABA_A$-dependent Cl^- influx is increased which may result in Cl^- currents becoming depolarizing (Cohen et al., 2002; Timofeev et al., 2002a; Timofeev and Steriade, 2004). However, following 4AP treatment, increases in $[Cl^-]_i$ in excitatory neurons, and increases in inhibitory interneuron firing at the onset of seizure-like discharges have been reported both *in vivo* (Grasse et al., 2013; Toyoda et al., 2015) and *in vitro* (Lillis et al., 2012; Uva et al., 2015;

Levesque et al., 2016). Additionally, intense stimulation of GABAergic interneurons has been demonstrated to increase $[K^+]_o$ and generate long-lasting depolarizations (Rivera et al., 2005; Viitanen et al., 2010). These transient GABAergic excitatory $[K^+]_o$ signals elicit prolonged depolarizations in rat temporal lobe, and may contribute to seizure generation (Lopantsev and Avoli, 1998; Viitanen et al., 2010).

The potassium-chloride co-transporter isoform 2 (KCC2) has recently been suggested to play a crucial role in the development of 4AP-induced seizures (Hamidi and Avoli, 2015; Levesque et al., 2016; González et al., 2018). The KCC2 co-transporter is one of the primary membrane-bound proteins responsible for maintaining the Cl^- concentration gradient (Payne et al., 2003). Unlike the Na^+/K^+ ATPase, the KCC2 is a passive ion transporter, relying on the K^+ concentration gradient to transport both Cl^- and K^+ out of the cell. Increases in $[Cl^-]_i$ lead to KCC2 activation and the efflux of one Cl^- and one K^+ ion, while elevations of $[K^+]_o$ halt its activity (Payne et al., 2003). Due to this activation paradigm, it has been proposed that the synchronized activation of GABAergic interneurons may cause a gradual accumulation of $[Cl^-]_i$, activating the KCC2 co-transporter. This activation would initiate the efflux of both Cl^- and K^+, elevating the $[K^+]_o$ and triggering the positive feedback loop between increases in $[K^+]_o$ and neuronal excitability described above. 4AP-induced ictal events and high-frequency stimulation-induced increases in $[K^+]_o$ could be prevented through the reduction of KCC2 activity (Hamidi and Avoli, 2015). It is therefore likely that the KCC2 co-transporter is involved in the generation of seizure-like discharges in a network plagued with impaired K^+ channel kinetics.

The brain has developed a number of homeostatic mechanisms by which it is capable of maintaining and re-establishing ionic concentration gradients. In the healthy brain, these mechanisms serve the purpose of maintaining normal physiological activity. However, in the

pathological brain, such as brains afflicted by K^+-channelopathies, these homeostatic mechanisms may actually exacerbate existing network hyperexcitability shifting the network to pathological seizure activity states.

Homeostatic synaptic scaling and TBI-induced epilepsy

Patients suffering from penetrating brain wounds after returning from the Vietnam war showed increased likelihood for epileptogenesis up to 15 years after the initial trauma (Salazar et al., 1985). As mentioned earlier, severe brain trauma, including penetrating brain wounds, are commonly associated with the development of epilepsy (Frohlich et al., 2008a; Timofeev et al., 2010; Timofeev et al., 2013). Experimentally, partial cortical deafferentation in cats has been used as a model of penetrating brain wounds to study post-traumatic epilepsy (PTE) (Topolnik et al., 2003a, b; Nita et al., 2006, 2007; Avramescu and Timofeev, 2008). A similar type of paroxysmal activity was also found in undercut model of epileptogenesis in mice (Chauvette et al., 2016; Ping and Jin, 2016). Similarly, slices from isolated cortical slabs show increased sensitivity to convulsive pharmacological compounds, and readily exhibit epileptiform discharges (Prince and Tseng, 1993). Partial cortical deafferentation presents with reduced neuronal excitability and firing rates immediately following trauma (Topolnik et al., 2003a, b; Nita et al., 2006; Avramescu and Timofeev, 2008). This perturbation of network activity has been shown to result in the modification of synaptic strengths through homeostatic synaptic plasticity (HSP) (Avramescu and Timofeev, 2008). Though severe penetrating brain wounds remain a common factor leading to acquired epilepsy, the exact underlying mechanism by which such wounds lead to the transition of the healthy brain to a pathological state over a prolonged delay period remains to be understood but may involve homeostatic regulation of synaptic strength.

HSP is a slow negative feedback bidirectional process which aims to maintain a target network firing rate through the activity-dependent modulation of post-synaptic AMPA receptor densities (Burrone and Murthy, 2003; Turrigiano, 2008; Pozo and Goda, 2010). Network-wide reduction of activity, through cortical deafferentation or the application of tetrodotoxin (TTX), has been demonstrated to result in increased synaptic strength and neuronal excitability in order to recover a baseline firing rate through HSP (Topolnik et al., 2003a, b; Wierenga et al., 2005; Jin et al., 2006; Nita et al., 2006; Echegoyen et al., 2007; Trasande and Ramirez, 2007; Avramescu and Timofeev, 2008; Ibata et al., 2008; Lemieux et al., 2014). Activation of this bidirectional mechanism has been suggested to involve activity-dependent $[Ca^{2+}]_i$ sensors influencing relative TNFα and BDNF expression levels (Burrone and Murthy, 2003; Turrigiano, 2008; Pozo and Goda, 2010). Additionally, the bidirectionality of HSP appears to be differentially regulated, with TNFα and BDNF levels influencing synaptic up-scaling and changes in PSD-95 affecting down-scaling of synaptic strengths in response to prolonged increases in network activity (Turrigiano, 2008; Pozo and Goda, 2010; Sun and Turrigiano, 2011). Therefore, impairments in the bidirectionality of this mechanism could mediate transitions to an epileptic state following TBI.

In healthy tissue, HSP works to counteract the intrinsically unstable Hebbian plasticity, prevent run-away excitability, and maintain overall network stability (Pozo and Goda, 2010). However, in the case of chronic reduction of activity, as observed in response to cortical deafferentation, HSP may fail to precisely compensate for the loss of network-wide activity, thereby promoting hyperexcitability and the generation of paroxysmal epileptiform discharges (Houweling et al., 2005; Frohlich et al., 2008a; Volman et al., 2011a; Volman et al., 2011b). Indeed, previous studies have shown that, in a computational model of the cortical network,

deafferentation of afferent inputs to a subpopulation of neurons within the network initiated homeostatic up-regulation of AMPA receptor conductance (Houweling et al., 2005; Volman et al., 2011a; González et al., 2015). Though the network was able to recover its baseline firing rate, the synaptic strengths increased substantially, putting the network in a pathological hyperexcitable state in which seizures could be easily generated.

Recent work also suggests that the susceptibility to PTE may be age-dependent (Timofeev et al., 2013; González et al., 2015). Partial cortical deafferentation in young and old cats resulted in the generation of spontaneous recurring electrographic seizures in older animals. Though acute seizures were observed in young animals within hours of the initial insult, sustained epileptogenesis was not observed in these younger cats. It was hypothesized that age-dependent impairment of the down-scaling mechanism of HSP may underlie the increased seizure susceptibility for older animals and patients (Timofeev et al., 2013). Recent experimental work has provided evidence for age-dependent differences in HSP down-scaling. It was demonstrated that the differential expression of the scaffolding protein PSD-95 in older neurons rendered homeostatic down-scaling ineffective (Sun and Turrigiano, 2011). Endogenous levels of PSD-95 increase with age, and it was shown that in old neurons, upregulation of PSD-95 impaired the HSP down-scaling without impacting HSP up-scaling (Sun and Turrigiano, 2011). As such, it is possible that the initial compensation for decreased network activity following TBI through HSP up-scaling can drive an older network to a higher AMPA conductance pathological state. In a younger network, HSP down-scaling would correct for this initial overcompensation by reducing AMPA receptor conductances and re-establishing physiological activity state. The reduced or lack of bidirectionality of HSP, due to increased levels of PSD-95 in older animals,

may keep the older network in a higher AMPA conductance state rendering the network more prone to seizure onset.

In a similar vein as to how mechanisms of ionic homeostasis, which are meant to maintain physiological activity and combat hyperexcitable pathological states, homeostatic mechanisms which regulate synaptic strength such as homeostatic synaptic scaling can drive a network to pathological states when the underlying network has undergone some form of sever perturbation. In its attempts to recover baseline activity following trauma, HSP may overcompensate for the initial loss of network-wide activity and alter the dynamics of the network such that the basin of attraction for the pathological state becomes more similar to the physiological state. As described earlier, this would result in an easier transition to pathological seizure states in response to small network perturbations.

Infra-slow resting-state network fluctuations and epilepsy

Recurrent spontaneous seizures are a hallmark of epileptic disorders. It is not, however, the only symptom. Epilepsy often presents with comorbid psychiatric disorders and cognitive impairments (Krishnamoorthy et al., 2007; Cataldi et al., 2013). Of patients suffering mesial temporal lobe epilepsy (mTLE), the most common form of focal epilepsy, an estimated 24-72% also suffer from depression and roughly 10-19% present with psychosis (Gaitatzis et al., 2004; Nadkarni et al., 2007; Cataldi et al., 2013). During seizure episodes, patients often experience altered levels of awareness, confusion, hallucinations, anxiety and paranoia (Krishnamoorthy et al., 2007). Similarly, interictal periods can also be plagued by hallucinations, memory deficits, delirium, behavioral disturbances, and personality disorders (Krishnamoorthy et al., 2007). Traditionally, focal epileptic seizures have been thought to originate in an isolated epileptic focus (Cataldi et al., 2013). This train of thought has become controversial as more studies have shown

that a number of brain regions within the temporal lobe, including the hippocampus and extrahippocampal structures, can function as epileptic foci (Bartolomei et al., 2005; Bartolomei et al., 2008). As such, the description of mTLE as an isolated epileptic focus disorder has been replaced with mTLE as a temporal lobe network disorder. This mTLE network may involve the hippocampus as well as other limbic structures, subcortical areas such as the thalamus, and various neocortical regions (Cataldi et al., 2013).

Recent functional magnetic resonance imaging (fMRI) studies have demonstrated altered spontaneous resting-state network activity in patients with mTLE (Vanhatalo et al., 2004; Liao et al., 2010; Zhang et al., 2010b; Zhang et al., 2010a; Liao et al., 2011; Fahoum et al., 2012). There is now substantial evidence for the role of resting-state networks in the regulation of various conscious, cognitive, and affective behaviors (Vanhatalo et al., 2004; Fukunaga et al., 2006; Buckner et al., 2008; Greicius, 2008; Greicius et al., 2008; Broyd et al., 2009; Zhang and Raichle, 2010; Picchioni et al., 2011). Studies comparing patients with mTLE to healthy subjects have demonstrated altered spontaneous resting-state activity and functional connectivity between specific nodes within these resting-state networks (Liao et al., 2010; Zhang et al., 2010b; Zhang et al., 2010a; Liao et al., 2011). One such affected network is the Default Mode Network (DMN) which has key nodes in the posterior cingulate cortex and the ventral medial prefrontal cortex (Greicius et al., 2003; Buckner et al., 2008; Greicius et al., 2008; Broyd et al., 2009; Greicius et al., 2009). The DMN has been historically referred to as a task-negative functional network as the structures that comprise this network are deactivated during goal-directed tasks and external stimuli (Buckner et al., 2008; Raichle, 2011, 2015). However, DMN activation occurs in response to internal stimuli, memory retrieval, mind-wandering, and abstract thinking (Buckner et al., 2008; Raichle, 2011, 2015). mTLE patients show overall reduced activation and decreased

functional connectivity between keys nodes of the DMN (Vanhatalo et al., 2004; Liao et al., 2010; Zhang et al., 2010b; Zhang et al., 2010a; Liao et al., 2011; Fahoum et al., 2012). Additionally, epileptic events such as interictal population spikes have been shown to decrease DMN activity similar to deactivation patterns observed in healthy subjects in response to natural sensory input (Kobayashi et al., 2006; Fahoum et al., 2012). Interestingly, several neurological and psychiatric disorders, such as Alzheimer's and schizophrenia, have been shown to correlate with altered resting-state fluctuations and functional connectivity within the DMN (Vanhatalo et al., 2004; Buckner et al., 2008; Greicius, 2008; Lui et al., 2008; Broyd et al., 2009; Raichle, 2010; Zhang and Raichle, 2010; Gupta et al., 2017). These alterations in spontaneous resting-state activity and functional connectivity within various resting-state networks such as the DMN may explain decreased cognitive performance in mTLE patients and other comorbid psychiatric disorders (Cataldi et al., 2013).

The spontaneous resting-state activity fluctuations in fMRI signals are a robust phenomenon that has been widely used to evaluate brain network properties (Vanhatalo et al., 2004; Fukunaga et al., 2006; Buckner et al., 2008; Greicius, 2008; Greicius et al., 2008; Broyd et al., 2009; Zhang and Raichle, 2010; Picchioni et al., 2011). In attempting to study the source of noise in fMRI recordings during resting-states, Biswal et al. (1995) observed that the spontaneous background fluctuations recorded during fMRI scans were coherent between functionally related brain regions (Biswal et al., 1995). Since then, other studies have shown similar coherent resting-state activity between regions comprising functional networks such as the DMN and executive control network (Fukunaga et al., 2006; Raichle and Mintun, 2006; Buckner et al., 2008; Greicius, 2008; Greicius et al., 2008; Broyd et al., 2009; Greicius et al., 2009; Larson-Prior et al., 2009; Raichle, 2011, 2015). These resting-state fluctuations occur in

the frequency range of 0.01 – 0.2 Hz (Fukunaga et al., 2006; Honey et al., 2007; Buckner et al., 2008; Ghosh et al., 2008; Greicius, 2008; Greicius et al., 2008; He et al., 2008; Khader et al., 2008; Broyd et al., 2009; Greicius et al., 2009; Larson-Prior et al., 2009; Lorincz et al., 2009; Chang and Glover, 2010; Picchioni et al., 2011; Palva and Palva, 2012; Pan et al., 2013; Hiltunen et al., 2014; Raichle, 2015), and are reported with neuroimaging, electrophysiological, and optical techniques (Biswal et al., 1995; Fukunaga et al., 2006; Greicius, 2008; Greicius et al., 2008; Pan et al., 2013; Hiltunen et al., 2014). Though the number of publications studying the properties of these infra-slow fluctuations and their functional relevance have increased substantially, few studies have focused on explaining the underlying biophysical properties which give rise to these infra-slow fluctuations.

In order to understand how epilepsy and seizures influence the properties resting-state network fluctuations and their potential roles in altered cognitive and conscious states during and between seizures, we must first develop a better understanding of the underlying biophysical mechanisms by which these spontaneous infra-slow fluctuations arise. As previously mentioned, changes in ion concentration gradients have been proposed to underlie modifications to network-wide activity (Pedley et al., 1974; Chub and O'Donovan, 2001; Somjen, 2002; Bazhenov et al., 2004; Chub et al., 2006; Frohlich and Bazhenov, 2006; Frohlich et al., 2008b; Krishnan and Bazhenov, 2011; Wei et al., 2014a; Krishnan et al., 2015). These changes in relative ion concentrations have been reported to occur on slow time scales (McCreery and Agnew, 1983). Indeed, low amplitude $[K^+]_o$ fluctuations have been reported during resting-state activity over a long time period (McCreery and Agnew, 1983). Similarly, slow $[K^+]_o$ fluctuations have been recorded prior to seizure-like activity in animal model of epilepsy and have been suggested to underlie slow bursting dynamics in epilepsy (Pedley et al., 1974; Traynelis and Dingledine,

1988; Somjen, 2002; Ziburkus et al., 2013; Huberfeld et al., 2015). As such, it may be likely that the intrinsic mechanisms which regulate ionic homeostasis may influence spontaneous resting-state activity and give rise to the infra-slow time scale of these fluctuations.

Here, we explore the how ionic and synaptic homeostatic mechanisms give rise to and regulate network dynamics. We begin by first exploring the role of homeostatic synaptic scaling in the development of post-traumatic epilepsy and how age-dependent impairments in this homeostatic mechanism might explain the age-related differences in susceptibility to epileptogenesis following cortical trauma. We then explore the role of the KCC2 co-transporter in seizure initiation in genetic epilepsies characterized by K^+-channelopathies. Finally, we explore how ion concentration dynamics and their regulatory mechanisms give rise to and mediate spontaneous infra-slow resting-state network fluctuations.

Acknowledgments

Chapter 1, in part, is a reprint of the material as it appears in Ionic and Synaptic Mechanisms of Seizure Generation and Epileptogenesis 2019. González, Oscar C.; Krishnan, Giri P.; Timofeev, Igor; Bazhenov, Maxim. The dissertation author was the primary author of this paper.

Chapter 2: Homeostatic Synaptic Scaling and Age-Dependent Post-traumatic Epilepsy

Abstract:

Homeostatic synaptic plasticity (HSP) has been implicated in the development of hyperexcitability and epileptic seizures following traumatic brain injury (TBI). Our *in vivo* experimental studies in cats revealed that the severity of TBI-mediated epileptogenesis depends on the age of the animal. To characterize the mechanisms of these differences, we studied the properties of the TBI-induced epileptogenesis in a biophysically realistic cortical network model

with dynamic ion concentrations. After deafferentation, which was induced by dissection of the afferent inputs, there was a reduction of the network-wide activity and up-regulation of excitatory connections leading to spontaneous spike-and-wave type seizures. When axonal sprouting was implemented, the seizure threshold increased in the model of young but not the older animals, which had slower or unidirectional homeostatic processes. Our study suggests that age-related changes in HSP mechanisms are sufficient to explain the difference in the likelihood of seizure onset in young versus older animals.

Introduction:

Penetrating brain wounds or other forms of brain trauma commonly lead to epileptogenesis (Kollevold, 1976; Dinner, 1993; Temkin et al., 1995; Annegers et al., 1998; Topolnik et al., 2003a; Jin et al., 2006; Nita et al., 2007; Avramescu and Timofeev, 2008). Partial cortical deafferentation triggers the development of electrographic seizures within hours of the initial insult (Topolnik et al., 2003b; Nita et al., 2006). Following partial cortical deafferentation, epileptiform discharges were observed *in vitro* (Prince and Tseng, 1993; Xiong et al., 2011). *In vivo* studies in undercut cat cortex have revealed synaptic strength modulation and changes in intrinsic excitability (Avramescu and Timofeev, 2008), but the exact mechanisms leading to seizure generation following brain trauma remain to be understood.

Homeostatic synaptic plasticity (HSP) has been implicated in epileptogenesis following severe brain trauma (Houweling et al., 2005; Echegoyen et al., 2007; Trasande and Ramirez, 2007; Frohlich et al., 2008a; O'Leary et al., 2010; Volman et al., 2011a; Volman et al., 2011b). HSP is a slow negative feedback mechanism that maintains neural activity within a physiological range through activity-dependent modulation of synaptic strength and intrinsic excitability (Burrone and Murthy, 2003; Turrigiano, 2008; Pozo and Goda, 2010). It has been proposed that

this is achieved through the use of activity-dependent $[Ca^{2+}]_i$ sensors, TNFα and BDNF levels, as well as changes in Arc/Arg3.1 expression (Burrone and Murthy, 2003; Turrigiano, 2008; Pozo and Goda, 2010). In a normal network, HSP works to counter-balance Hebbian plasticity thereby preventing runaway excitation, and restricts the network activity to maintain network stability (Pozo and Goda, 2010). However, for chronic activity deprivation, as occurs after partial cortical deafferentation, HSP may fail to correctly compensate for the loss of network activity promoting hyperexcitability, and may potentially lead to paroxysmal synchronized bursting events (Houweling et al., 2005; Frohlich et al., 2008a; Volman et al., 2011a; Volman et al., 2011b).

Recent studies of epileptogenesis in animals of different ages revealed that older animals are more prone to epileptic seizures after traumatic brain injury than the younger ones (Timofeev et al., 2013). It was suggested that following recovery from injury, HSP may fail to control synaptic strength in deafferented areas leading to "overshooting" of synaptic strength and promoting epileptogenesis. In this study, we explored the hypothesis that HSP regulation is age-dependent and its changes may lead to epileptogenesis using a biophysically realistic cortical network model in which synaptic strengths are under homeostatic regulation, and the dynamics of intra- and extracellular ion concentrations are implemented to achieve realistic "*in vivo*-type" network dynamics. Following network deafferentation, we observed a decrease in the seizure threshold that was dependent on the severity of trauma. Implementing axonal sprouting rescued the normal physiological activity, but only when HSP was able to precisely control excitability. Impairment of the homeostatic down-regulation, as observed in older animals, increased severity of epileptogenesis and led to persistent epileptiform discharges as observed experimentally in the older, but not in the younger animals.

Results:

Trauma-induced epileptogenesis in vivo

Our previous studies have demonstrated that cortical undercut induces acute seizures stopping within several hours (Topolnik et al., 2003b). In head-restrained adult cats, the seizures were also developed in chronic conditions – weeks to months following the undercut in 70% of animals (Nita et al., 2007). Although cats are very tolerant to head-restrained conditions, some physiological artifacts, due to the unusual environment could be a factor that contributed to seizure generation. Therefore, in this study we performed continuous wireless electrographic and behavioral recordings for two-four months in four young (10-12 months old at the time of surgery) and one adult cat (older than 8 years at the time of surgery).

The acute seizures were recorded for 8-10 hours after the end of isoflurane anesthesia in all animals. The amplitude of electrical activity in the undercut suprasylvian area was lower as compared to other sites of intracortical recordings. The general dynamics of pathological 3-5 Hz rhythmic activity around the undercut cortex were not different from our previous study in terms of their spatial and temporal distribution (Nita et al., 2007). This electrical activity was recorded in the 8-year-old cat only. However, we observed new phenomena that had not been seen in head-restrained animals. The undercut cortex produced isolated large amplitude (~0.5 mV) slow waves. There were 18-20 periods of these slow waves per day in the first week following the undercut, and then their occurrence increased to about 50 periods per day. Within each period there were 2 to 40 slow waves none of which were rhythmic, and they occurred at most once every ten seconds. We have not observed these events in the head-restrained conditions in our previous experiments (Nita et al., 2007).

After six weeks, rare large paroxysmal electrographic events developed in the adult cat only. The full-blown seizures accompanied with motor jerks developed at the end of the third month. Most of the seizures were detected in the waking state, within a minute of transition from either slow-wave or REM sleep (figure 2.1A). In this animal, the highest amplitude of slow-waves during slow-wave sleep were recorded in both right and left somatosensory cortices (figure 2.1 B1, B2, green traces) and the lowest amplitude was recorded in the undercut cortex (figure 2.1 B1, B2, black traces). During seizure, the maximal local field potential (LFP) amplitude was recorded in marginal gyrus (figure 2.1, B1, B2, red trace) followed by left postcruciate gyrus (figure 2.1 B1, B2, upper green trace). Both these recording sites were surrounding the undercut cortex, suggesting that the areas surrounding the undercut cortex play a leading role in seizure generation. After the end of the seizure the cat awakened as demonstrated by activated LFP pattern in visual cortex and was at physical rest as evidenced by an absence of movements, low neck muscle tone, and strong mu rhythm recorded over somatosensory cortical areas (figure 2.1 D1, D2).

In our previous experiments, about 70% of cats developed seizures in chronic conditions after undercut (Nita et al., 2007). These animals were of unknown age. Here we reanalyzed these data. Out of 6 animals, the two that did not develop epilepsy within 3-4 months of observation were the cats that weighed 1.9-2.2 kg. The cats that developed epilepsy within the first several months from the undercut weighed 2.3-3.9 kg; veterinary examination did not consider these cats to be obese. The cats that weighed more than 2.3 kg were most likely fully adult. This further suggests that cortical undercuts lead to the development of epilepsy only in adult cats.

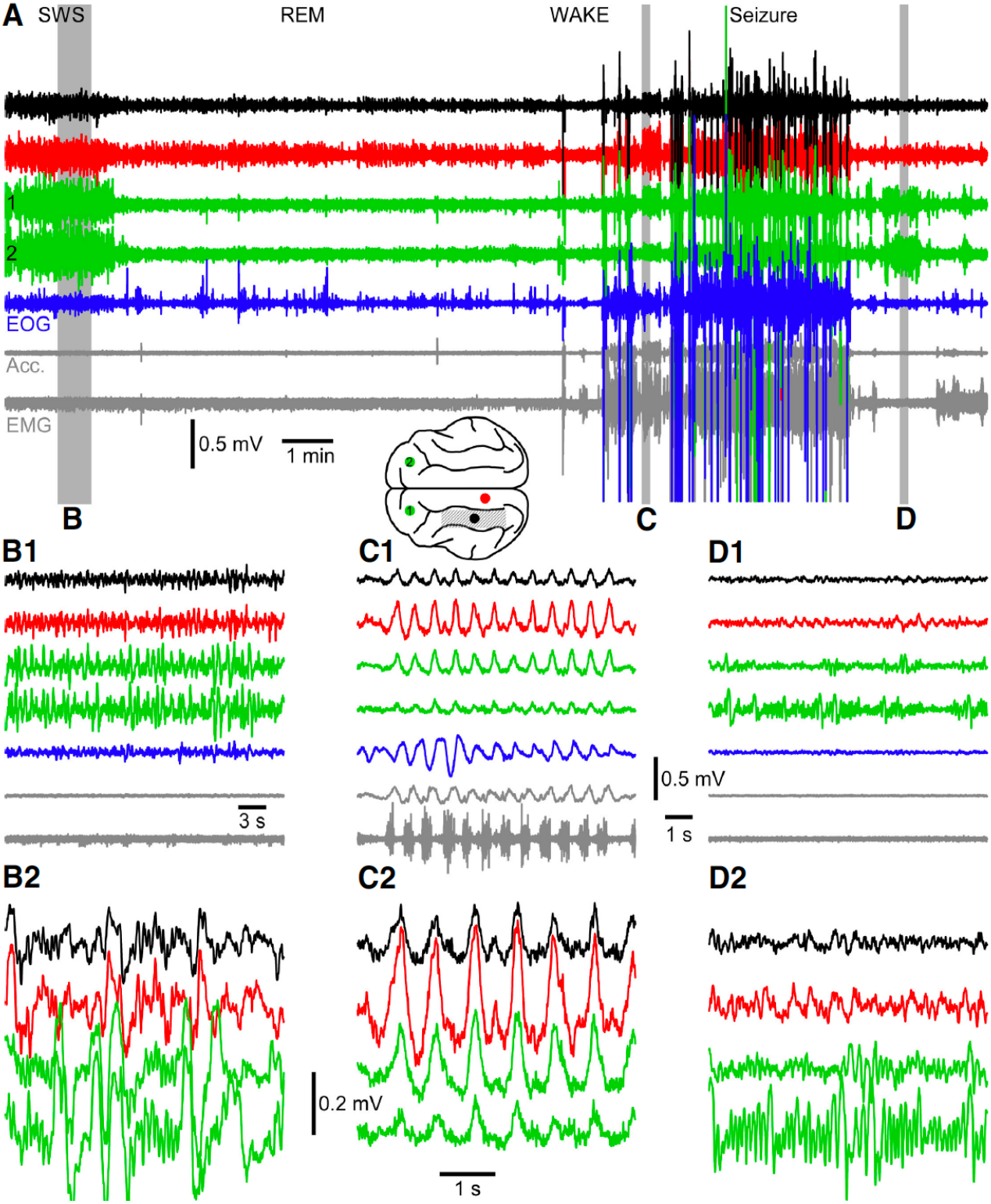

Figure 2.1 Cortical undercut leads to electrographic seizures *in vivo*. A, Transition between slow-wave sleep (SWS), rapid eye movement sleep (REM), waking state and seizure. Brain drawing shows location of intracortical local field potential electrodes. The other traces are EOG – electrooculogram, Acc – accelerometer and EMG – electromyogram. Segments of recordings indicated by the grey area are expanded in time in **B1** (SWS), **C1** (Seizure) and **D1** (Postictal recovery). Further expansion in time and amplitude is shown in panels **B2**, **C2** and **D2**.

Partial cortical deafferentation triggers seizure-like activity in the network model

Following our previous studies (Timofeev et al., 2000; Topolnik et al., 2003b, a; Houweling et al., 2005; Frohlich and Bazhenov, 2006; Frohlich et al., 2008b; Frohlich et al., 2008a; Timofeev et al., 2010; Volman et al., 2011a; Volman et al., 2011b), partial network deafferentation was used as a computational model of TBI. The network model incorporated populations of synaptically coupled excitatory pyramidal cells and inhibitory interneurons. In addition, realistic ion concentration dynamics were implemented to simulate *in vivo*-like conditions (see Methods for details). HSP was implemented to maintain a target firing rate by up- or down-regulation of synaptic strength. To achieve feasible simulation times, the HSP scaling rate was significantly increased to achieve much faster than physiological scaling.

In an intact, non-deafferented network, application of a low amplitude 1 sec current pulse stimulus to all pyramidal neurons was unable to elicit seizure activity (figure 2.2A-C). The brief stimulus caused a small transient increase in network activity reflected in the rise of the mean firing rate of the network (figure 2.3A, red trace). Prior to the stimulus, the network firing rate was fairly constant around the target firing rate of 5 Hz. At the onset of the stimulus (300 sec in figure 2.3A), the firing rate of the network increased to ~10 Hz, but quickly returned to the baseline following termination of the current pulse. Increase in the network mean firing rate was accompanied by small transient increases in extracellular potassium ($[K^+]_o$) and intracellular sodium ($[Na^+]_i$) concentrations, which then returned to the baseline shortly after the stimulus ended (figure 2.3D red traces). The firing pattern of this intact network remained unperturbed, showing spontaneous activity across the entire network (figure 2.2A-C).

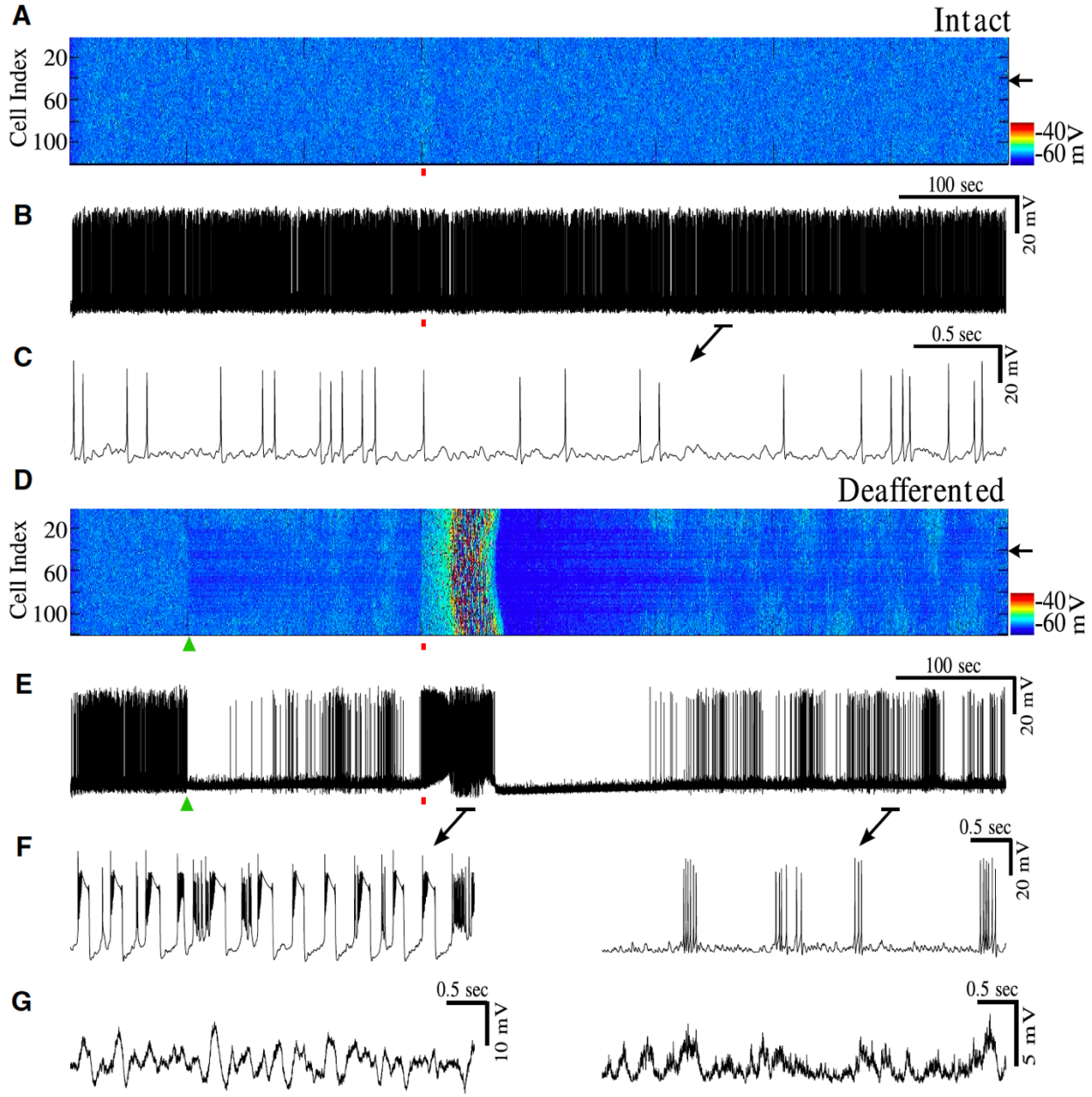

Figure 2.2 Network deafferentation leads to reduction of seizure threshold. A, Raster plot of activity in control network without deafferentation. Brief 1s stimulus was applied at 300s (red bar). **B**, Single cell activity from control network in **A** (location indicated by arrow). **C**, Zoom in of activity from **B** showing spontaneous firing pattern. **D**, Raster plot of activity of a network with 50% deafferentation applied at 100s (green triangle). Stimulation was applied at 300s (red bar) of equal duration and strength as that applied in **A**. **E**, Single cell activity from the deafferented network in **D**. **F**, Left, synchronized bursting events with spike inactivation during spike and wave seizure-like activity in **E**. Right, background bursting firing pattern generated between seizures. **G**, Left, LFP of the network corresponding to the spike and wave epileptiform activity shown in **F** (left). Right, the LFP corresponding to background bursting in **F** (right).

Inducing 50% deafferentation (afferent input was reduced by half) (green triangle, figure 2.2D) to a middle region of 80 neurons (out of a total of 120 neurons) led to an immediate decrease of activity in the region affected by the deafferentation (figure 2.2D, figure 2.3A black). This triggered homeostatic up-regulation of excitatory synaptic connectivity leading to the slow recovery of the network firing rate (figure 2.3A, see the time interval 100-200 sec). Figure 2.2E shows the voltage trace of a single representative neuron within the deafferented region, and the reduction in activity of the neuron following deafferentation. Extracellular potassium concentration (figure 2.3D black trace and figure 2.3E) was also slightly reduced as a result of the deafferentation. Synaptic weights between pyramidal neurons progressively increased (figure 2.3B black trace) through HSP regulation in response to the reduction of firing rate.

Upon application of external stimulus to the deafferented network (figure 2.2D red bar; strength same as figure 2.2A), the network generated seizure-like activity. We found a significant reduction in the seizure threshold: seizure-like activity could be generated in the deafferented network using only 4% of the stimulus strength needed to induce seizure-like activity in the intact network. Pathological activity showed characteristic state transitions between fast runs and spike-and-wave complexes, followed by spontaneous termination and post-ictal depression (figure 2.2D, E) resembling *in vivo* recordings of electrographic seizures (Topolnik et al., 2003b). The LFP during the fast runs and spike-and-wave complexes in the model (figure 2.2G) resemble the LFPs recorded *in vivo* in figure 2.1. Following post-ictal depression, the baseline firing rate of the deafferented network fluctuated around the target firing rate of 5 Hz. However, there was a marked difference in the network baseline firing pattern after deafferentation. Unlike asynchronous spontaneous firing observed in the intact network (figure 2.2 A-C), the neurons showed isolated bursting events following deafferentation (figure 2.2 D-F, right). Bursting was

observed independently of the seizure episodes suggesting that the origin of this pattern was purely a consequence of network deafferentation.

The dynamics of network activity can be illustrated by following the trajectory in a reduced phase space of the average synaptic weights plotted against the average firing rate (figure 2.3C). Without deafferentation (figure 2.3C, red), the state of the network was in a fixed point–like attractor and stayed there for the duration of the simulation. Following 50% deafferentation, the network state drifted away from the fixed point (figure 2.3C, black) due to HSP-mediated increase in synaptic weights. It approached a limit cycle-like attractor corresponding to the slow oscillatory dynamics of the baseline activity. In this state, the network was sensitive to small perturbations; thus, a small external stimulus could trigger a seizure. The seizure-like activity resulted in a rapid rise in the firing rate followed by a return of oscillations (figure 2.3C, spike in black plot).

Analysis of the $[K^+]_o$ (figure 2.3D-E) suggested that the seizure onset was triggered by a positive feedback mechanism. Following external stimulation, $[K^+]_o$ in the region of the network affected by deafferentation reached a level high enough to increase excitability and neuronal firing; that further increased $[K^+]_o$ leading to seizure onset (figure 2.3 D-E). During seizure-like activity $[K^+]_o$ reached as high as 7 mM, while the $[Na^+]_i$ reached 22.5 mM; in contrast, the levels of $[K^+]_o$ and $[Na^+]_i$ in the intact network remained around 4 mM and 20 mM, respectively (figure 2.3D, red traces). $[K^+]_o$ and $[Na^+]_i$ levels remained high in the intact regions of the deafferented network compared to the baseline levels in the non-deafferented network (figure 2.3E, F). Dynamics of $[K^+]_o$ and $[Na^+]_i$ determined the spike-and-wave pattern of the epileptic seizure and its termination. As previously shown, $[K^+]_o$ increases during fast runs and decreases during the spike-and-wave phase mediating periodic transitions between the two dynamic states in the

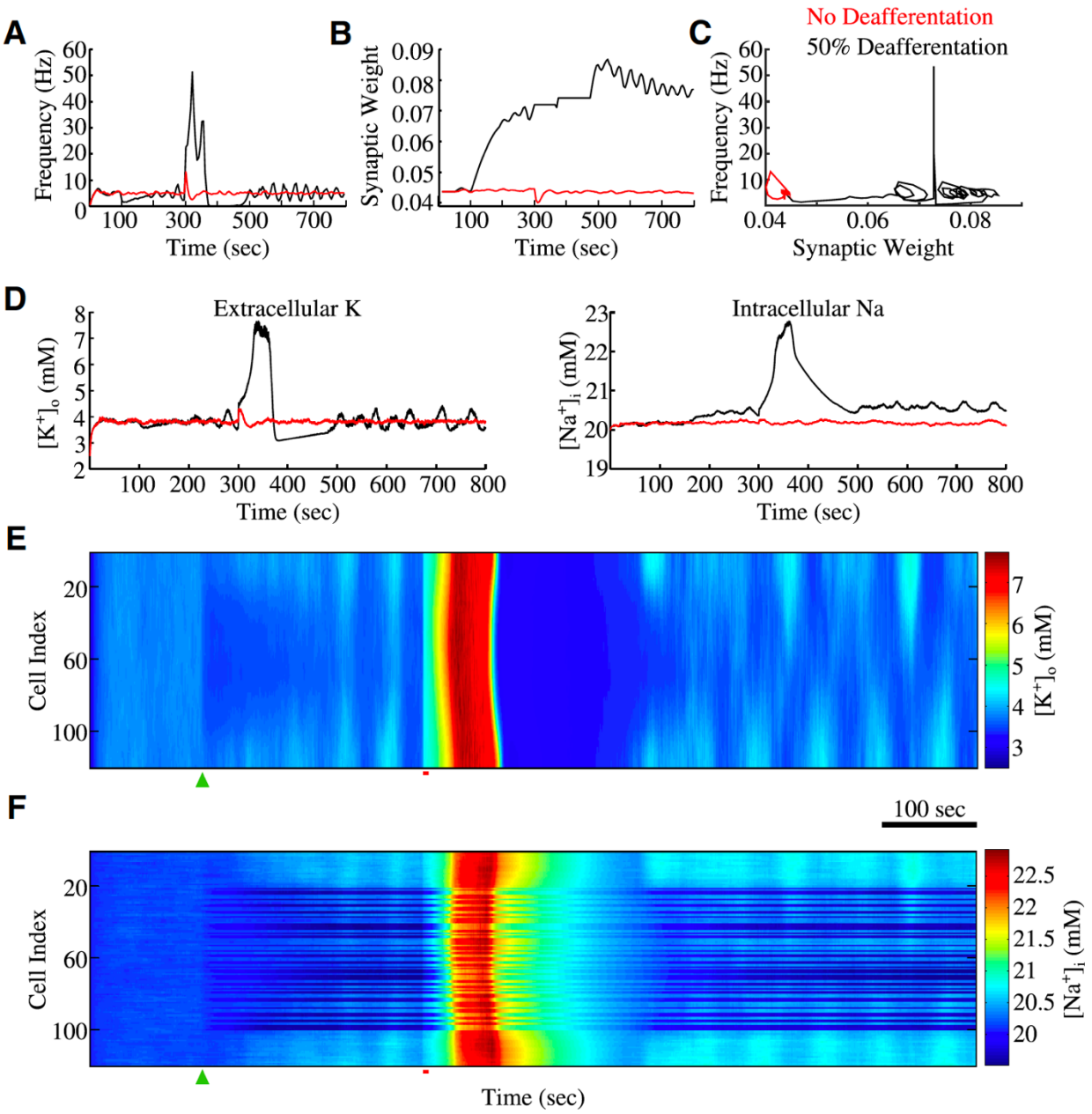

Figure 2.3 Synaptic weights and ion concentration dynamics. A, Average firing rate a network without deafferentation (red) and network with 50% deafferentation (black). **B**, Average synaptic weight dynamics. HSP scaling was blocked during seizure state to avoid un-physiologically fast changes of synaptic weights. **C**, Phase space projection shows dynamics of the averaged network firing rate and synaptic weight for intact (red) and deafferented (black) networks. **D**, Left (right), evolution of the extracellular potassium (intracellular sodium) concentrations near (from) a single cortical pyramidal neuron. **E**, **F**, raster plots of extracellular potassium and intracellular sodium concentrations respectively, for the network with deafferentation. Time of deafferentation is indicated by the green triangle, and stimulus application is indicated by red bar.

presence of bistability between fast runs and spike-and-wave complexes (Frohlich et al., 2005; Frohlich and Bazhenov, 2006). Progressive increase of $[Na^+]_i$ over the course of seizure eliminated the bistability leading to termination of the seizure and a post-ictal depression state (Krishnan and Bazhenov, 2011).

We found that stimulation of the deafferented network during either the peak or trough of the slow baseline $[K^+]_o$ oscillation did not significantly affect seizure threshold. While we previously reported dependence of the threshold for seizure onset on the level of $[K^+]_o$ (Frohlich et al., 2010), fluctuations of the baseline $[K^+]_o$ reported here were too small (<1 mM) to produce a significant change of the seizure threshold.

In this model, seizure-like activity started first near the center of the network. This was likely because there were enough intact neurons within the deafferented region to trigger a seizure. In networks with more severe deafferentation (e.g. 90% deafferentation in figure 2.5), there were fewer active neurons within the deafferented region, but neurons from the intact part of the network stimulated activity near the border of the intact and deafferented regions; that area became a primary site for seizure initiation.

Severity of deafferentation determines seizure threshold

We next explored the effects of the severity of deafferentation on seizure threshold. We began by keeping the size of the deafferented region constant while varying the percent of deafferented neurons within the affected region. In a 1D network of 120 PY neurons, an affected region of 80 contiguous neurons was chosen, and within these 80 neurons the percent of deafferented neurons was varied. Starting with a network with 0% deafferentation (all neurons were left intact) and increasing the severity of the trauma to 100% deafferentation (all 80 neurons experienced partial deafferentation) there was a significant decrease in seizure threshold

(figure 2.4A). In intact non-deafferented networks, seizure-like activity could still be induced by a sufficiently strong current pulse (100% in figure 2.4 A, C). Similar to the seizures in the deafferented network, the intact network exhibited characteristic fast run and spike-and-wave complex state transitions, and large increases in $[K^+]_o$ as well as increases in $[Na^+]_i$. With a small deafferentation (<10%) the seizure threshold was reduced but remained relatively high (figure 2.4A). Deafferentation of 10% of the neural population (figure 2.4B) resulted in a seizure threshold of 70% of the stimulus strength necessary to evoke seizure in intact network. In that case, reduction in the network baseline activity following deafferentation (green triangle) was relatively small. Nevertheless, even such minor "trauma" led to appearance of isolated bursting events (similar to that shown in figure 2.2F, right).

The seizure threshold quickly reduced with deafferentation of 20% and higher; 50% deafferentation produced the lowest seizure threshold of about 4% of that in the intact network (figure 2.4A). This condition (50% deafferentation) was chosen for simulations shown in figures 2.2 and 2.3. Increasing deafferentation to 100% led to a small increase in seizure threshold as compared to that in the model with 50% deafferentation. The remaining intact (and therefore, more active) neurons at the intermediate levels of deafferentation (e.g., 50%) could likely help initiate seizure; this can explain the minor threshold increase when an entire population was deafferented. In these simulations, although seizure initiation threshold became very low with increasing size of deafferentation, spontaneous seizures were not generated. Independent of the severity of the trauma, all seizure-like events exhibited characteristic fast run and spike-and-wave complex state transitions and increases in $[K^+]_o$. Additionally, all but the fully intact network developed isolated bursting following deafferentation.

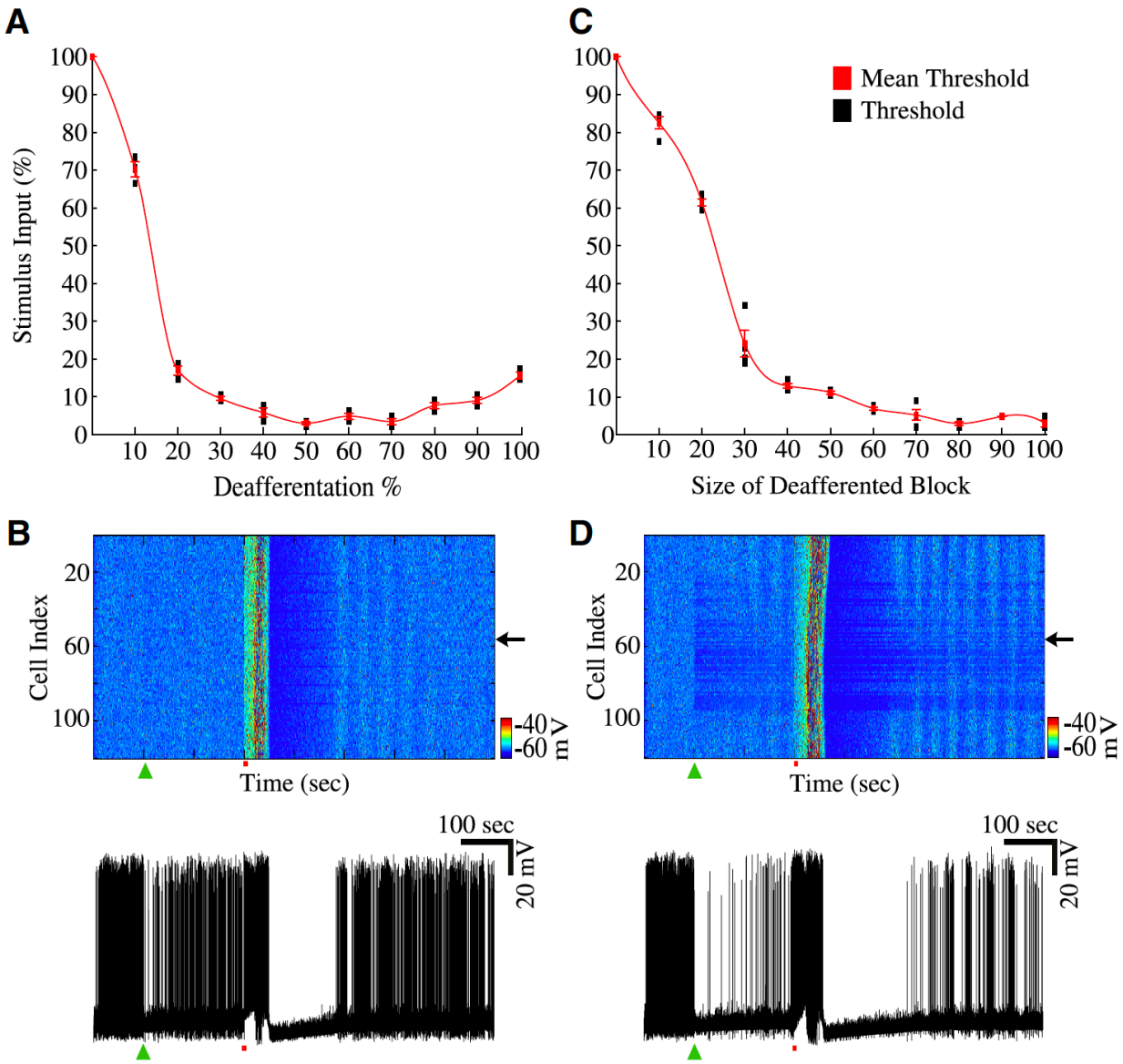

Figure 2.4 Severity of deafferentation affects seizure threshold. A, Threshold values for different degrees of deafferentation. Red line shows the mean threshold for a given degree of deafferentation, black bars give a range of thresholds from individual simulations. **B**, Raster plot of activity from a network with 10% deafferentation (green triangle). Bottom, activity of a single neuron from the network (top panel); location is indicated by the arrow. **C**, Threshold values for different sizes of deafferented area. **D**, Raster plot of activity from a network with a block of 70 neurons undergoing 50% deafferentation (green triangle). Bottom, activity of a single neuron from the network.

We then tested the effect of the size of deafferented region on the susceptibility of the network for seizure generation by changing the number of neurons in the affected region (i.e. 80 neurons for the previous condition) and applying 50% deafferentation (approximately 40 neurons were deafferented out of 80 neurons for the previous condition). Increasing the size of the affected region from 0 neurons to a block of 100 neurons also showed a significant change in

seizure threshold (figure 2.4C). Affected regions of 10 to 20 neurons resulted in a small decrease of threshold (>60% of that in intact network), very similar to the small change in seizure threshold observed in the 10% deafferented condition (figure 2.4A). Deafferented regions of 30 to 100 neurons, however, led to much larger decrease of the seizure threshold. When 100 neurons were deafferented, the seizure threshold reduced to only 3% of that in the intact condition. figure 2.4D shows a network with a deafferented region of 70 neurons. Surprisingly, this network produced a seizure pattern that was very similar to that in the network with only 10% deafferentation (figure 2.4B). Unlike the results from varying the percent of deafferented neurons (figure 2.4A), we did not observe an increase in threshold as the size of the affected region approached 100 neurons. Although both of the trauma conditions resulted in very low seizure initiation thresholds, varying the size of the deafferented region showed a smoother drop in threshold (figure 2.4C) as opposed to the abrupt drop in figure 2.4A. As was the case with varying the percent of neurons being deafferented, varying the size of the affected region did not result in the generation of spontaneous seizures.

Seizure-like events start near the boundary between intact and deafferented regions

To study spatio-temporal properties of initiation and spread of seizure-like activity, we increased the size of the network to 200 neurons leaving an intact region of 60 neurons on either side of the deafferented area of 80 neurons in the center of the network (figure 2.5A). We then applied 90% deafferentation (figure 2.5A, green triangle). As in the previous experiments, prior to the “trauma” the network displayed an asynchronous firing pattern. After deafferentation, we observed an immediate and strong drop in activity of the deafferented region. A brief, 1 s stimulus applied to the entire population of neurons (red bar) evoked seizure-like activity. figure 2.5B provides a closer look at the spatio-temporal pattern of activity near the time of stimulation.

The stimulus (red bar) triggered tonic firing which lasted about 20 s before transitioning to spike-and-wave bursting activity. In all models of epileptiform activity reported in this study, $[K^+]_o$ increased during fast runs and decreased during spike-and-wave bursting phase (Frohlich et al., 2005; Frohlich and Bazhenov, 2006). This created a bistability between two dynamic network states for a range of $[K^+]_o$ mediating transitions from tonic firing to spike-and-wave bursting.

We observed that epileptic bursts initiated at the boundaries between intact and deafferented regions (figure 2.5B) and then propagated outward to the rest of the network. A closer look at a single neuron near the boundary and a neuron from the center of the deafferented region revealed the delay in the onset of transition from fast runs to spike-and-wave complexes (figure 2.5C, D), thus indicating that the synchronized activity propagated away from the boundaries and well inside the intact and deafferented regions. Seizure-like activity in the intact regions of the network appeared to last longer than that in the deafferented region. These results are consistent with our new experimental findings (figure 2.1), which reported that the seizure amplitude was highest near the boundary of the undercut area, and with the previous experimental studies showing that seizure initiation *in vivo* occurs near the boundary between intact and deafferented regions (Nita et al., 2007). Unlike the neurons located well inside deafferented region, neurons near the border receive synaptic input from active intact neurons while some of their excitatory connections are homeostatically up-regulated. This combination of up-regulated synaptic strength and strong synaptic input made these neurons hyperexcitable and primed for seizure (Volman et al., 2011a).

Spontaneous vs. evoked epileptiform events

To test effect of HSP properties on seizure threshold, we varied the rate of homeostatic scaling (α_{HSP} , which is the rate at which synaptic weights change during HSP, see Methods for

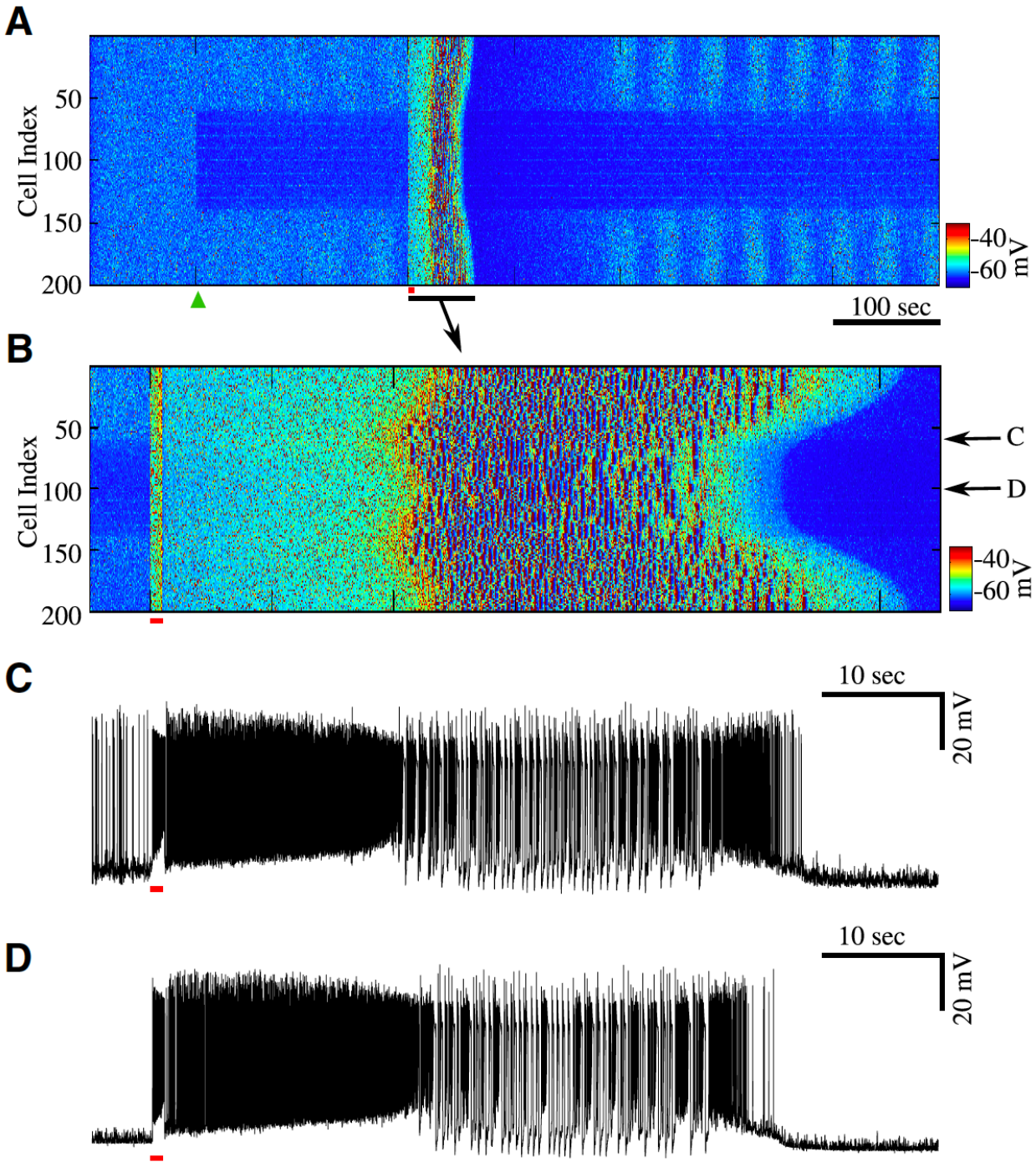

Figure 2.5 Seizures initiate at the boundaries and propagate towards intact and deafferented regions. A, Raster plot of activity from a network with 90% deafferentation applied at 100sec (green triangle) followed by stimulus at 300sec (red bar). **B**, Zoom in the raster plot of activity during one episode of seizure in **A**. **C**, **D**, Single cell activity from the network in **B**; locations are indicated by the arrows. Note bursting with spike inactivation followed by tonic spiking (fast run) just before termination of seizure.

details); higher scaling rate manifested faster, but also less accurate adjustment of synaptic weights. Spontaneous seizures were generated after 50% deafferentation (similar to conditions presented in figure 2.2) when the rate of homeostatic scaling was increased from 0.01 to 0.06, and the update time for synaptic weights was increased from every 5 s to every 20 s (figure 2.6A, B). Less precise synaptic scaling at higher rates prevented fine adjustments of synaptic weights thereby making the network more prone to overcompensate for the loss of activity and increase its propensity for seizure. Physiologically, this effect could result from the feedback delay between increase of synaptic strength and changes of the ambient glutamate level sufficient to stop synaptic up-regulation. These spontaneous seizures exhibited characteristic fast runs and spike-and-wave complexes (figure 2.6B) and were accompanied by a large increase in the network mean firing rate, with a maximum rate reaching 65 Hz, and large increases of synaptic weights (figure 2.6C, D). The network generated the first spontaneous seizure about 100 s after the deafferentation, with about 250 s between seizure-like events (figure 2.6A). Post-ictal depression lasted for about 100 s. Before the first seizure onset, synaptic weights reached higher level than that in the model with a slower and more precise HSP rate (compare figure 2.3B with 2.6D), which could explain the occurrence of spontaneous seizures. This experiment suggested that precise regulation of the HSP scaling may have an important impact on the network dynamics.

Effects of axonal sprouting on seizure threshold

Local axonal sprouting has been observed in cortex following cortical deafferentation (Carmichael and Chesselet, 2002; Avramescu and Timofeev, 2008; Timofeev et al., 2013; Kusmierczak et al., 2015). Connection probabilities progressively increased up to 6 weeks after cortical undercut was administered in cats (Avramescu and Timofeev, 2008). Axonal sprouting

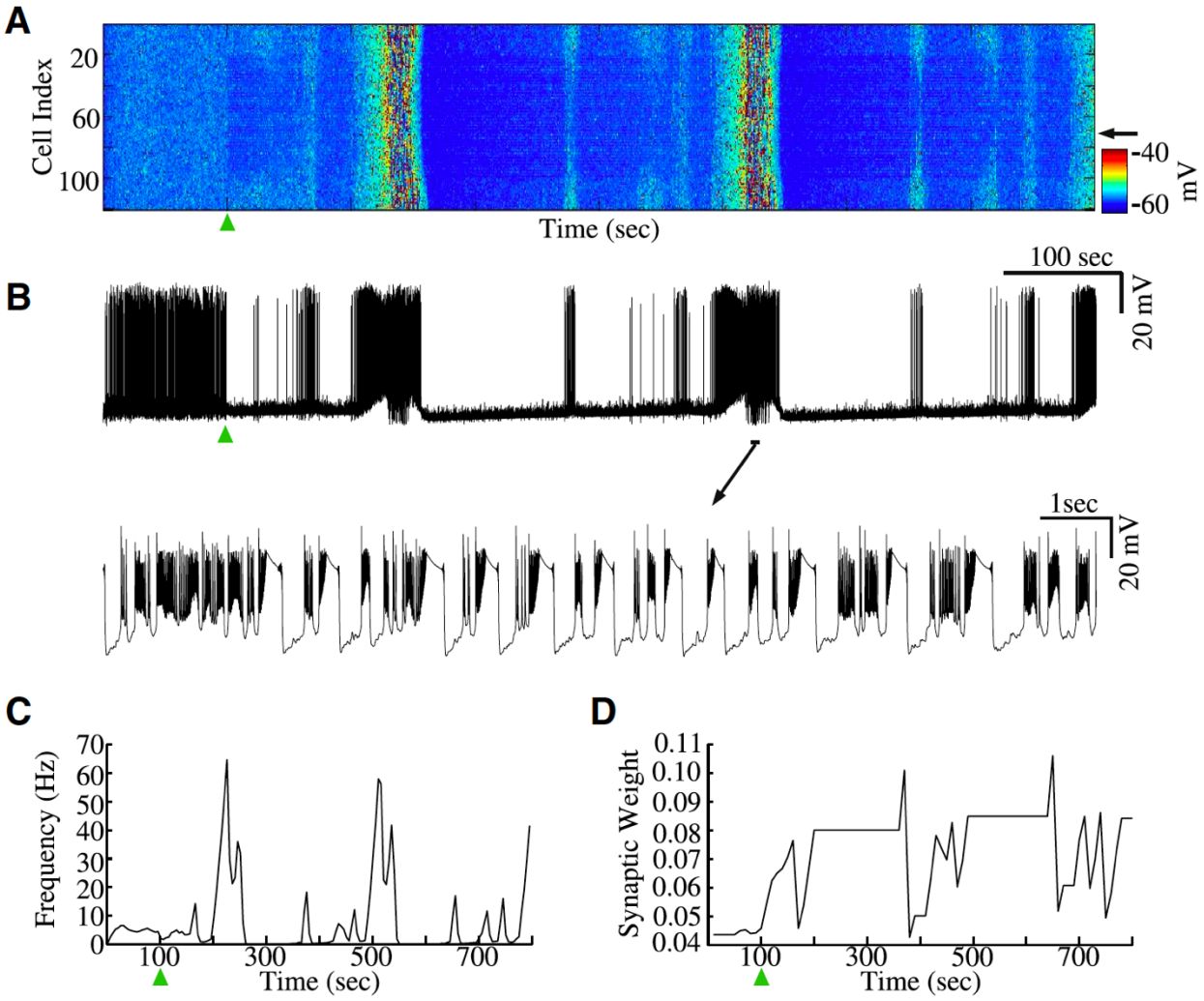

Figure 2.6 Spontaneous epileptiform events. A, Raster plot of activity with spontaneous, recurrent seizure-like events. Deafferentation time is indicated by the green triangle (α_{HSP} = 0.06 and check time = 10 sec). **B**, Top, single cell activity from the network in **A** (black arrow). Bottom, zoom in shows individual bursts with spike inactivation during seizure. **C**, Average firing rate of the network in **A**. **D**, Mean synaptic weights dynamics as a function of time for the network in **A**. HSP scaling was blocked during seizure state to avoid un-physiologically fast changes of synaptic weights.

in response to cortical trauma was found to be regulated by synchronous network activity after the trauma (Carmichael and Chesselet, 2002). To study the effect of trauma-induced axonal sprouting on seizure threshold and generation, we implemented a recovery process which modeled the axonal sprouting observed following brain trauma, and which regulated the amount of external input received by the deafferented population of neurons. This model of axonal

sprouting was only applied to deafferented neurons, and the level of input was not allowed to exceed that in the intact network.

Because both homeostatic scaling and axonal sprouting may vary with age, we varied the rate of both processes in our model and tested the effect of these changes on the seizure threshold (figure 2.7A). In general, we found that as the sprouting rate increased the threshold for seizure generation also increased. For high sprouting rates, increasing HSP rate, α_{HSP}, led to an increase in threshold. For networks with a very fast HSP rate (α_{HSP}= 0.06) and sprouting rate (γ_{Syn}= 0.001), the seizure threshold reached the level observed in a completely intact network (figure 2.7A, top/right). Figure 2.7B shows examples of the seizure threshold dynamics over time for two combinations of HSP and sprouting rate parameters (see 1 and 2 in figure 2.7A). We compared a "fast" network with faster HSP and faster sprouting rate (α_{HSP}= 0.005; γ_{Syn}= 0.001) to a "slow" network that had a slower HSP and slower sprouting rate (α_{HSP} = 0.001; γ_{Syn}= 0.0002). Fifty percent deafferentation was applied to both networks at the same time point (figure 2.7B, arrow). In figure 2.7B, early and late HSP are defined by the time elapsed following the initial cortical insult, early HSP was the time almost immediately after deafferentation and late HSP was the time when the target firing rate was fully recovered. From a clinical perspective, early HSP can be considered the time when early onset seizures are prevalent, and late HSP is when the incidence of late onset seizures is increased. The threshold values presented prior to the onset of the deafferentation represent the threshold for intact networks.

During early stages of HSP, the fast network had a lower seizure threshold than the slow network (figure 2.7B; compare the first point after deafferentation). However, as the time progressed, the fast network displayed a significant increase in the threshold level (>70% of

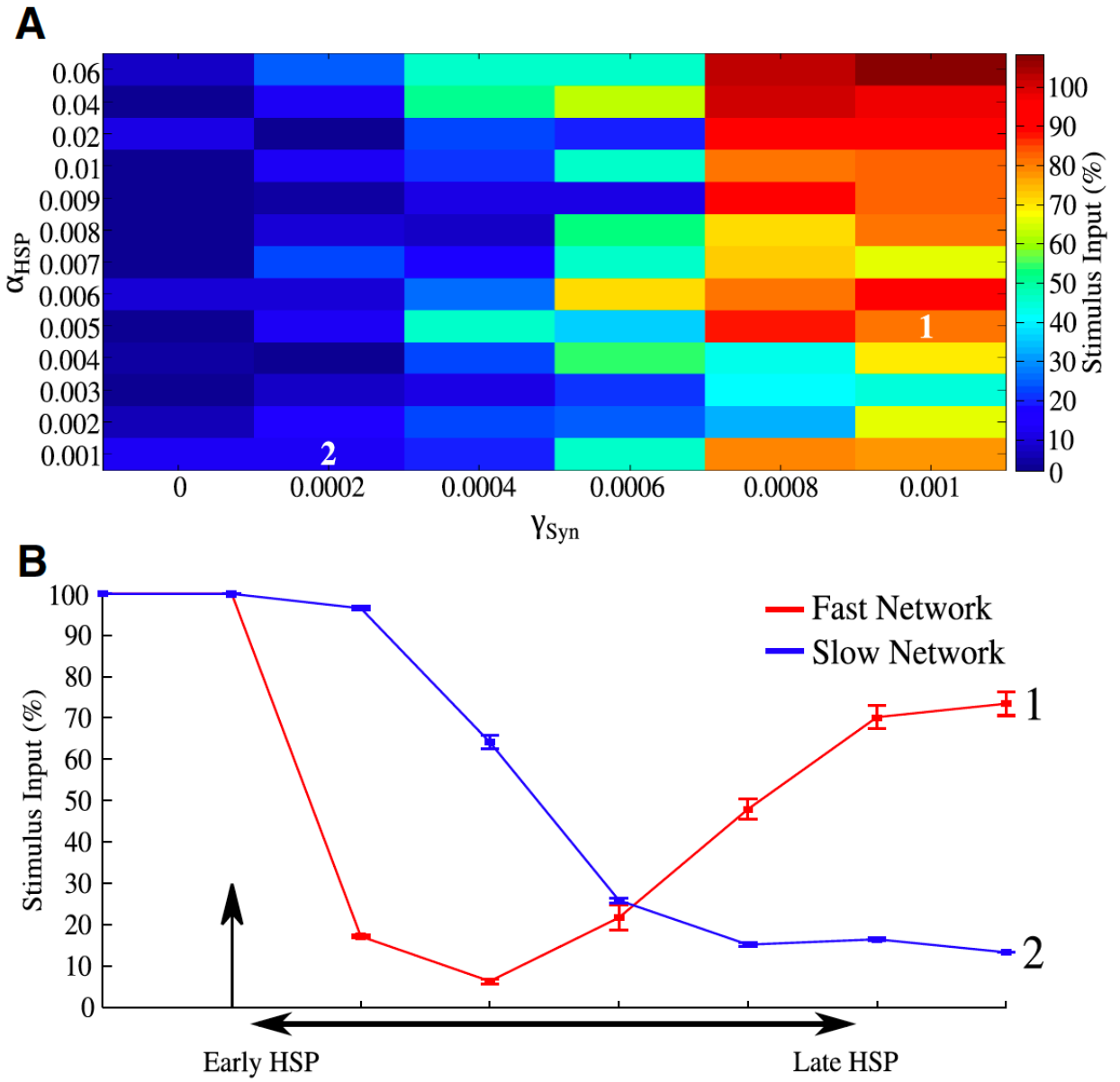

Figure 2.7 Effect of axonal sprouting rate on seizure threshold. A, Seizure threshold (color map) as a function of HSP α_{HSP} and sprouting rate, γ_{Syn}. All thresholds were tested in late HSP condition representing the last data points in panel **B**. The tiles numbered 1 & 2 correspond to the thresholds of the fast and slow networks in **B,** respectively. **B**, Threshold dynamics for two sample networks. Fifty percent deafferentation was applied at 100sec (arrow). The "fast" network (red) has a fast HSP and fast sprouting rate (α_{HSP} = 0.005, γ_{Syn}= 0.001) while the "slow" network (blue) has slow HSP and slow sprouting rate (α_{HSP} = 0.001, γ_{Syn}= 0.0002). Hundred percent represents seizure threshold of an intact network.

intact network) whereas the slow network's seizure threshold continued to decline. It should be noted that both networks, with the fast and slow HSP and sprouting rate in figure 2.7B, were able to fully recover their seizure thresholds after a substantial amount of time; however, the overall

duration of the time window when the threshold was reduced was much longer in the network with the slow sprouting rates. Experimental studies with cats (Timofeev et al., 2013) suggest that the age-related increase in seizure susceptibility following cortical deafferentation may be caused by the differences in homeostatic scaling and axonal sprouting. Indeed, our model predicts that it may be a plausible mechanism to explain the reduced likelihood of late onset seizure as seen in animal experiments, as well as in juvenile TBI patients compared to adult TBI patients.

Impact of impaired homeostatic down-regulation on seizure threshold

In the previous section, we showed that the differences in the properties of HSP scaling and axonal sprouting rate may explain why younger cats are less likely to develop seizures than older animals following severe brain trauma (Timofeev et al., 2013). Below we tested several specific mechanisms that could explain the difference between TBI impact on young and adult animals.

Experimental data suggest that different biophysical mechanisms are responsible for homeostatic up- and down-regulation, and that they may be differentially impaired with aging. Recent data (Sun and Turrigiano, 2011) revealed that down-regulation of synaptic strength in older animals may be impaired by increased expression levels of PSD-95 (see more in Discussion). We, therefore, proposed that homeostatic synaptic scaling may be less bidirectional in the older animal as compared to the young ones. As such, we tested the possibility of age-related changes in seizure susceptibility by varying the down-regulation of synaptic weights (α^-_{HSP}) while keeping up-regulation constant ($\alpha^+_{HSP} = 0.01$). First, we set the sprouting rate to zero. Following the onset of deafferentation, the network generated spontaneous seizures for values of $\alpha^-_{HSP} \leq 0.003$ (figure 2.8A). The seizure threshold was reduced (compared to a control network) for all values of $\alpha^-_{HSP} \leq 0.002$ (figure 2.8A inset). Reducing α^-_{HSP} to 0.001

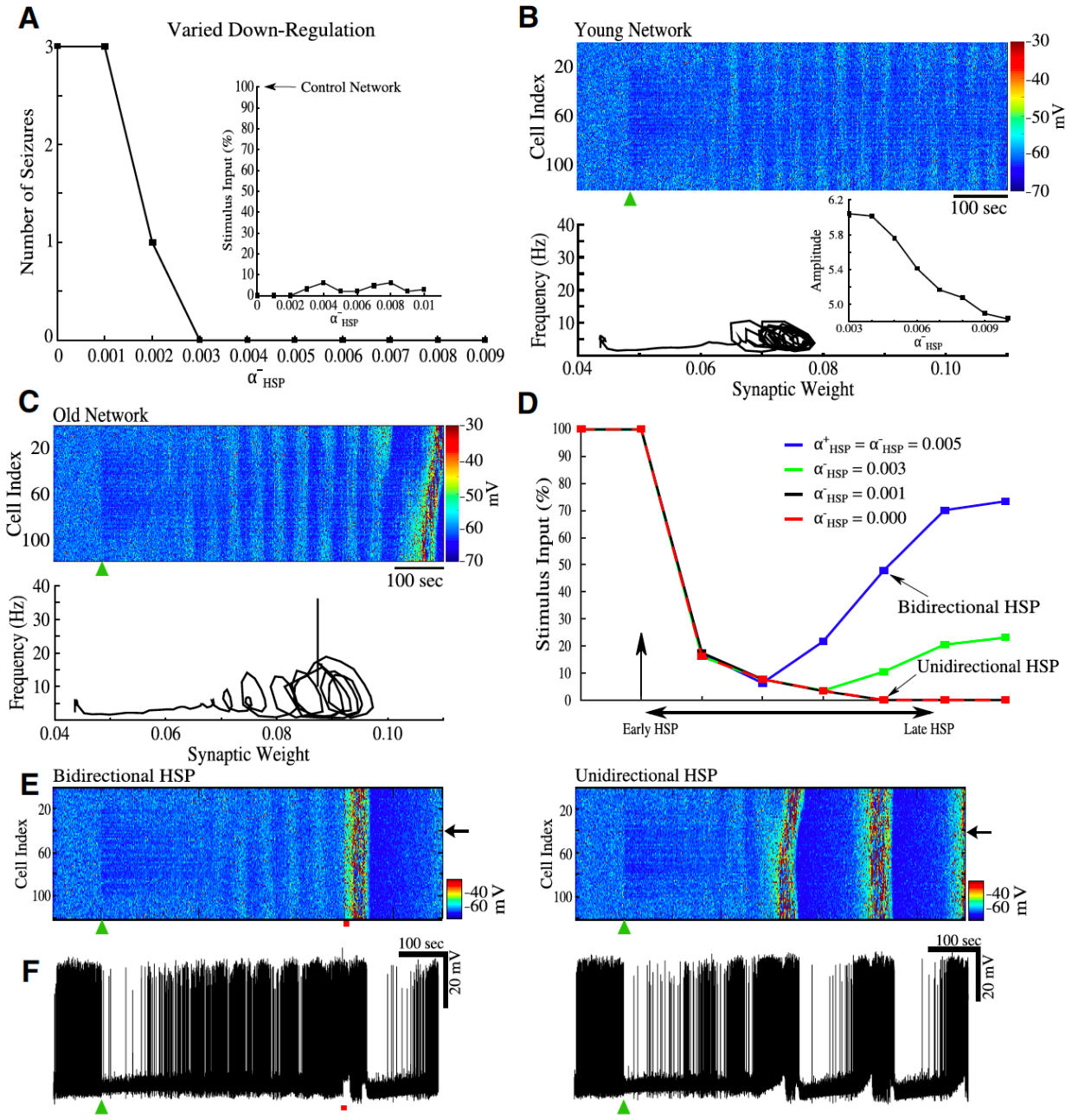

Figure 2.8 Seizure susceptibility in the "young" vs. "old" animal models. Fifty percent deafferentation was applied at 100 sec (black arrow or green triangle). **A**, Number of spontaneous seizures vs. HSP down-regulation rate, α^-_{HSP}. Inset shows the seizure thresholds for networks with different α^-_{HSP}. **B,** Top, Raster plot of activity of a network with $\alpha^-_{HSP} = 0.009$. Bottom, phase space projection shows dynamics of synaptic weights and averaged firing rate. Inset, amplitude of the steady-state oscillation in the phase space projections for values of $\alpha^-_{HSP} = 0.003 - 0.01$; these values did not produce spontaneous seizures. **C,** Top, Raster plot of the network activity for $\alpha^-_{HSP} = 0.002$. Bottom, phase space projection shows dynamics of synaptic weights and averaged firing rate leading to seizure. **D,** Time evolution of seizure threshold for networks with varying α^-_{HSP}. All networks implemented synaptic sprouting; vertical arrow indicates the time of deafferentation. **E,** Raster plots of the network activity with bidirectional HSP (left), and unidirectional HSP (right). **F**, Single cell activity from the networks with bidirectional (left) and unidirectional (right) HSP.

or removing down-scaling all together led to the generation of multiple recurrent spontaneous seizures in response to 50% deafferentation.

Figures 2.8B and C show examples of the networks with different degrees of impairment of the down-regulation processes. A network model with a slightly reduced α^-_{HSP} = 0.009, representing scenario of a "younger" animal (figure 2.8B), did not produce spontaneous seizures following deafferentation (green triangle in figure 2.8B). The phase trajectory of this network converged to a fixed point-like attractor (figure 2.8B, bottom). In the network model representing an "older" animal and having a larger reduction of $\alpha^-_{HSP} = 0.002$ (figure 1.8C), we observed recurrent spontaneous seizures (see the end of the simulation in figure 2.8C, top) and the phase trajectory converged to a limit cycle-like attractor in which the synaptic weights slowly oscillated along with the average firing rate (figure 2.8C, bottom).

Analysis of the network dynamics for α^-_{HSP} values which did not lead to spontaneous seizures (α^-_{HSP} = 0.003 – 0.01) revealed that the amplitude of the steady-state oscillations in the reduced phase space of the average firing rate plotted against synaptic weights increased as the α^-_{HSP} value decreased (compare figure 2.8B vs. 2.8C; see figure 2.8B insert) suggesting a dynamical mechanism of instability and seizure initiation in the models with imprecise synaptic scaling for lower α^-_{HSP} values.

Next, we explored the effects of impaired homeostatic down-regulation on seizure threshold in the presence of synaptic recovery. We tested this by determining the seizure thresholds of four different networks. Each network had the same sprouting rate but varied in the rate of homeostatic down-regulation of synaptic weights, α^-_{HSP} (figure 2.8D). Following deafferentation, all four networks had similar seizure thresholds at the early stages of the HSP. However, a clear-cut difference was found at the late stages of synaptic homeostasis. The

networks with less impaired α^{-}_{HSP} were able to recover some of the seizure threshold and prevent spontaneous seizure generation (figure 2.8D, blue and green lines). In contrast, the networks with more impaired α^{-}_{HSP} produced recurrent spontaneous seizures (figure 2.8D, black and red lines overlap in most of the plot). Even for very long simulation times, the unidirectional network, $\alpha^{-}_{HSP} = 0$, was unable to recovery its seizure threshold.

Representative examples of the network dynamics and activity of one pyramidal cell from a bidirectional ($\alpha^{-}_{HSP} = \alpha^{+}_{HSP}$) and unidirectional ($\alpha^{-}_{HSP} = 0$) network are shown in figures 2.8E and F. The green triangles in both plots indicate the time of deafferentation, and the red bar in figure 2.8E left indicates the stimulus used to induce seizure-like activity. The first spontaneous seizure generated in the unidirectional HSP network occurred 100 s prior to the evoked seizures in the bidirectional network. The bidirectional network never generated spontaneous seizures.

Discussion:

Previous theoretical studies predicted that synaptic up-regulation after severe brain trauma may lead to a hyperexcitable network where susceptibility for seizures is dramatically increased (Houweling et al., 2005; Frohlich et al., 2008a; Volman et al., 2011a; Volman et al., 2011b). Reduction of the seizure threshold after severe deafferentation is consistent with experimental studies where it was observed that cortical undercut increased local neuronal connectivity, which eventually increased network excitability and promoted seizures (Salin et al., 1995; Jin et al., 2006; Avramescu and Timofeev, 2008; Jin et al., 2011).

In this study we present *in vivo* experimental data and results of computer simulations to test the hypothesis that age-related changes in homeostatic synaptic plasticity (HSP) may be sufficient to explain the difference in the likelihood of seizure onset in young versus old animals.

Our study, based on detailed modeling of the interaction between homeostatic synaptic scaling and ion concentration dynamics, revealed that following deafferentation the threshold for seizure initiation recovers to a state close to that in an intact network for models of younger animals but remains low for models implementing HSP changes that may occur during aging.

Evidence for age dependence of trauma-induced epileptogenesis.

Our new *in vivo* data suggest a strong correlation between seizure susceptibility after brain trauma and the age of an animal. Adult cats in our study developed trauma-induced epilepsy but this was not the case in our young cats. Previous studies in rats revealed age-dependent differences in susceptibility to pharmacologically-induced seizure following cortical injury. $FeCl_3$ injection induced post-traumatic seizures in young (4 months) and old (18 months) rats, however, older rats were more susceptible to post-traumatic epilepsy than younger animals and exhibited both faster seizure spread and faster seizure onset (Jyoti et al., 2009).

Age-dependent differences in the development of TBI-induced epilepsy have been observed in human patients. One study reported that patients 65 years of age and older at the time of injury were more susceptible to the development of epilepsy than younger patients (Annegers et al., 1998). More recent study (Christensen et al., 2009) assessed the risk of developing epilepsy in children and young adults suffering from TBI. Taking into consideration age, severity of trauma, sex and family history, the study found that the risk of epilepsy was dependent on the severity of the trauma and the age of patient at the time of injury.

Role of HSP in epileptogenesis.

Reduced network activity, through bath application of TTX *in vitro* or through cortical deafferentation *in vivo*, leads to changes in synaptic strengths and increases in the excitability of the network (Topolnik et al., 2003a, b; Wierenga et al., 2005; Jin et al., 2006; Nita et al., 2006;

Echegoyen et al., 2007; Trasande and Ramirez, 2007; Avramescu and Timofeev, 2008; Ibata et al., 2008; Lemieux et al., 2014). It is generally accepted that these changes are caused by homeostatic plasticity - a regulatory mechanism, which maintains a target firing rate through up-regulation of excitatory intrinsic and synaptic factors and down-regulation of inhibitory factors (Burrone and Murthy, 2003; Rich and Wenner, 2007; Turrigiano, 2008; Pozo and Goda, 2010).

Our previous modeling studies explored the hypothesis that HSP may fail to control "normal" excitability in heterogeneous networks, where there are subpopulations of neurons with severely different levels of activity – conditions found in traumatized cortex (Houweling et al., 2005; Frohlich et al., 2008a; Volman et al., 2011a; Volman et al., 2011b). In these models HSP-dependent epileptogenesis was manifested by periodic bursting events; however, the realistic pattern of spike-and-wave seizures was impossible to reproduce because of the model simplicity. Changes of the ion concentrations can have profound effects on the network dynamics and may be responsible for the characteristic patterns of electrical activity observed during seizures. In particular, increase of $[K^+]_o$ during epileptic seizures functions as a positive feedback loop to depolarize the neurons and to make the network more excitable leading to further increase of $[K^+]_o$ (Somjen, 2002; Frohlich et al., 2008b; Krishnan and Bazhenov, 2011). The model presented in this study included dynamics of intra- and extracellular concentrations of K^+ and Na^+ ions, as well as intracellular concentrations of Cl^- and Ca^{2+}. In this model, seizure-like activity closely resembled *in vivo* intracellular recordings of spike-and-wave electrographic seizures in cats (Avramescu and Timofeev, 2008), which spontaneously terminate and are followed by an inter-ictal period.

Our model predicts the role of the severity of brain trauma in determining the susceptibility to seizure onset. It has been reported that cats that have undergone partial cortical

deafferentation are much more likely to have seizures when anaesthetized with ketamine/xylazine than cats that do not have cortical trauma (Topolnik et al., 2003a; Nita et al., 2006). Changing the degree of deafferentation in our model resulted in different thresholds for seizure generation such that larger deafferentation produced lower seizure thresholds; this is consistent with previously reported results in simplified models of the cortical network (Volman et al., 2011a). We found that the seizure activity could also be induced in a control, non-deafferented network by sufficiently strong stimulation. This result supports the idea of the presence of bistability in the cortical network with physiological and pathological attractors coexisting and having different basins of attraction in epileptic and non-epileptic brains (Frohlich et al., 2010).

In vivo data presented in our study suggest that state of vigilance may affect the transition from physiological activity to epileptic seizures. Neocortical seizures commonly occur during slow-wave sleep. One possible explanation depends on the presence of repetitive hyperpolarized down states in the cortex found during slow-wave sleep. It has been suggested that such periods of silence may lead to an increase in cortical excitability and may facilitate seizure onset (Timofeev et al., 2000; Topolnik et al., 2003b, a; Nita et al., 2006, 2007; Avramescu and Timofeev, 2008; Timofeev et al., 2010; Timofeev et al., 2013). Transition from sleep to waking is associated with activation of the cholinergic system and overall increase in excitability (Brown et al., 2012). Taken together it suggests that the time just after the sleep-wake transition, when the sleep-related increase in excitability is still in place and increase in excitability associated with cholinergic changes just occurred, would constitute ideal conditions for seizures to occur. Indeed, in our *in vivo* study, seizures always occurred shortly after transitions from sleep to waking states.

Mechanisms of age dependence in epileptogenesis.

Our *in vivo* study revealed that the outcome of trauma-induced epileptogenesis significantly depends on the age of an animal with older animals being much more prone to seizures. The multiplicative nature of HSP is of special interest in terms of age-related differences. The multiplicativity of HSP depends on the modulation of AMPA receptors that occurs at all synapses on a given neuron. This type of HSP is different from synapse-specific HSP expression (Echegoyen et al., 2007; Goel and Lee, 2007; Rich and Wenner, 2007; Turrigiano, 2008; Lee et al., 2014). Age-dependent differences in multiplicative vs. synapse-specific HSP expression in response to dark rearing was previously reported (Goel and Lee, 2007).

Thus, the properties of homeostatic scaling and/or the rate of axonal sprouting of the traumatized connectivity may be different in young and adult animals and may lead to different final states of the cortical network excitability. Impaired homeostatic down-regulation in the older animals will prevent full restoration of intact synaptic connectivity after recovery of synaptic input to affected areas, e.g., by axonal sprouting (Timofeev et al., 2013). Indeed, studies on spinal cord injury-induced sprouting and hippocampal deafferentation-induced sprouting have shown age-dependent differences (Schauwecker et al., 1995; Jaerve et al., 2011). Following trauma, increases in growth associated proteins (GAPs) occurred in the hippocampus of young rats (3 months old), but not in adult rats (24 months old).

In our model, we tested this mechanism by introducing a model of axonal sprouting processes, which worked to compensate for the afferent input lost during partial deafferentation. Our results revealed that the network with faster sprouting rate and homeostatic scaling displayed a rapid increase of seizure thresholds after initial decline, while the network with slow

synaptic sprouting and synaptic scaling displayed prolonged periods of seizure-like activity. Although the latter network eventually restored its initial high seizure threshold, we can speculate that older animals may have limited abilities for axonal sprouting and, therefore, synaptic projections to the undercut area may never fully recover leading to chronically reduced seizure threshold.

Homeostatic scaling is a bidirectional process that aims to maintain a target firing rate through the strengthening and weakening of synaptic connections. Most of the synaptic strength modulation involved in this process can be attributed to changes in synaptic AMPA receptor densities (Rich and Wenner, 2007; Hou et al., 2008; Pozo and Goda, 2010; Remme and Wadman, 2012). It was recently demonstrated that the scaffolding protein PSD-95 is necessary for synaptic scaling, and its role in scaling the synaptic strength was dependent on age and directionality of the scaling (Sun and Turrigiano, 2011). Expression levels of PSD-95 increased as the neurons aged and PSD-95 affected mainly the down-regulation of synaptic strength while up-regulation was much less affected. These results support our hypothesis that the down-regulation of synaptic strength in older animals may be more difficult to regulate leading to higher susceptibility to seizures (Timofeev et al., 2013). We found that impairing the sensitivity of the homeostatic scaling sensor not only reduced seizure threshold but also led to generation of spontaneous seizures.

Age-dependent changes of the homeostatic up-regulation may also contribute to seizure susceptibility. BDNF has been shown to be involved in the increase of AMPA receptor insertion following decrease in synaptic activity, but not to the removal of receptors in response to increased activity (Rutherford et al., 1998; Leslie et al., 2001; Turrigiano, 2008; Pozo and Goda, 2010). Additionally, BDNF expression levels have been shown to decrease with age

(Lommatzsch et al., 2005). Taken together these results suggest that reduced levels of BDNF in older animals could reduce the dynamic range of BDNF regulation of homeostatic up-scaling. This may lead to larger increases in AMPA receptor insertion in response to the smaller changes in BDNF expression in older animals as compared to younger ones and may provide a complimentary mechanism for age-dependent changes of the seizure susceptibility.

Strategies to prevent epileptogenesis.

Trauma-induced epilepsy is poorly controlled by anti-epileptic drugs (AEDs) (Hernandez, 1997; Chang et al., 2003; Temkin, 2003; Agrawal et al., 2006; Temkin, 2009). Administration of AEDs immediately following TBI reduces incidence of early seizure onset within the first week following brain insult (Annegers et al., 1998; Agrawal et al., 2006; Szaflarski et al., 2014), but rarely controls late seizures. Our study predicts that reduction of the neuronal excitability – a common target of the anti-epileptic drugs, e.g., levetiracetam (Szaflarski et al., 2014) – in some conditions can enhance HSP mediated synaptic up-regulation and increase severity of epileptogenesis. Thus, our study provides new insight into the development of interventions that can be used to treat TBI, which would target to maintain physiological level of activity in deafferented areas and thus reduce likelihood of epileptic seizures.

Methods and Materials:

In vivo experiments. All experiments were performed in accordance with the guideline of the Canadian Council on Animal Care and approved by the Université Laval Committee on Ethics and Animal Protection. Experiments were performed on cats of either sex. To create conditions that occur in penetrating wounds, the white matter underneath the suprasylvian gyrus (parietal cortex, area5 and 7) was transected under isoflurane anesthesia. The details of this

cortical undercut procedure were described previously (Topolnik et al., 2003b, Nita et al., 2007). The details of the surgery and simultaneous wireless LFP – behavioral recordings are described in (Grand et al., 2013). In these experiments, the intracortical LFP electrodes were inserted to a depth of 1 mm in undercut cortex (left suprasylvian gyrus), left posterior marginal gyrus (secondary visual cortex, area 18), and right and left postcruciate gyri (primary somatosensory cortex, area 6). To control for states of vigilance and to record seizure-associated movements, we implanted electrooculogram (EOG) electrodes in the inferior surface of the orbital plate of the frontal bone, electromyogram electrodes into the neck muscles, and an accelerometer (ADXL-330, Analog Devices, Norwood, MA, USA) was attached to the head bones. Continuous wireless recordings of electrographic and movement activities were achieved with NeuroWare W16-series system (Triangle Biosystems Inc., Durham, NC, USA). The wireless amplifier and battery were attached to the head and protected with a plastic housing. Head-restrained experiments were carried out identically to previous description (Nita et al., 2007). The experiments lasted for three to six months.

Analysis: All recordings were analyzed off-line using custom-written routines in IgorPro 4 (Lake Oswego, Oregon, USA).

Pyramidal cell and interneuron models. Pyramidal cells (PYs) and inhibitory interneurons (INs) were modeled as two-compartment neurons with dendritic and axosomatic compartments as described previously in detail (Mainen and Sejnowski, 1996; Kager et al., 2000; Bazhenov et al., 2004; Frohlich and Bazhenov, 2006; Krishnan and Bazhenov, 2011). The change in voltage for each compartment can be described by the following equations:

$$C_m \frac{dV_D}{dt} = -g_c^D (V_D - V_S) - I_D^{leak} - I_D^{pump} - I_D^{Int}$$

$$g_c^S (V_D - V_S) = -I_S^{leak} - I_S^{pump} - I_S^{Int}$$

where V_D is the voltage of the dendritic compartment, I_D^{leak} and I_S^{leak} are the sum of the ionic leak currents, I_D^{pump} and I_S^{pump} are the sum of the Na^+ and K^+ currents through the Na^+/K^+ pump, and I_D^{Int} and I_S^{Int} are the intrinsic currents for the dendritic and axosomatic compartments respectively.

The intrinsic current present in the dendritic compartment (I_D^{Int}) include the voltage-gated sodium current (I^{Na}), persistent sodium current (I^{NaP}), high-threshold calcium current (I^{Ca}), calcium-activated potassium current (I^{KCa}), slowly activating potassium current (I^{Km}), hyperpolarization-activated depolarizing mix cationic currents (I^h), and leak conductances. The axosomatic compartment (I_S^{Int}) consisted of the delayed-rectifier potassium current (I^{Kv}), voltage-gated sodium current (I^{Na}), the persistent sodium current (I^{NaP}), and the sodium-activated potassium current (I^{KNa}). All of these currents have been described in detail elsewhere (Krishnan and Bazhenov, 2011).

Ion concentration dynamics. This model exhibits changes in concentrations of $[K^+]_o$, $[K^+]_i$, $[Na^+]_o$, $[Na^+]_i$, $[Ca^{2+}]_i$, and $[Cl^-]_i$. The reversal potentials for each current calculated through the use of the Nernst equation for the specific ion or ions passing through the channel of interest. The concentration dynamics of these ions were modeled similar to previous work (Kager et al., 2000; Bazhenov et al., 2004; Frohlich and Bazhenov, 2006; Krishnan and Bazhenov, 2011) and are described as follows:

$$\frac{d[K^+]_o}{dt} = \left(\frac{k}{Fd}\right)\left(I_K^{pump} + I_{\sum K}^{Int}\right) + \delta_o\left(\frac{([K^+]_{o-1} + [K^+]_{o+1})}{2} - [K^+]_o\right) + \delta_o([K^+]_{oc} - [K^+]_o) + G$$

$$\frac{d[K^+]_i}{dt} = -\left(\frac{k}{F}\right)\left(I_K^{pump} + I_{\sum K}^{Int}\right) + \delta_i([K^+]_{ic} - [K^+]_o)$$

$$\frac{d[Na^+]_o}{dt} = \left(\frac{k}{Fd}\right)\left(I_{Na}^{pump} + I_{\sum Na}^{Int}\right) + \delta_o\left(\frac{([Na^+]_{o-1} + [Na^+]_{o+1})}{2} - [Na^+]_o\right)$$

$$+ \delta_o([Na^+]_{oc} - [Na^+]_o)$$

$$\frac{d[Na^+]_i}{dt} = -\left(\frac{k}{F}\right)\left(I_{Na}^{pump} + I_{\sum Na}^{Int}\right) + \delta_i([Na^+]_{ic} - [Na^+]_o)$$

$$\frac{d[Cl^-]_i}{dt} = -\left(\frac{k}{F}\right) I_{\sum Cl}^{Int} + \left(\frac{[Cl^-]_{i\infty} + [Cl^-]_i}{\tau_{Cl}}\right)$$

$$\tau_{Cl} = \left(100 + \frac{\tau_{Cl\infty}}{\left(1 + \exp\left([Cl^-]_{i\infty} - \frac{[K^+]_o}{\tau_{KoCl}}\right)\right)}\right)$$

$$\frac{d[Ca^{2+}]_i}{dt} = \frac{(-5.1819 \times 10^{-5} I_{Ca})}{D_{Ca}} + \left(2.4 \times 10^{-4} - \frac{[Ca^{2+}]_i}{\tau_{Ca}}\right)$$

where F = 96489 C/mol, the conversion factor k = 10, d = 0.15 determined the ratio of the extracellular compartment volume to the surface area, $[K^+]_{oc}$ and $[Na^+]_{oc}$ are the K^+ and Na^+ concentrations in the adjacent compartments, and $[K^+]_{o-1}$, $[K^+]_{o+1}$, $[Na^+]_{o-1}$, and $[Na^+]_{o+1}$ are the concentrations of K^+ and Na^+ in neighboring cells respectively. In this model, $[K^+]_o$ represents the concentration of the extracellular potassium immediately surrounding a given neuron. Additionally, extracellular K^+ was allowed to diffuse between the two compartments in the model and between the space volumes associated with neighboring neurons. G represents the

glial K^+ uptake. For the chloride dynamics, $[Cl^-]_{i\infty}$ = 5mM, $\tau_{Cl\infty}$ = 2x10^4, and τ_{KoCl} = 0.08s. As discussed in (Krishnan and Bazhenov, 2011), these values were chosen to match experimental data with regards to the role of $[K^+]_o$ on KCC2 co-transporter efficiecy. Values for τ_{Ca} and D_{Ca}were set to 300ms and 0.85 respectively.

Network and Synaptic Properties. The cortical network was modeled as a one-dimensional network which consisted of 120 PYs and 24 INs. Each PY neuron made local excitatory connections to five other PY neurons on both sides such that each PY neuron projected to 10 PYs with AMPA conductance strength of 9 nS and NMDA conductance of 0.9 nS. Each PY neuron also formed synaptic connections onto IN neurons with AMPA and NMDA conductance strengths of 3 nS and 0.3 nS respectively. Each IN neuron, in turn, projected to 5 local PY neurons, forming $GABA_A$ connections with conductance strengths of 9 nS. Additionally, each PY and IN neuron received individual afferent excitatory input modeled as a Poisson process. This network configuration, although simplified, reproduced realistic electrical activity found in cortical network during epileptic seizures and is similar to those used in previous studies (Bazhenov et al., 2002; Frohlich and Bazhenov, 2006; Frohlich et al., 2008b; Krishnan and Bazhenov, 2011).

Trauma to the network, in the form of cortical deafferentation, was modeled as a 50% reduction of the afferent input to a given set of PY neurons. The PYs that underwent deafferentation were selected at random and were within the 80 neurons in the center of the network. This provided a region of 40 PYs, 20 on both ends of the network, which would remain intact and allow for observation of seizure propagation and control for boundary effects. The fraction of deafferented PYs was varied from 0 to 100% within the aforementioned regions of 80

PY neurons, where 0% meant no PY was deafferented, and 100% meant that all 80 PYs underwent deafferentation.

The firing rate of the network was calculated every 5 s and was determined by averaging over all number of PY spikes in the 5 s interval. AMPA conductance between PYs was then adjusted, through homeostatic scaling, to maintain a target network firing rate of 5 Hz. We used a similar homeostatic rule as previous studies (Houweling et al., 2005; Frohlich et al., 2008a) and was given by the following:

$$W_{i+1}^{PY-PY} = W_i^{PY-PY} + \alpha_{HSP}(v_0 - \bar{v})W_i^{PY-PY}$$

where W_i^{PY-PY} is the AMPA conductance between two excitatory neurons at the i^{th} 5 s interval, v_0 is the target firing rate (5 Hz), $\bar{v}$ is the current network averaged firing rate, and α_{HSP} is the rate of homeostatic scaling (α_{HSP} = 0.01, unless otherwise specified). Because it was not possible to simulate the network model on the longer time scale of the HSP, we applied HSP at a much faster rate (minutes) than observed *in vivo* (hours to days). We determined the value of α_{HSP} by controlling the network activity and ion concentrations, ensuring that they always stayed in the physiological range without requiring excessively long computational times.

Seizures in humans and animal models of TBI generally last for only a brief period (30 sec to a few minutes). Homeostatic changes in network excitability in cell cultures, *in vitro* and *in vivo* conditions require several hours (> 4 hrs) to days of chronically blocked activity (Topolnik et al., 2003b, a; Nita et al., 2006; Echegoyen et al., 2007; Nita et al., 2007; Rich and Wenner, 2007; Trasande and Ramirez, 2007; Avramescu and Timofeev, 2008; Ibata et al., 2008; O'Leary et al., 2010). Therefore, we assumed that the timescales for HSP and seizure activity are very different, and that HSP may not have much of an effect on synaptic weights during a single seizure event. As such, to prevent unrealistic changes of synaptic weights during seizures in the

model, where the rate of HSP was increased to obtain reasonable simulation times, we turned HSP off during seizure-like events.

In addition to the homeostatic scaling, we added synaptic recovery processes to some of the simulations to model trauma-induced axonal sprouting (Kusmierczak et al., 2015) and to allow the deafferented PY neurons to recover the lost afferent inputs. This was implemented by:

$$A_{i+1}^{PY} = A_i^{PY} + \gamma_{Syn}(A_0 - A_i^{PY})A_i^{PY}$$

where A_i^{PY} is the strength of the current afferent input to the deafferented PY neurons, A_0 is the original strength of the afferent input, and γ_{Syn} is the sprouting rate. The sprouting rate was varied in our simulations to test the hypothesis that the differences in axonal sprouting may be sufficient to explain observation that older cats are more susceptible to seizure than younger cats following partial cortical deafferentation (Timofeev et al., 2013). In our simulations, the homeostatic rule was applied globally, and axonal sprouting process was applied to all deafferented PY neurons only.

Estimation of seizure thresholds. The seizure threshold was determined using a binary search method using an iterative procedure. The network was initially stimulated with high, P_{Up}, and low, P_{Low}, amplitude current pulses that would not induce a seizure, P_{Low1}, and would always induce seizure, P_{Up1}, respectively. At each step in the iterative process, the current pulse value was set to the average of the upper and lower bounds, $<P>$. If this new value $<P>$ elicited a seizure, then the upper bound would be set to $P_{Up2} = <P>$. If the pulse value of $<P>$ was unable to elicit a seizure, the lower bound would be set to $P_{Low2} = <P>$. The next current pulse value would be determined by once again taking the average of the upper and lower bounds. This process was repeated until the difference between the upper and lower bounds was less than $e = 0.1$, at which point the threshold was taken to be the average of these final bounds.

Acknowledgements

Chapter 2, in full, is a reprint of the material as it appears in Modeling of Age-Dependent Epileptogenesis by Differential Homeostatic Synaptic Scaling 2015. González, Oscar C.; Krishnan, Giri P.; Chauvette, Sylvain; Timofeev, Igor; Sejnowski, Terrence; Bazhenov, Maxim. The dissertation author was the primary author of this paper.

Chapter 3: KCC2-Dependent Potassium Efflux in 4-Aminopyridine-Induced Seizure

Abstract:

A balance between excitation and inhibition is necessary to maintain stable brain network dynamics. Traditionally, seizure activity is believed to arise from the breakdown of this delicate balance in favor of excitation with loss of inhibition. Surprisingly, recent experimental evidence suggests that this conventional view may be limited, and that inhibition plays a prominent role in the development of epileptiform synchronization. Here, we explored the role of the KCC2 co-transporter in the onset of inhibitory network-induced seizures. Our experiments in acute mouse brain slices, of either sex, revealed that optogenetic stimulation of either parvalbumin- or somatostatin-expressing interneurons induced ictal discharges in rodent entorhinal cortex during 4-aminopyridine application. These data point to a proconvulsive role of $GABA_A$ receptor signaling that is independent of the inhibitory input location (i.e., dendritic *vs.* somatic). We developed a biophysically realistic network model implementing ion concentration dynamics to explore the mechanisms leading to inhibitory network-induced seizures. In agreement with experimental results, we found that stimulation of the inhibitory interneurons induced seizure-like activity in a network with reduced potassium A-current. Our model predicts that interneuron stimulation triggered an increase of interneuron firing, which was accompanied by an increase in the intracellular chloride concentration and a subsequent KCC2-dependent gradual accumulation

of the extracellular potassium promoting epileptiform ictal activity. When KCC2 activity was reduced, stimulation of the interneurons was no longer able to induce ictal events. Overall, our study provides evidence for a proconvulsive role of $GABA_A$ receptor signaling that depends on the involvement of the KCC2 co-transporter.

Introduction:

Under specific conditions, activation of inhibitory $GABA_A$ receptor signaling may play a prominent role in the generation of seizures (Lillis et al., 2012; Hamidi and Avoli, 2015; Sessolo et al., 2015; Uva et al., 2015; Yekhlef et al., 2015; Shiri et al., 2016). This evidence is in conflict with the established notion that epileptiform discharges result from excessive glutamatergic signaling due to reduced inhibition (Ben-Ari et al., 1979; Dingledine and Gjerstad, 1980; Schwartzkroin and Prince, 1980). Indeed, it has been shown that inhibitory interneurons discharge action potentials at the onset of seizure-like events both *in vitro* (Lillis et al., 2012; Uva et al., 2015; Levesque et al., 2016) and *in vivo* (Grasse et al., 2013; Toyoda et al., 2015). Moreover, seizure-like discharges *in vitro* disappear after pharmacological interventions that interfere with $GABA_A$ receptor signaling (Avoli et al., 1996; Lopantsev and Avoli, 1998; Uva et al., 2015). In line with this evidence, direct optogenetic activation of inhibitory interneurons during bath application of 4-aminopyridine (4AP) elicits seizure-like discharges *in vitro* (Yekhlef et al., 2015; Shiri et al., 2016). Together, these data suggest that an increase in inhibitory interneuron synchrony may lead to the development of paroxysmal seizure-like activity under conditions of impaired potassium (K^+) channel conductances. However, the mechanisms of this action remain to be fully understood.

Intracellular chloride concentration ($[Cl^-]_i$) increases in principal neurons at the onset of seizure-like activity in 4AP treated conditions (Lillis et al., 2012). Such intracellular

accumulation of $[Cl^-]_i$, which is presumably due to an increase in GABAergic signaling prior to seizure onset, can be accompanied by a large increase in the extracellular potassium concentration ($[K^+]_o$) (Krishnan and Bazhenov, 2011). *In vitro* optogenetic stimulation of inhibitory interneurons can increase $[K^+]_o$ to a level capable of inducing seizure-like discharges (Yekhlef et al., 2015). An elevated level of $[K^+]_o$ may function as a positive feedback loop, increasing overall network excitability and leading to seizure onset (Pedley et al., 1974; Traynelis and Dingledine, 1988; Somjen, 2002; Frohlich and Bazhenov, 2006; Frohlich et al., 2008b; Krishnan and Bazhenov, 2011; González et al., 2015). Indeed, fast-rising $[K^+]_o$ increases associated with interneuron network activity preceded the initiation of seizure-like events *in vitro* in the 4AP seizure model (Librizzi et al., 2017). Previous computational studies found that oscillations of $[K^+]_o$ mediate periodic transitions between fast runs and spike-and-wave complexes during seizures (Frohlich and Bazhenov, 2006; Frohlich et al., 2008b; Krishnan and Bazhenov, 2011), and that increases in baseline $[K^+]_o$ fluctuations may occur following cortical trauma (González et al., 2015). K^+ dynamics have been implicated in the transition to seizure and spreading depression (Wei et al., 2014a), two network states previously thought to be mechanistically distinct.

The potassium-chloride co-transporter isoform 2 (KCC2) has been proposed as the critical link between the increase in $[Cl^-]_i$ and subsequent increase in $[K^+]_o$ (Rivera et al., 2005; Hamidi and Avoli, 2015; Shiri et al., 2016). Indeed, reduction of KCC2 activity prevents the generation of seizure-like events induced by 4AP (Hamidi and Avoli, 2015), as well as the increases in $[K^+]_o$ that occur in response to high-frequency stimulation (Viitanen et al., 2010). Therefore, it was postulated that synchronized GABAergic activity may cause a gradual accumulation of $[Cl^-]_i$, leading to the activation of KCC2. This results in the extrusion of both

Cl^- and K^+, allowing K^+ to reach a level necessary to elicit seizure (Avoli and de Curtis, 2011; Avoli et al., 2016).

In our new study, we tested this hypothesis by employing a biophysically realistic network model with dynamic ion concentrations, Na^+/K^+ ATPase activity, and KCC2 co-transporter activity. We found that reduction of the outward K^+ (type A) current (I_A), mimicking the effects of 4AP application, changed the network dynamics so interneuron stimulation could initiate seizure-like activity. Importantly, reduction of KCC2 activity (*cf*.,(Hamidi and Avoli, 2015) prevented seizure generation, thus supporting our hypothesis about the role of KCC2 in ictogenesis.

Results:

Optogenetic stimulation of interneurons triggers ictal discharges

Spontaneous 4AP-induced ictal discharges were recorded from the entorhinal cortex (EC) of PV-Cre mice that were transcranially injected with the enhanced ChR2 opsin, ChETA (n = 5 slices). These discharges occurred every 158.07 ± 10.30 s with an average duration of 45.97 ± 1.33 s (n = 124 events). Using a 30 s train of 1 s light pulses at 0.2 Hz that optogenetically activated fast-spiking parvalbumin (PV)-positive interneurons, we were able to trigger ictal discharges of similar duration (i.e., 43.91 ± 2.27 s) but more frequently, at an average interval of 139.45 ± 4.79 s (n = 35 events; $p < 0.05$; figure 3.1A).

Next, we established whether the ability of interneuron activation to drive ictal discharges was linked exclusively to fast-spiking PV-positive interneurons, or whether ictal discharges could also be triggered by activating regular-spiking somatostatin (SOM)-positive interneurons. Therefore, we obtained brain slices containing the EC of SOM-Cre mice that had been transcranially injected with the ChETA opsin (n = 8 slices). Spontaneous 4AP-induced ictal

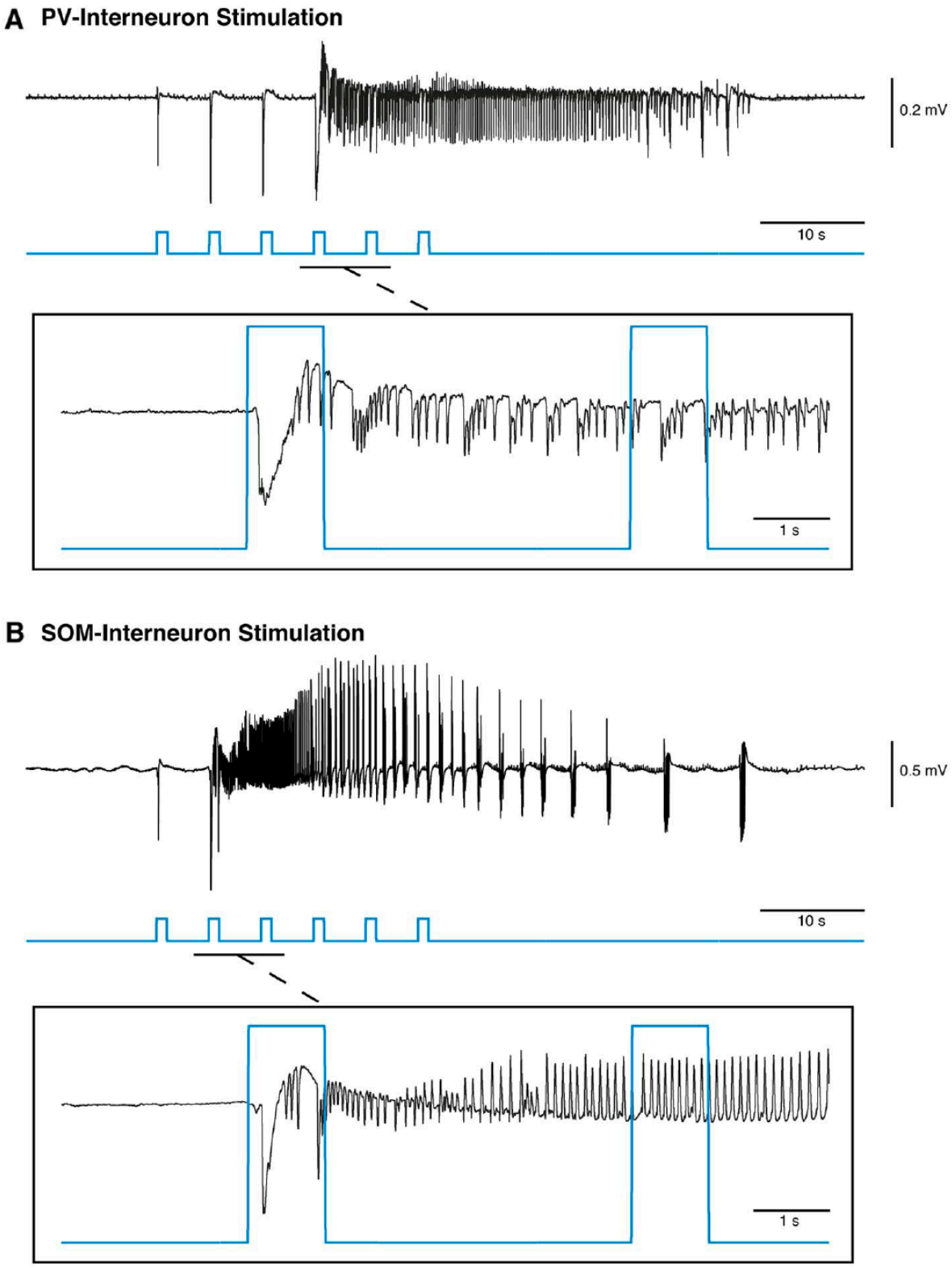

Figure 3.1 Ictal discharges can be triggered by optogenetic stimulation of PV- or SOM-positive interneurons. **A**, Ictal discharge evoked by 0.2 Hz series of 1 s light pulses stimulating PV-positive interneurons during bath application of 4AP; ictal onset is expanded to show the timing of the light pulse in relation to ictal onset (box). **B**, The same stimulation parameters applied to SOM-positive interneurons also triggers ictal discharges.

discharges in these experiments occurred every 127.35 ± 6.30 s and lasted on average 63.28 ± 1.84 s (n = 126 events). Using the same protocol used to stimulate PV-interneurons (i.e. 1 s light pulses at 0.2 Hz for 30 s), we were able to trigger ictal discharge of similar duration (55.71 ± 1.90 s), but at a shorter interval of 104.56 ± 5.47 s (n = 44 events; $p < 0.05$; figure 3.1B). The ictal discharges elicited by the optogenetic activation of either PV- or SOM-expressing interneurons showed characteristic properties of low-voltage, fast (LVF) ictal discharges. Previously, we showed that these LVF ictal discharges are different from the hypersynchronous (HYP) ictal discharges induced by optogenetic stimulation of CamKII-positive principal neurons suggesting a different mechanism between principal neuron- and inhibitory interneuron-induced ictal discharges (Shiri et al., 2016).

Reduction of I_A primes the network for interneuron-induced seizure-like activity

In order to establish the mechanisms by which PV- and SOM-interneuron stimulation causes ictal discharges in brain slices treated with 4AP, we developed a biophysically realistic network model implementing dynamic ion concentrations, the electrogenic Na^+/K^+ pump, and the KCC2 co-transporter. The network contained synaptically coupled principal (excitatory) neurons (PN) and inhibitory interneurons (IN), where the extracellular compartments of these two neuron types were ionically coupled (see Methods). In order to make comparisons between our model and experimental data, we modeled the application of 4AP as resulting in a 50 percent reduction of the outward K^+ A-current. Additionally, optogenetic stimulation of interneurons was modeled as a series of 1 s pulses at 0.2 Hz for 30 s similar to those used in our *in vitro* experiments; these "activating" pulses were applied to all interneurons.

In a control network, one without reduction of I_A, the stimuli applied to INs resulted in increased IN firing rate for the duration of the stimulation, followed by a gradual decay back to

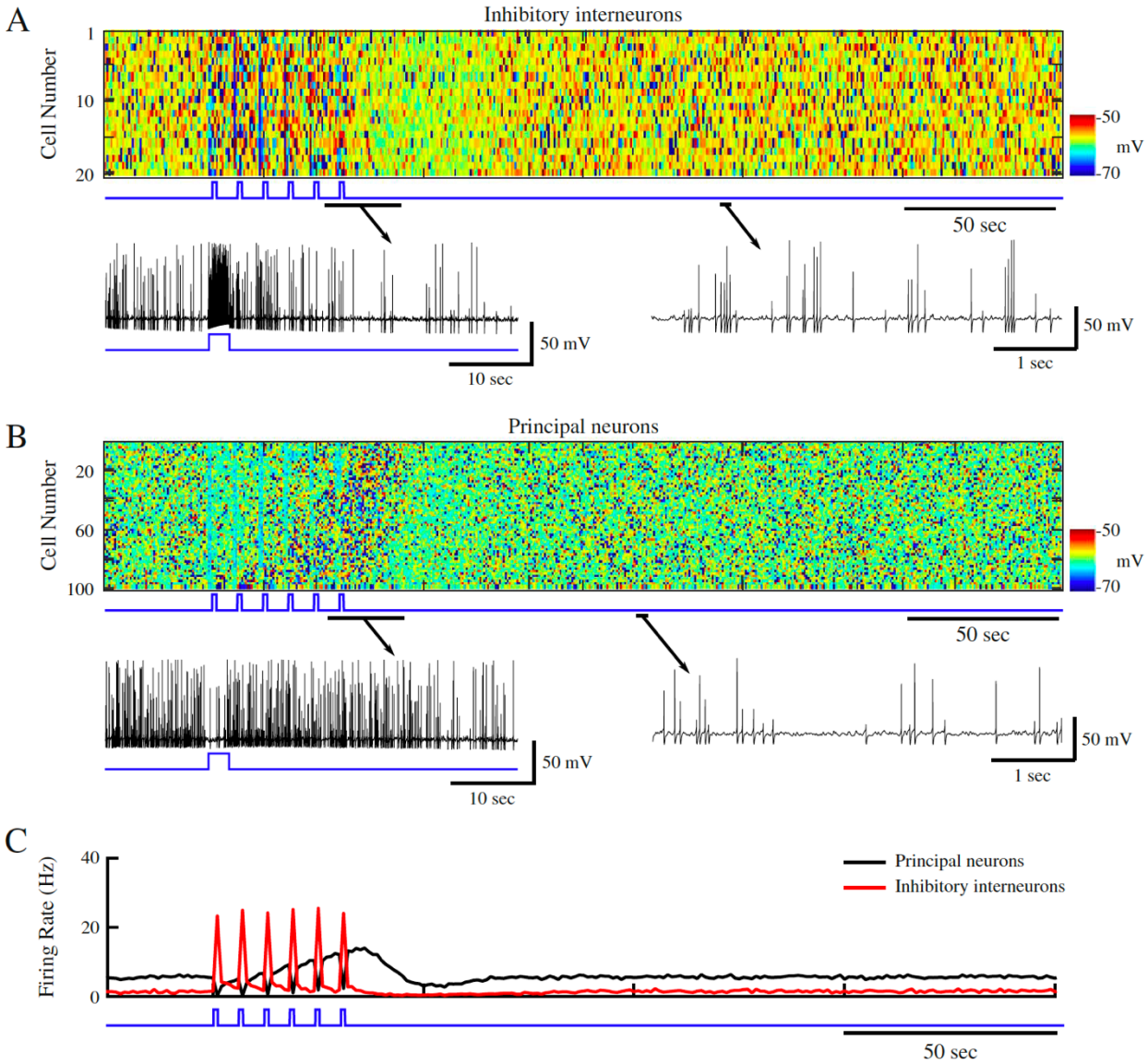

Figure 3.2 Stimulation of inhibitory interneurons in a healthy network results in brief silencing of excitatory neurons. A, Top panel shows raster plot of interneuron activity. Bottom panel shows zoom in of a single representative interneuron spiking from the network in the top panel. Time of interneuron stimulation is indicated by the blue trace. **B,** Principal neuron network activity with zoom in the spiking pattern of a single principal neuron. The blue trace indicates the time of interneuron stimulation. **C,** Mean firing rates for the interneurons (red) and principal neurons (black).

baseline firing (figure 3.2A). During baseline activity, the mean IN firing rate fluctuated around 1 Hz, but during stimulation it reached ~25 Hz (figure 3.2C, red). The increase in IN firing during stimulus pulses was accompanied by a hyperpolarization and relative silencing of the postsynaptic PNs (figure 3.2B and C, black trace). Similar to INs, PNs displayed a gradual return

to a baseline mean firing rate of about 5 Hz (figure 3.2C, black trace). This control network behaved as expected, i.e., the transient increase in IN firing caused a transient hyperpolarization of the PNs followed by a gradual return to the baseline activity.

We next tested the effects induced by IN stimulation on the network dynamics during conditions mimicking 4AP application, i.e., a reduction of I_A in both PNs and INs that resulted in a slight increase of the mean intrinsic baseline firing rates of both cell types (~ 4 Hz and ~ 12 Hz for INs and PNs respectively; figure 3.3D). In this condition, a single stimulus applied to INs produced an expected hyperpolarization and silencing of PN activity. We then proceeded to apply a sequence of the stimuli to all INs to model the effect of optogenetic stimulation similar to our experiment in the control network (figure 3.2). IN firing peaked at ~ 35 Hz during each stimulus pulse (figure 3.3A and D, red trace), and during the first 2 pulses PNs were hyperpolarized and silenced by the IN-mediated inhibition (figure 3.3B and C). However, during subsequent stimulation pulses, the mean firing rate of PNs began to increase (figure 3.3D, black trace), and the network developed a seizure-like state, which initiated as focal tonic firing (figure 3.3B, cells 60-100) before spreading to the rest of the network, and eventually transitioning to a clonic bursting phase (figure 3.3B and C). Seizure termination was followed by the postictal depression, and then by a return to baseline firing in both neuron types.

Since reduction of I_A shifted the network to a state where synchronous inhibitory activity could induce seizure, we next tested the effect of I_A strength on the seizure threshold. Reduction of I_A made networks more susceptible to seizure (figure 3.3E; 40-60% range), which can be attributed to increased intrinsic network excitability due to reduced K^+-dependent inhibition. I_A strengths less than 40% of the baseline resulted in spontaneous seizures, while strengths greater than 60% did not allow transitions to seizure-like activity following interneuron stimulation.

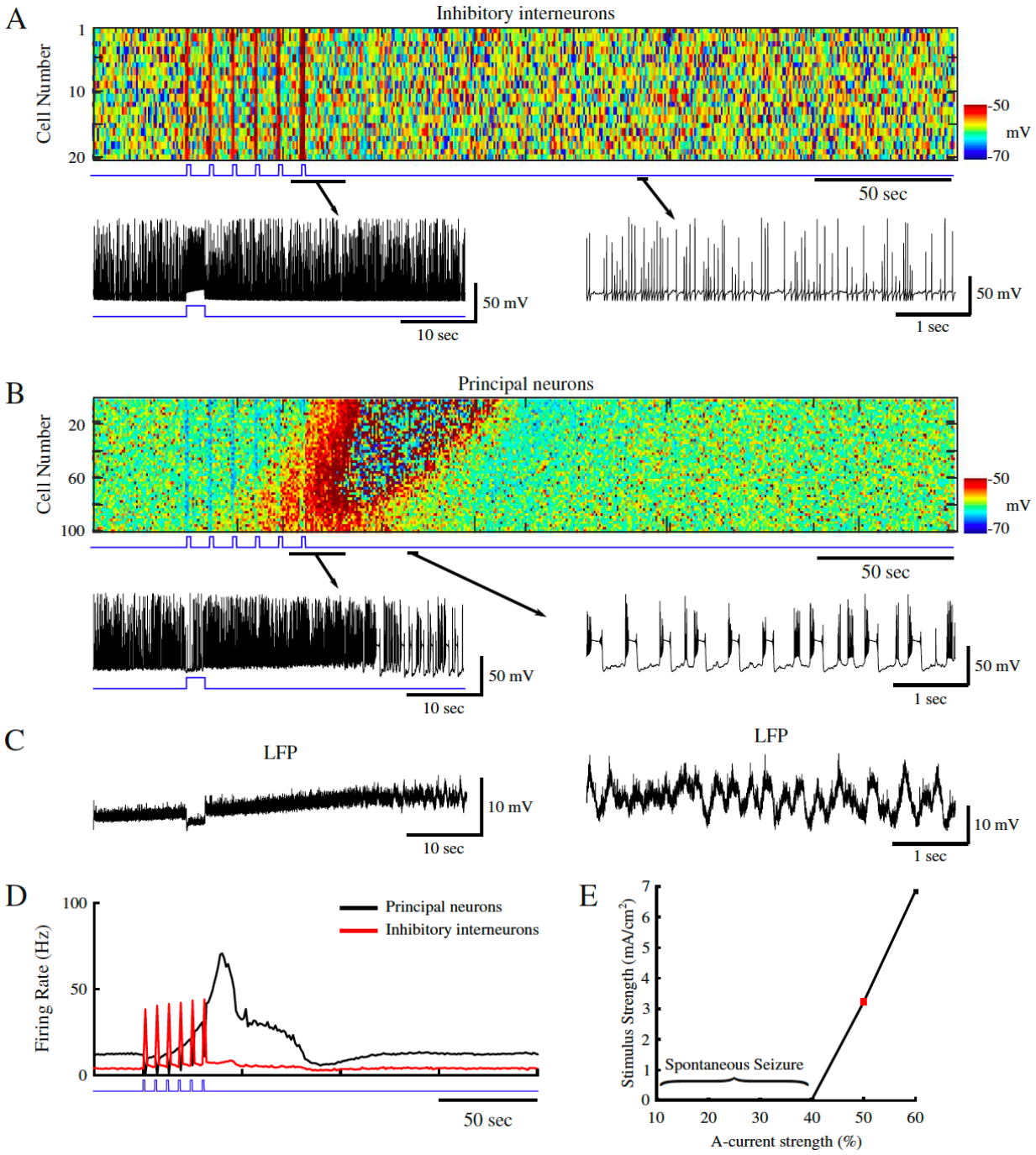

Figure 3.3 Reduction of A-current increases network excitability allowing for ictogenesis upon interneuron stimulation. A, Top panel shows raster plot of interneuron activity. Bottom panel shows zoom in of a single interneuron spiking from the network in the top panel. Time of interneuron stimulation is indicated by the blue trace. **B,** Principal neuron network activity with zoom in the spiking pattern of a single principal neuron. The blue trace indicates the time of interneuron stimulation. **C,** Corresponding local field potentials (LFP) for the zoom-ins in B. **D,** Mean firing rates for the interneurons (red) and principal neurons (black). **E,** Stimulus strength necessary for seizure generation as a function of A-current strength. Red square indicates the A-current strength used for the network presented in panels A-D.

Dynamics of the $[K^+]_o$ and $[Cl^-]_i$ under these two network conditions – i.e., control and under reduced I_A (figures 3.2 and 3.3) – revealed stark differences following IN stimulation. As seen in figure 3.4A, mean $[Cl^-]_i$ and $[K^+]_o$ for all PNs behaved similarly prior to and during IN stimulation in both control and reduced I_A networks (red and black traces respectively). During IN stimulation, both networks revealed increases in the mean $[Cl^-]_i$, and initial decreases in $[K^+]_o$ (figure 3.4A). The increase in $[Cl^-]_i$ in PNs was presumably due to activation of postsynaptic $GABA_A$ receptors, while the transient (initial) decrease in $[K^+]_o$ could reflect the resulting reduction of PN firing. Following termination of the IN stimulation, the $[Cl^-]_i$ in the control network gradually returned to baseline along with the IN firing rate (figure 3.2C, red trace and figure 3.4A, red trace in left panel). PN firing became transiently elevated but then also returned to baseline (figure 3.2C, black trace). In contrast, under conditions of I_A reduction, IN firing remained elevated and $[Cl^-]_i$ continued to increase following the end of the stimulation (figure 3.2C, red trace and figure 3.4A, black trace in left panel). Accumulation of $[Cl]_i$ caused activation of the KCC2 co-transporter. As KCC2 uses K^+ gradient to remove Cl^- (Payne et al., 2003), activation of KCC2 led to accumulation of $[K^+]_o$ (figure 3.4A, right panel, black trace). This increased PNs excitability (already elevated under reduced I_A conditions) and triggered a positive feedback loop (Frohlich and Bazhenov, 2006; Frohlich et al., 2008b; Krishnan and Bazhenov, 2011) initiating a network transition to seizure-like activity (figure 3.4B and 3.4C). It is important to emphasize, that while the increase of $[Cl^-]_i$ reduced the effect of inhibition, the Cl^- reversal potential never raised above the resting membrane potential of PNs and, therefore, the effect of $GABA_A$ remained hyperpolarizing throughout the entire simulation time.

Both $[Cl^-]_i$ in PNs and $[K^+]_o$ in the surrounding extracellular space remained elevated during the seizure-like activity (figure 3.4B and C, respectively). The expanded sample shown in

figure 3.4D illustrates how activation of INs resulted in the silencing and hyperpolarization of PNs during stimulation pulses, while the subsequent accumulation of $[K^+]_o$ increased firing rate and eventually triggered the transition to seizure-like activity. These results reveal that in conditions of increased baseline excitability (such as after reducing I_A), the network is able to generate seizure-like activity following interneuron activation. Our model suggests that the mechanism of seizure initiation involves: (a) IN stimulation leading to the release of GABA and postsynaptic activation of $GABA_A$ receptors; (b) $GABA_A$ receptor activation leading to increase of $[Cl^-]_i$ mediating KCC2 activation; (c) KCC2 activation leading to increase of $[K^+]_o$ sufficiently to initiate the positive feedback loop that mediates an "avalanche" increase of excitability.

KCC2 co-transporter activity gives rise to interneuron-induced seizure-like activity

To directly test our hypothesis that an increase of KCC2 activity, resulting from $[Cl^-]_i$ accumulation, may underlie initiation of seizure-like activity, we reduced KCC2 co-transporter strength by 50 percent ($\alpha_{KCC2} = 40$, see Methods) in a network with reduced I_A, while stimulating INs (figure 3.5). IN stimulation was identical to that performed in the previous experiments (figures 3.2 and 3.3). In this new condition, stimulation of INs resulted only in the transient silencing of PN activity (figure 3.5A, top), and $[K^+]_o$ returned to the baseline levels shortly after the termination of IN stimulation (figure 3.5A, bottom). Unlike the results shown in figure 3.3, no transition to seizure-like activity occurred during or following the termination of IN stimulation. Note, however, that the reduction of KCC2 activity resulted in a less excitable network, which was caused by a decrease of $[K^+]_o$ accumulation due to the reduced KCC2 baseline activity.

To further demonstrate that accumulation of $[Cl^-]_i$ was directly responsible for the activation of the KCC2 co-transporter and subsequent accumulation of $[K^+]_o$, in the next

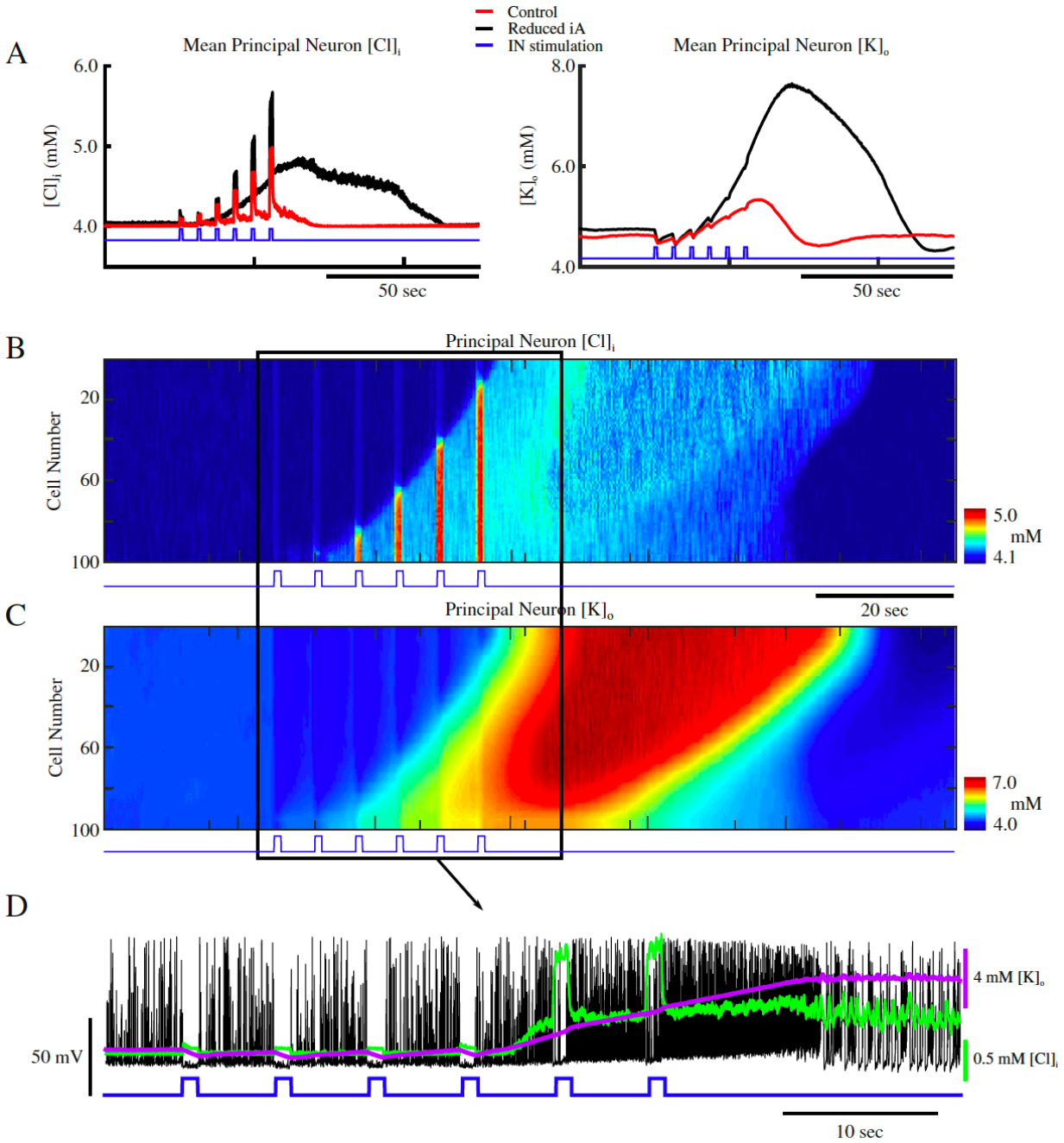

Figure 3.4 Increase of $[Cl^-]_i$ leads to gradual accumulation of $[K^+]_o$ and ictogenesis. A, Mean $[Cl^-]_i$ (left) and $[K^+]_o$ (right) for principal neurons in the control network from figure 2, and the reduced A-current network in figure 3 (red and black respectively). The blue trace indicates the pattern of interneuron stimulation. **B and C,** network-wide $[Cl^-]_i$ and $[K^+]_o$ for principal neurons. The blue trace indicates the pattern of interneuron stimulation. **D,** Overlay of the spiking of a single principal neuron (black) from figure 3, and the corresponding $[Cl^-]_i$ (green), $[K^+]_o$ (purple), and IN stimulation (blue).

experiment we reduced the effect of KCC2 on the ion concentrations but prevented the reduction of baseline network activity (figure 3.5A). Thus, we kept the strength of KCC2 intact (α_{KCC2} = 80), but we capped the maximal amount of Cl^- that can enter both PNs and INs. In doing so, we limited the peak KCC2 activity without changing the baseline KCC2 activity and, therefore, baseline network firing rate. In this condition, IN stimulation was still unable to initiate a seizure-like response (figure 3.5B). $[Cl^-]_i$ increased during IN stimulation, however, it was unable to induce sufficient activation of the KCC2 co-transporter to trigger high $[K^+]_o$ increase. Thus, following IN stimulation, only a small and brief increase in $[K^+]_o$ was observed (figure 3.5B, bottom). This suggests that limiting KCC2 performance may prevent the transition to the seizure-like activity. We need to mention, however, that limiting peak $[Cl^-]_i$ level also affected other network properties (e.g., reversal potential of Cl^- and therefore effect of inhibition).

Since limiting $[Cl^-]_i$ increase could affect several properties of the model, in the next experiment we artificially limited the effect of $[Cl^-]_i$ on the KCC2 co-transporter only. Therefore, in this condition, though the $[Cl^-]_i$ could exhibit a significant increase, the KCC2 co-transporter would only sense a limited increase in $[Cl^-]_i$. That is, the value of the variable in the I_{KCC2} equation representing intracellular Cl^- concentration (see Methods) was kept below the actual amount of $[Cl^-]_i$. Essentially, this rendered the K^+ extrusion mechanism of the KCC2 co-transporter less sensitive to $[Cl^-]_i$. As shown in figure 3.5C, IN stimulation was unable to elicit seizure-like activity in this network. Brief increases in both $[Cl^-]_i$ and $[K^+]_o$ were observed following the stimulation (figure 3.5C, bottom). Though the KCC2 activity increased $[K^+]_o$ following IN stimulation, $[K^+]_o$ never reached concentrations sufficient for generation of seizure-like activity. Importantly $[Cl^-]_i$ could reach its peak level (the same as in the control model) in

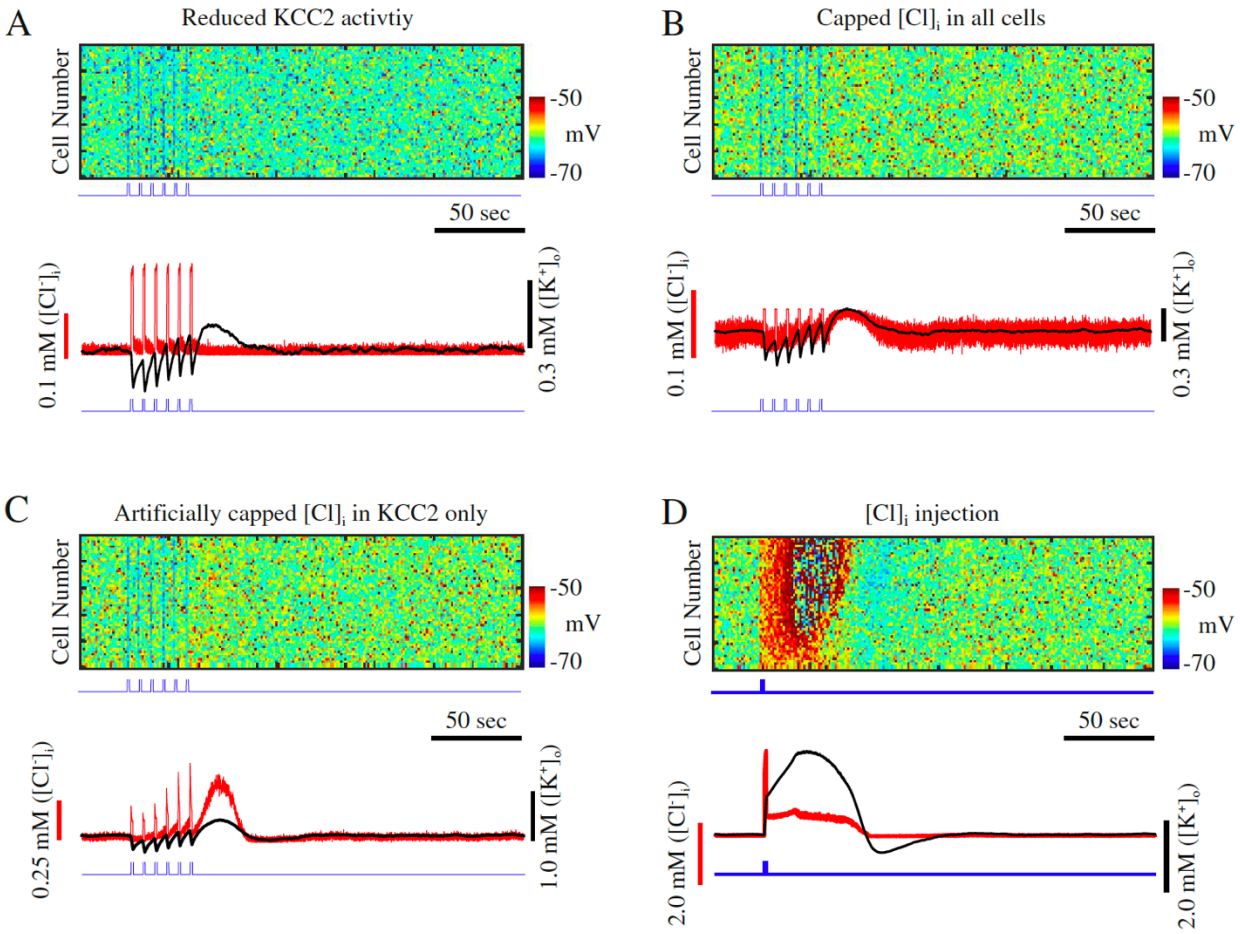

Figure 3.5 Seizure onset is dependent on KCC2 activation. A, Reduction of KCC2 activity prevents seizure. Top, raster plot of principal neurons in a network with reduced A-current and KCC2 activity. Blue trace indicates pattern of interneurons stimulation. Bottom, corresponding mean $[Cl^-]_i$ (red) and mean $[K^+]_o$ (black) for principal neurons in top panel. **B,** Network with limited $[Cl^-]_i$ accumulation. Top, raster plot showing activity of principal neurons. Bottom, corresponding mean $[Cl^-]_i$ (red) and mean $[K^+]_o$ (black) for principal neurons from the top panel. **C,** Network with artificially impaired $[Cl^-]_i$ sensitive K^+ mechanism. Top, raster plot showing activity of principal neurons. Bottom, corresponding mean $[Cl^-]_i$ (red) and mean $[K^+]_o$ (black) for principal neurons in top panel. **D,** Cl^- injection can trigger seizure. Top, rater showing activity of principal neurons. Blue trace shows time of Cl^- injection to principal neurons. Bottom, corresponding mean $[Cl^-]_i$ (red) and mean $[K^+]_o$ (black) for principal neurons in top panel.

this experiment, suggesting that the shift of the $GABA_A$ reversal potential, associated with increase of $[Cl^-]_i$, alone is not sufficient to induce seizure-like activity.

Finally, we tested whether a direct increase in $[Cl^-]_i$ in PNs could lead to the activation of the KCC2 co-transporter and subsequent elevation of $[K^+]_o$. In this experiment, we used a baseline model where the effect of $[Cl^-]_i$ on KCC2 was intact (similar to network in figure 3.3).

We found that a brief and sufficiently strong increase of $[Cl^-]_i$ in PNs was able to activate KCC2 extrusion of K^+ followed by the development of seizure-like activity (figure 3.5D). Together, these data suggest that Cl^- specific activation of KCC2 activity gives rise to the increase in $[K^+]_o$ sufficient for triggering transition to seizure-like activity.

$GABA_A$, and KCC2 influence properties of interneuron-induced seizure-like activity

Our model predicts that $GABA_A$ receptor-dependent increase in $[Cl^-]_i$ results in KCC2 mediated increase of $[K^+]_o$ and may lead to the initiation of seizure. Next, we tested how these two specific properties affect seizure onset and duration. By changing the contribution of $GABA_A$ to the $[Cl^-]_i$ in the model, we found that limiting $[Cl^-]_i$ increase in PNs increased the seizure threshold (figure 3.6A). Reducing $GABA_A$ receptor-dependent increase of $[Cl^-]_i$ to 94 % of the baseline, prevented IN stimulation from inducing seizure-like activity in the model. The reduced contribution of $GABA_A$ receptor activation to the $[Cl^-]_i$ also resulted in the shorter seizure duration (figure 3.6C). Both these effects arise from the fact that reduced $[Cl^-]_i$ accumulation led to the lower KCC2 activation and reduced K^+ efflux.

This prediction was further validated by directly changing KCC2 strength (α_{KCC2}). As illustrated in figure 3.6B, increasing KCC2 strength decreased seizure threshold, while decreasing KCC2 strength led to the threshold increase. Decreasing KCC2 strength also resulted in a decrease of seizure duration, while increased KCC2 strength had an opposite effect (figure 3.6D and F). Interestingly, reduction of KCC2 strength also delayed the onset time of seizure-like activity (figure 3.6E). Between the network with control (100 %) KCC2 activity and the network with low KCC2 activity (figure 3.6F, blue), there was a difference of about 11 s for the seizure onset time. In the networks with stronger KCC2 (figure 3.6E, green), seizure onset occurred earlier as compared to that in a control network with 100% KCC2 strength. This effect

Figure 3.6 Contributions to $[Cl^-]_i$ from $GABA_A$, and KCC2 activity modulate seizure threshold, duration and onset. A, Seizure threshold as a function of $GABA_A$ contribution to $[Cl^-]_i$. **B,** Seizure threshold as a function of KCC2 strength. **C,** Seizure duration as a function of $GABA_A$ contribution to $[Cl^-]_i$. **D,** Seizure duration as a function of KCC2 activity. **E,** Seizure onset delay as a function of KCC2 activity. Delay was measured between the onset time of a seizure in the control network with 100% KCC2 strength as compared to the seizure onset time in the networks with varied KCC2 strength. Inset shows examples of the filtered seizure LFPs. Colored data points correspond to the sampled data in the inset. Black trace in inset represents the control network with 100% KCC2 activity. Dash line shows threshold used to calculate seizure onset times. **F,** Examples of different seizure durations as a result of varied KCC2 strength. Top, filtered network LFP. Middle and Bottom, corresponding mean $[Cl^-]_i$ and $[K^+]_o$ respectively. Arrows point to the corresponding data points in **D**.

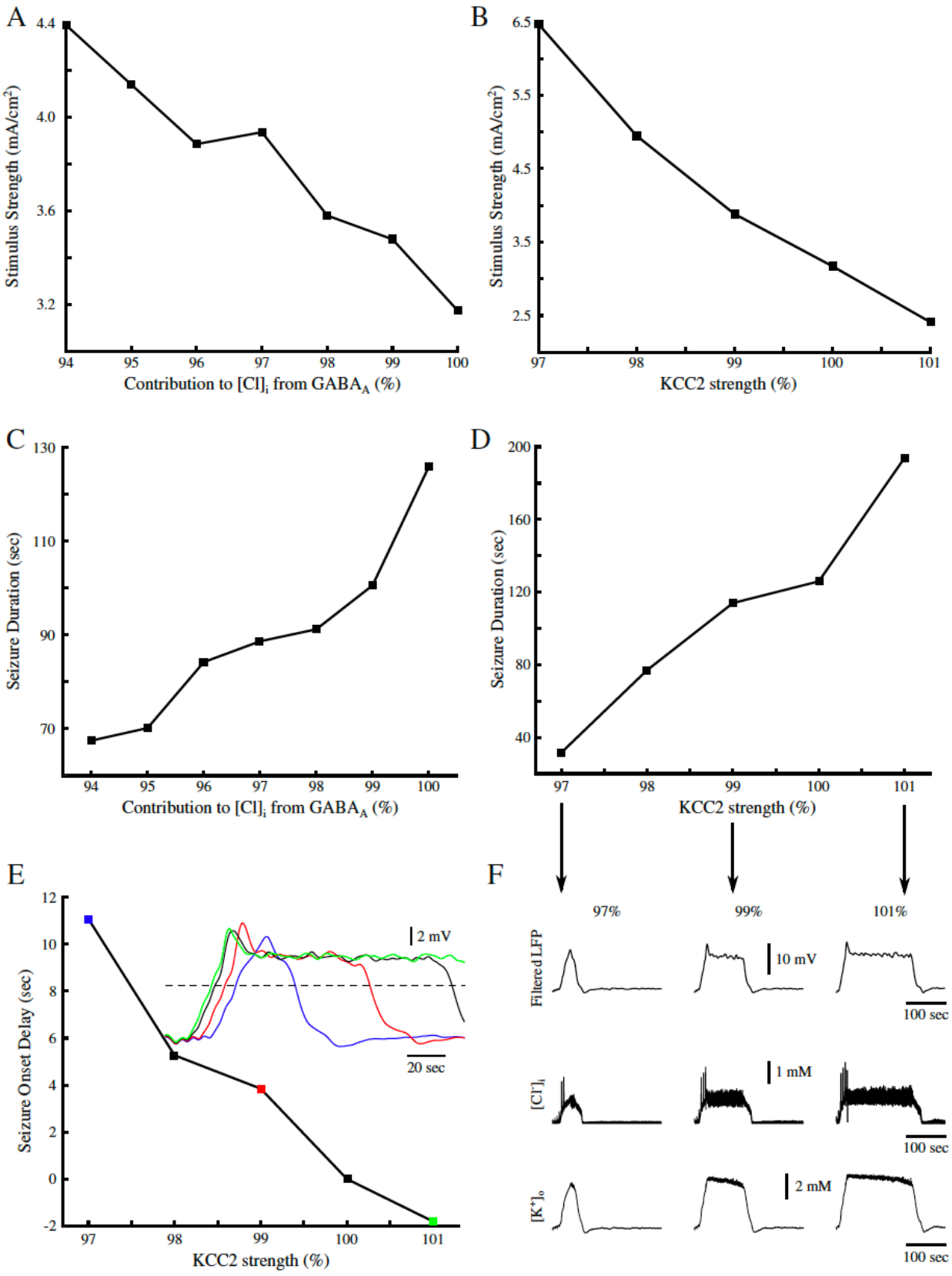
A
Stimulus Strength (mA/cm²)
4.4
4.0
3.6
3.2
94
95
96
97
98
99
100
Contribution to [Cl]i from GABAA (%)
B
Stimulus Strength (mA/cm²)
6.5
5.5
4.5
3.5
2.5
97
98
99
100
101
KCC2 strength (%)
C
Seizure Duration (sec)
130
110
90
70
94
95
96
97
98
99
100
Contribution to [Cl]i from GABAA (%)
D
Seizure Duration (sec)
200
160
120
80
40
97
98
99
100
101
KCC2 strength (%)
E
Seizure Onset Delay (sec)
12
10
8
6
4
2
0
-2
97
98
99
100
101
KCC2 strength (%)
2 mV
20 sec
F
97%
99%
101%
Filtered LFP
10 mV
100 sec
[Cl⁻]i
1 mM
100 sec
[K⁺]o
2 mM
100 sec

can be explained by the different rate of $[K^+]_o$ accumulation resulting from KCC2 activity. When KCC2 activity was enhanced, $[K^+]_o$ accumulated faster and reached the critical threshold that was sufficient for initiation of seizure-like activity after only a few seconds.

Discussion:

Application of potassium channel blocker 4AP may lead to epileptiform activity both *in vivo* and *in vitro* (Avoli and de Curtis, 2011). Optogenetic activation of inhibitory interneurons, in acute mouse brain slices exposed to 4AP, triggered seizure-like discharges (Sessolo et al., 2015; Yekhlef et al., 2015; Shiri et al., 2016). Blocking KCC2 activity with either VU024055 or high doses of bumetanide abolished ictal discharges in 4AP-treated rat brain slices (Hamidi and Avoli, 2015), suggesting that this form of inhibition-induced seizure may involve activation of the KCC2 co-transporter. In this new study, we tested the hypothesis that in conditions of elevated cortical excitability (as in the presence of 4AP), Cl^--dependent activation of the KCC2 co-transporter can trigger the progression of a network to a seizure state by an increase of extracellular K^+. Our *in vitro* data and computer simulation results predict that synchronous activation of the inhibitory interneurons can lead to a Cl^- increase sufficient for KCC2 activation and development of paroxysmal activity. This mechanism does not require synaptic $GABA_A$ to inverse polarity as the epileptiform activity is mediated by an increase of the extracellular K^+ and not by the depolarizing effect of the $GABA_A$ signaling, which remains inhibitory.

K^+ channelopathies in epilepsy

Various channelopathies, including mutated or misregulated K^+ channels, have been suggested to underlie certain forms of genetic epilepsies (D'Adamo et al., 2013; Lascano et al., 2016). Indeed, mutations in K_V4 α-subunits are present in some patients suffering from pharmacoresistant temporal lobe epilepsy (Singh et al., 2006; D'Adamo et al., 2013).

Specifically, a truncation mutation of the $K_V4.2$ α-subunit, responsible for the I_A, was observed in human patients (Singh et al., 2006). This mutation results in an attenuated I_A and subsequent increases in seizure susceptibility. In addition to mutations of specific ion channels, mutations of genes encoding proteins which modulate ion channel activity were found. Patients suffering from autosomal dominant partial epilepsy with auditory features (ADPEAF) have been shown to have point mutations in the leucine-rich glioma-inactivated 1 (LGI1) gene, resulting in reduced neuronal secretion of LGI1 (Ottman et al., 2004; Nobile et al., 2009; Dazzo et al., 2015). Neuronally secreted LGI1 binds to $K_V1.4$ and $K_V\beta1$, two known subunits comprising the A-type channels, preventing rapid inactivation of A-type currents (Schulte et al., 2006). The reduction of LGI1 expression in patients with ADPEAF results in the rapid inactivation of A-type channels and subsequent hyperexcitability.

The I_A antagonist, 4AP, has been shown to cause increased neuronal excitability and seizure-like discharges *in vivo* (Fragoso-Veloz et al., 1990; Levesque et al., 2013) and *in vitro* (Avoli et al., 1996; Lopantsev and Avoli, 1998). Interestingly, direct knockout of the $K_V4.2$ α-subunit resulted in increased excitability but did not generate spontaneous seizures. This knockout can, however, increase seizure susceptibility in response to additional proconvulsive pharmacological agents (Barnwell et al., 2009). Previous studies proposed that reduction of A-type K^+ current promotes ictogenesis by directly increasing neuronal excitability (Galvan et al., 1982; Gustafsson et al., 1982; Yamaguchi and Rogawski, 1992). In contrast, our study predicts that the reduction of A-type K^+ current leads to increased excitability of both excitatory and inhibitory neurons, and that the latter is critical for ictogenesis. We show that acute brain slices treated with 4AP exhibit transitions to seizure when perturbed by photostimulation of inhibitory interneurons. Using computer modeling, we tested the hypothesis that the mechanism by which

increased GABAergic signaling may lead to paroxysmal discharges involves Cl^--dependent activation of KCC2 followed by increases in the extracellular K^+.

$GABA_A$ receptor-dependent $[K^+]_o$ excitatory transients

Early studies proposed that reduced inhibition underlies seizure generation and perhaps epilepsy (Ben-Ari et al., 1979; Dingledine and Gjerstad, 1980; Schwartzkroin and Prince, 1980). Later, this view was challenged in several studies, (de Curtis and Avoli, 2016), which revealed that synchronous inhibitory interneuron activity occurs prior to seizure onset in slices treated with 4AP (Lillis et al., 2012; Uva et al., 2015; Levesque et al., 2016). It has been reported that intense GABAergic stimulation results in an increase of $[K^+]_o$ and long-lasting depolarizations (Rivera et al., 2005; Viitanen et al., 2010). Additionally, application of either bicuculline or furosemide inhibits these events (Viitanen et al., 2010). Indeed, these GABAergic excitatory $[K^+]_o$ transients have been shown to elicit prolonged depolarizations in rat CA1 and EC, and may play a prominent role in seizure generation (Lopantsev and Avoli, 1998; Viitanen et al., 2010). The proconvulsive GABAergic excitatory $[K^+]_o$ transients may give rise to the spontaneous seizure onset in patients with K^+ channel abnormalities.

In vitro and *in silico* results presented in this study predict the mechanisms by which GABAergic signaling can trigger seizure onset. We propose that the increased GABAergic signaling, such as triggered by stimulation of inhibitory interneurons, induces Cl^- build up, followed by Cl^--dependent activation of the KCC2 co-transporter and subsequent increase of $[K^+]_o$. Indeed, high frequency stimulation has been shown to cause increases in $[K^+]_o$ in response to intense $GABA_A$ receptor activation (Ruusuvuori et al., 2004; Rivera et al., 2005; Viitanen et al., 2010). Optogenetic stimulation of either SOM- or PV-expressing interneurons also causes large increases in $[K^+]_o$ (Yekhlef et al., 2015). It has been shown that sufficiently large initial

increase of $[K^+]_o$ can give rise to a positive feedback loop due to an increase in the network excitability through $[K^+]_o$-dependent depolarization of neurons, which in turn results in a further increase of $[K^+]_o$ and can lead to epileptiform activity (Somjen, 2002; Frohlich and Bazhenov, 2006; Frohlich et al., 2008b; Krishnan and Bazhenov, 2011; Wei et al., 2014a; González et al., 2015; Krishnan et al., 2015). Our new study predicts that the mechanisms leading to the initial increase in $[K^+]_o$, which kicks the network into a vicious feedback cycle, may involve KCC2-dependent efflux of K^+.

KCC2 in epilepsy

It has been shown that during early stages of development, GABAergic signaling in the rodent brain produces depolarizing potentials (Payne et al., 2003; Ben-Ari et al., 2007). The transition from depolarizing to hyperpolarizing GABAergic signaling has been attributed to the changes in Cl^- homeostasis as the animal develops (Payne et al., 2003; Watanabe and Fukuda, 2015). During early stages of development, the Na^+-K^+-Cl^- co-transporter (NKCC1) - responsible for transporting two Cl^- ions and one K^+ and Na^+ ion into the neuron - is highly expressed in rat and mouse neurons (Dzhala et al., 2005). As a result $[Cl^-]_i$ can reach baseline concentrations of 30mM (Achilles et al., 2007) resulting in depolarization of the Cl^- reversal potential and making GABAergic signaling depolarizing. As the brain develops, NKCC1 expression levels decrease, and KCC2 expression increases (Watanabe and Fukuda, 2015). Indeed, KCC2 mRNA is not detected until E18.5 and E15.5 in mouse CA1 and CA3 hippocampal subfields, respectively, while by P15, KCC2 and NKCC1 expression in the mouse brain reaches adult levels (Watanabe and Fukuda, 2015). In our current study, as well as in previous reports (Sessolo et al., 2015; Yekhlef et al., 2015; Shiri et al., 2016), epileptiform activity was induced through optogenetic stimulation of inhibitory interneurons in juvenile and young adult mice ranging from P15 to P40

during 4AP treatment. Furthermore, experiments in adult rats have shown that the KCC2 co-transporter plays a prominent role in the development of 4AP-induced epileptiform activity (Avoli et al., 1996; Lopantsev and Avoli, 1998; Hamidi and Avoli, 2015). Together, these results suggest that the "ictogenic" effect of interneuron activation in 4AP conditions, as described in our study, does not depend on the reversal of the $GABA_A$ synaptic potential as found early in development, but may rely on the mechanisms that were tested in our computational model. These mechanisms rest on the increase in the extracellular K^+ concentrations that result from KCC2 activation, triggered by an increase of intracellular Cl^- during intense interneuron firing.

Downregulation of KCC2 expression levels have been suggested to underlie the development of epilepsy in patients (Huberfeld et al., 2007; Buchin et al., 2016). However, other studies have shown that increased KCC2 activation may play a prominent role in seizure generation (Viitanen et al., 2010; Hamidi and Avoli, 2015). Activity dependent regulation of KCC2 expression may explain this seemingly conflicting evidence. Indeed, KCC2 expression has been shown to reduce following increases in activity and epileptiform discharges (Rivera et al., 2002; Rivera et al., 2004; Rivera et al., 2005). Our computational model revealed that the reduction of KCC2 activity prevents seizures in response to intense GABAergic signaling, suggesting that the observed reduction of KCC2 expression may not be a seizure triggering factor, but rather a protective mechanism to reduce the likelihood of seizures being triggered by other factors. Our study predicts that an increase of $[Cl^-]_i$ in excitatory neurons activates the KCC2 co-transporter and promotes seizure initiation. Consistent with this prediction, recent experimental studies reported large increases in $[Cl^-]_i$ in excitatory neurons prior to paroxysmal discharges (Lillis et al., 2012). Our model also predicts that increases in KCC2 activity can increase seizure susceptibility and duration. This result is consistent with previous computational

modelling and experimental work (Krishnan and Bazhenov, 2011; Hamidi and Avoli, 2015). Importantly, our model predicts a complex effect of $GABA_A$ inhibition in seizure development. On one hand, increase of $GABA_A$ signaling would act to suppress the network activity, on the other it would promote increase of $[Cl^-]_i$ in excitatory neurons which drives KCC2 activation and $[K^+]_o$ efflux, thus paradoxically increasing network excitability. The balance of these opposite factors determines the resulting network dynamics (normal vs epileptic) in the physiological settings.

Methods and Materials:

Animals. All procedures were performed according to protocols and guidelines of the Canadian Council on Animal Care and were approved by the McGill University Animal Care Committee. PV-Cre (Jackson Laboratory, B6;129P2-*Pvalb*$^{tm1(cre)Arbr}$/J, stock number 008069) and SOM-Cre (Jackson Laboratory, *Ssttm2.1(cre)Zjh*/J, stock number 013044) homozygote mouse colonies were bred and maintained in house in order to generate pups that were used in this study.

Stereotaxic virus injections. Four PV-Cre (2 male and 2 female) and five SOM-Cre (3 male and 2 female) pups were anesthetized at P15 using isoflurane and positioned in a stereotaxic frame (Stoelting). AAVdj-ChETA-eYFP virus (UNC Vector Core) was delivered in the entorhinal cortex (EC) (0.6 µL at a rate of 0.06 µL/min). Injection coordinates were: anteroposterior -4.00 mm from bregma, lateral +/- 3.60 mm, dorsoventral -4.00 mm. The transverse sinus was used as a point of reference, and the injection needle was inserted with a 2º anteroposterior angle. After completion of the surgery, pups were returned to their home cage.

Brain slice preparation. Mice were deeply anesthetized with inhaled isoflurane and decapitated at P30-40. Brains were quickly removed and immersed in ice-cold slicing solution

containing (in mM): 25.2 sucrose, 10 glucose, 26 $NaHCO_3$, 2.5 KCl, 1.25 KH_2PO_4, 4 $MgCl_2$, and 0.1 $CaCl_2$ (pH 7.3, oxygenated with 95% O_2/5% CO_2). Horizontal brain sections (thickness = 400 μm) containing the EC were cut using a vibratome (VT1000S, Leica) and incubated for one hour or more in a slice saver filled with artificial cerebrospinal fluid (ACSF) of the following composition (in mM): 125 NaCl, 25 glucose, 26 $NaHCO_3$, 2 KCl, 1.25 NaH_2PO_4, 2 $MgCl_2$, and 1.2 $CaCl_2$.

Electrophysiological recordings, photostimulation, and analysis. Slices were transferred to a submerged chamber where they were continuously perfused with oxygenated ACSF (KCl and $CaCl_2$ adjusted to 4.5 and 2 mM, respectively) (30 ºC, 10-15 mL/min). Field potentials were recorded using ACSF-filled microelectrodes (1-2 MΩ) positioned in the EC in the presence of 4AP (150 μM). Signals were recorded with a differential AC amplifier (AM systems), filtered online (0.1-500 Hz), digitized with a Digidata 1440a (Molecular Devices) and sampled at 5 kHz using the pClamp software (Molecular Devices).

For ChR2 excitation, blue light (473 nm, intensity 35 mW) was delivered through a custom-made LED system, where the LED (Luxeon) was coupled to a 3 mm wide fiber-optic (Edmund Optics) and was placed above the recording region. For optogenetic stimulation of interneurons, light pulses (1 s duration) were delivered at 0.2 Hz for 30 s with a 150 s interval between trains. All reagents were obtained from Sigma-Aldrich and were bath applied. Ictal duration and interval are expressed as mean ± SEM. Data were compared using the Student's t-test. Results were considered significant if the p-value was less than 0.05.

Principal neuron and interneuron models. Principal or excitatory neurons (PNs) and inhibitory interneurons (INs) were both modeled as two compartment models as described previously in (Bazhenov et al., 2002, 2004; Houweling et al., 2005; Frohlich et al., 2008b;

Krishnan and Bazhenov, 2011; Volman et al., 2011a; Volman et al., 2011b; González et al., 2015; Krishnan et al., 2015). The membrane potential dynamics for each compartment were modeled by the following equations:

$$C_m \frac{dV_D}{dt} = -g_D^c(V_D - V_S) - I_D^{leak} - I_D^{pump} - I_D^{Int}$$

$$g_S^c(V_D - V_S) = -I_S^{leak} - I_S^{pump} - I_S^{Int}$$

where $V_{D,S}$ are the dendritic and axosomatic membrane potentials, $g_{D,S}^c$ are the dendritic and axosomatic compartment coupling current conductance, I_D^{pump} and I_S^{pump} are the sum total Na^+/K^+ ATPase currents, I_D^{leak} and I_S^{leak} are the sum of the ionic leak currents, and I_D^{Int} and I_S^{Int} are the intrinsic currents for the dendritic and axosomatic compartments respectively. The intrinsic currents for the dendritic and axosomatic compartments have been previously described in (Krishnan and Bazhenov, 2011; González et al., 2015; Krishnan et al., 2015).

Dynamic ion concentrations. Ionic concentrations dynamics for $[K^+]_o$, $[K^+]_i$, $[Na^+]_o$, $[Na^+]_i$, $[Ca^{2+}]_i$, and $[Cl^-]_i$ were modeled similar to our previous work (Krishnan and Bazhenov, 2011; González et al., 2015; Krishnan et al., 2015). In order to model the KCC2 co-transporter, we made some modifications to the $[K^+]_o$ and $[Cl^-]_i$ equations. Briefly, our previous models included KCC2 regulation of $[Cl^-]_i$ in a $[K^+]_o$ dependent manner. However, the $[K^+]_o$ was not affected by KCC2 activity. In this new study the $[K^+]_o$ and $[Cl^-]_i$ were modeled as follows:

$$\frac{d[K^+]_o}{dt} = \left(\frac{k}{Fd}\right)\left(I_K^{pump} + I_{\sum K}^{Int} + I_{KCC2}\right) + \delta_o([K^+]_{oc} - [K^+]_o) + G$$

$$+ \delta_o\left(\left(\frac{([K^+]_{o-1} + [K^+]_{o+1})}{2} + \gamma([K^+]_{ox})\right)/(1+\gamma) - [K^+]_o\right)$$

$$\frac{d[Cl^-]_i}{dt} = -\left(\frac{k}{F}\right)\left(I_{\sum Cl}^{Int} + I_{KCC2}\right)$$

where F = 96489 C/mol is the Faraday constant, the ratio of the extracellular volume to surface area is given by d = 0.15, and the conversion factor k = 10. Additionally, I_K^{pump} is the K^+ current through the Na^+/K^+ ATPase, $[K^+]_{oc}$ is the K^+ concentration in the adjacent compartment, $[K^+]_{o-1}$ and $[K^+]_{o+1}$ are the concentrations of K^+ neighboring cells. $\gamma = 0.06$ is the ion coupling coefficient between PNs and INs, $[K^+]_{ox}$ is the K^+ concentration of the neighboring IN when computing the $[K^+]_o$ for PNs and vice versa. δ_o is the scaled diffusion coefficient ($\delta_o = D/\Delta x$), where $D = 6\text{x}10^{-6}\ cm^2/s$ is the diffusion constant, $\Delta x = 100\mu m$ is distance, and G represents the glial buffering of K^+ as described in detail previously (Krishnan and Bazhenov, 2011; González et al., 2015; Krishnan et al., 2015). $I_{\sum K}^{Int}$ and $I_{\sum Cl}^{Int}$ are the sum total intrinsic K^+ and Cl^- currents respectively. I_{KCC2} defines the efflux of $[K^+]_o$ and $[Cl^-]_i$ generated by the KCC2 co-transporter and is described as follows:

$$I_{KCC2} = \left(\frac{\alpha_{KCC2}}{1 + \exp\left(([Cl^-]_{i\infty} - [Cl^-]_i)/1.0\right)}\right)\left(\frac{[Cl^-]_{i\infty} - [Cl^-]_i}{\tau_{Cl}}\right)$$

$$\tau_{Cl} = \left(100 + \frac{\tau_{Cl\infty}}{\left(1 + \exp\left(\frac{[Cl^-]_{i\infty} - [K^+]_o}{\tau_{KoCl}}\right)\right)}\right)$$

where α_{KCC2} = 80 defines the strength of the co-transporter, $[Cl^-]_{i\infty}$ = 5mM is the steady-state Cl^- concentration, $[Cl^-]_i$ is the intracellular Cl^- concentration, $\tau_{Cl\infty}$ = 4x10^{3}s, and τ_{KoCl} = 0.08s.

Synapse and network properties. We modeled a one dimensional network consisting of 100 PNs and 20 INs. Every PN formed local excitatory synapses onto ten neighboring PNs with AMPA conductance strength of 3.5 nS and NMDA conductance of 0.9 nS. PNs also formed

excitatory synaptic connections onto INs with AMPA and NMDA conductance strengths of 2.4 nS and 0.24 nS respectively. INs synapsed onto five local PNs, with $GABA_A$ connections of 3.5 nS conductance strength. Additionally, PN and IN received individual afferent excitatory input modeled as a Poisson process as described in our previous studies (Krishnan and Bazhenov, 2011; González et al., 2015; Krishnan et al., 2015).

Estimation of seizure threshold. The seizure threshold was determined using a binary search method that employed an iterative procedure as described in (González et al., 2015). Briefly, at each step of the searching algorithm, the strength of the stimulus would be set to the mean of the upper and lower limits, $<P>$. If this stimulus strength was able to elicit seizure, the upper limit would be set to the current value of $<P>$. If $<P>$ was unable to elicit a seizure, the lower limit would take the value of $<P>$. The new stimulus strength, $<P>$, would then be computed based on the updated upper and lower limits. This process continued until the difference between the upper and lower limits was less than 0.1. The threshold was determined to be the average of these final limits.

Acknowledgements

Chapter 3, in full, is a reprint of the material as it appears in Role of KCC2-Dependent Potassium Efflux in 4-Aminopyridine-Induced Epileptiform Synchronization 2018. González, Oscar C.; Shiri, Zahra; Krishnan, Giri P.; Myers, Timothy L.; Williams, Sylvain; Avoli, Massimo; Bazhenov, Maxim. The dissertation author was the primary author of this paper.

Chapter 4: Ion Dynamics and the Origin of Infra-Slow Resting-State Fluctuations

Abstract:

Resting-state or baseline low frequency (0.01-0.2 Hz) brain activity is observed in fMRI, EEG and LFP recordings. These fluctuations were found to be correlated across brain regions

and are thought to reflect neuronal activity fluctuations between functionally connected areas of the brain. However, the origin of these infra-slow fluctuations remains unknown. Here, using a detailed computational model of a brain network, we show that spontaneous infra-slow (< 0.05 Hz) fluctuations could originate due to the ion concentration dynamics. Our computational model implemented dynamics for intra and extracellular K^+ and Na^+, intracellular Cl^- and Ca^{2+} ions, Na^+/K^+ exchange pump, and KCC2 co-transporter. In the network model simulating resting wake-like brain state, we observed infra-slow fluctuations in the extracellular K^+ concentration, Na^+/K^+ pump activation, firing rate of neurons and local field potentials. Holding K^+ concentration constant prevented the generation of these fluctuations. The amplitude and peak frequency of this activity were modulated by Na^+/K^+ pump, AMPA/GABA synaptic currents and glial properties. Furthermore, in a large-scale network with long-range connections based on CoCoMac connectivity data, the infra-slow fluctuations became synchronized amongst remote clusters similar to the resting-state networks observed *in vivo*. Overall, our study proposes that ion concentration dynamics mediated by neuronal and glial activity may contribute to the generation of infra-slow spontaneous fluctuations of brain activity that are reported as the resting-state fluctuations in fMRI and EEG recordings.

Introduction:

Resting-state or spontaneous background fluctuations, in the frequency range of 0.01-0.2 Hz (Fukunaga et al., 2006; Honey et al., 2007; Buckner et al., 2008; Ghosh et al., 2008; Greicius, 2008; Greicius et al., 2008; He et al., 2008; Khader et al., 2008; Broyd et al., 2009; Greicius et al., 2009; Larson-Prior et al., 2009; Lorincz et al., 2009; Chang and Glover, 2010; Picchioni et al., 2011; Palva and Palva, 2012; Pan et al., 2013; Hiltunen et al., 2014; Raichle, 2015), are reported by a wide range of neuroimaging methods, including electrophysiological, optical, EEG

and fMRI (Biswal et al., 1995; Fukunaga et al., 2006; Greicius, 2008; Greicius et al., 2008; Pan et al., 2013; Hiltunen et al., 2014). The spontaneous resting-state activity in fMRI signals is a robust phenomenon that has been widely used to evaluate brain network properties, from determining functional connectivity during cognitive tasks to identifying altered functional connectivity in various conscious and disease states (Vanhatalo et al., 2004; Fukunaga et al., 2006; Buckner et al., 2008; Greicius, 2008; Greicius et al., 2008; Broyd et al., 2009; Zhang and Raichle, 2010; Picchioni et al., 2011). The resting-state activity across wide brain regions forms functional networks, such as the default-mode network (DMN), that vary with brain state and type of cognitive activity (Vanhatalo et al., 2004; Fukunaga et al., 2006; Buckner et al., 2008; Greicius et al., 2008; Broyd et al., 2009; Picchioni et al., 2011). Several neurological and psychiatric disorders, such as epilepsy and schizophrenia, have been shown to correlate with altered resting-state fluctuations and functional connectivity (Vanhatalo et al., 2004; Buckner et al., 2008; Greicius, 2008; Lui et al., 2008; Broyd et al., 2009; Raichle, 2010; Zhang and Raichle, 2010; Gupta et al., 2017). Although there is growing interest in understanding the resting-state fluctuations, the underlying neural mechanisms by which these oscillations arise remain unknown.

Previous experimental work showed that infra-slow fluctuations in the local field potential (LFP) gamma power, neuronal firing rate, and slow cortical potentials (SCP) exhibit a correlational relationship with resting-state fMRI blood-oxygen-level dependent (BOLD) fluctuations (He et al., 2008; Khader et al., 2008; Picchioni et al., 2011; Palva and Palva, 2012; Pan et al., 2013; Hiltunen et al., 2014). Further, the underlying structural connectivity of brain networks was shown to shape the functional connectivity estimated from resting-state activity (Honey et al., 2007; Deco et al., 2009; Greicius et al., 2009; Deco et al., 2011). Finally,

computational studies, using population level models, suggested the role of intrinsic noise, coupling strengths, conduction velocities, and underlying structural connectivity in the generation of resting-state fluctuations (Honey et al., 2007; Ghosh et al., 2008; Deco et al., 2009). However, these earlier modeling studies were based on the phenomenological mean field type models and so the underlying biophysical properties giving rise to the infra-slow time scale based on activity of individual neurons and their networks remains to be understood. Interestingly, experimental and computational studies suggest that the resting-state activity arises from switching between different activity levels in the localized brain regions. Changes in the ion concentrations have been suggested to modulate network activity (Pedley et al., 1974; Chub and O'Donovan, 2001; Somjen, 2002; Bazhenov et al., 2004; Chub et al., 2006; Frohlich and Bazhenov, 2006; Frohlich et al., 2008b; Krishnan and Bazhenov, 2011; Wei et al., 2014a; Krishnan et al., 2015) that could occur at a slow time scale. In this study, we tested the hypothesis that fluctuations of the ion concentrations may result in the infra-slow resting-state brain activity fluctuations.

Extracellular potassium concentrations ($[K^+]_o$) have been shown to fluctuate during resting-state or background activity over a long time period (McCreery and Agnew, 1983). Recordings from anesthetized cat cortex have shown that the $[K^+]_o$ exhibits small amplitude (~ 0.5mM) fluctuations around a mean concentration, with the period of these fluctuations being about an hour or less (McCreery and Agnew, 1983). Additionally, extracellular potassium recordings in animal models of epilepsy have shown substantial $[K^+]_o$ fluctuations prior to and during bouts of seizure-like activity (Pedley et al., 1974; Traynelis and Dingledine, 1988; Somjen, 2002). A number of computational models suggested a prominent role of potassium concentration dynamics modulating neuronal excitability and synchrony (Bazhenov et al., 2004;

Frohlich and Bazhenov, 2006; Frohlich et al., 2008b; Krishnan and Bazhenov, 2011; Wei et al., 2014a; González et al., 2015; Krishnan et al., 2015). Previous studies have shown that slow spontaneous rhythmic activity in chick spinal cord may arise through accumulation and removal of intracellular chloride (Chub and O'Donovan, 2001; Chub et al., 2006). Similarly, changes in the ionic gradients have been reported to underlie slow bursting dynamics in epilepsy (Ziburkus et al., 2013; Huberfeld et al., 2015). We now know that slow neuronal dynamics can emerge without the presence of the slow time constants in the ion channel dynamics. The central idea of this new paper is that the ion gradients buildup and discharge, and ion pumping may result in the infra-slow time scale of the resting-state fluctuations.

Our study predicts that resting-state activity can arise from infra-slow fluctuations of the ion concentrations. Furthermore, we identified that the low amplitude fluctuations in the ion dynamics allow for local and long-range synchronization among the distant networks. These local fluctuations can lead to correlated and anti-correlated activities between clusters of neurons through long-range feedforward excitatory and inhibitory projections, which reflect underlying network structural connectivity in agreement to the experimental observations of the resting-state activity.

Results:

The biophysical network model developed in this study incorporated synaptically coupled excitatory pyramidal (PY) and inhibitory (IN) neurons, and implemented realistic dynamics of the major ion concentrations to provide *in vivo*-like conditions (Frohlich and Bazhenov, 2006; Frohlich et al., 2008b; Krishnan and Bazhenov, 2011; González et al., 2015; Krishnan et al., 2015). A “single cluster” network model possessed only local connectivity (5 neuron radius).

Below we will first explore dynamics of a single cluster network and then expand it to the case of several clusters connected with long-range synaptic connections.

Infra-slow fluctuations arise spontaneously in the network model

In a network consisting of a single cluster of 50 neurons (figure 4.1 A1), PY and IN population activity appeared random over a period of 800 sec simulation time (figure 4.1 A2 top). Individual voltage traces from PY neurons within the network showed spontaneous random firing (figure 4.1 A2 bottom). However, analysis of the mean firing rate of PY neurons revealed a very slow semi-periodic fluctuation (figure 4.1B). Similar fluctuations were observed in the band-pass filtered mean PY membrane voltage (figure 4.1C). The slow fluctuations in the mean firing rate and membrane voltage were also reflected in the slow fluctuations of the mean $[K^+]_o$ and $[Na^+]_i$ (figure 4.1D green and red respectively), and the mean Na^+/K^+ pump current (figure 4.1E). The $[K^+]_o$ fluctuation was 0.1-0.2 mM in amplitude, while the $[Na^+]_i$ fluctuation was only ~0.05 mM in amplitude. Power spectrum of the mean $[K^+]_o$, $[Na^+]_i$, Na^+/K^+ pump current, membrane voltage, and network firing rate revealed a peak amplitude at around 0.02 Hz (figure 4.1F).

Ion concentration dynamics give rise to the infra-slow fluctuations

Since we observed infra-slow resting-state fluctuations in both mean $[K^+]_o$ and $[Na^+]_i$, we first tested the role of these ions in the generation of the resting-state activity in our network model. Thus, we fixed the concentrations of these two ions independently. Holding the K^+ concentration constant resulted in a loss of the infra-slow oscillatory activity in the mean membrane voltage of the PY neurons, regardless of the specific values of the concentration (figure 4.2A top red). Power spectrum analysis revealed the disappearance of a low-frequency peak and almost flat spectrum (figure 4.2B inset). In contrast, preventing the Na^+ fluctuation did

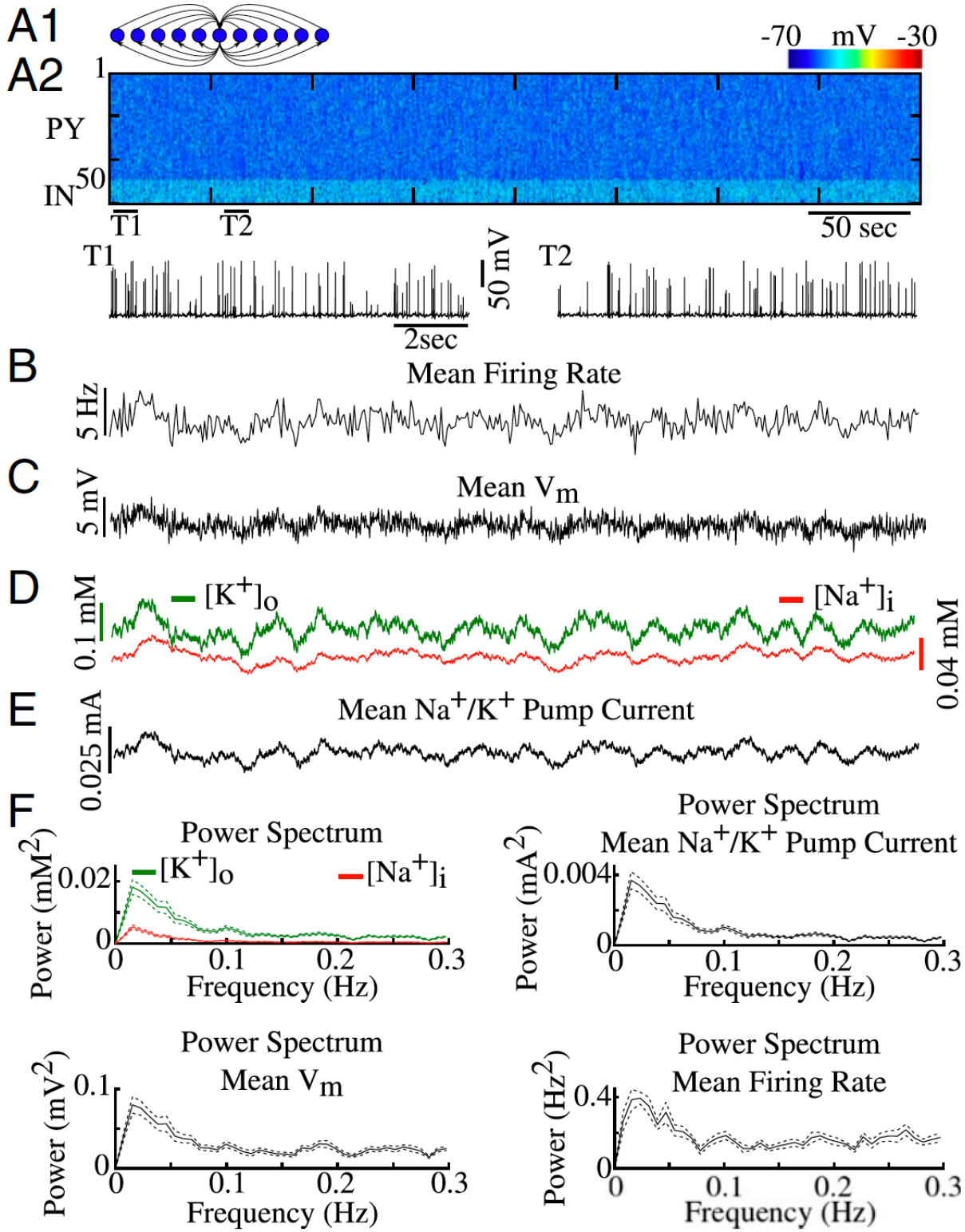

Figure 12.1 Minimal cortical network model exhibits resting-state fluctuations. A1, Cartoon of the basic network architecture. **A2,** Spontaneous activity in the network of PY and IN neurons. T1 and T2 indicate times expanded below in single PY cell traces. **B-E,** Mean PY firing rate, mean filtered (0.001-0.1Hz) membrane voltage, $[K^+]_o$ and $[Na^+]_i$, and Na^+/K^+ pump current dynamics, respectively. **F,** Power spectrums of the mean PY firing rate, membrane voltage, $[K^+]_o$ and $[Na^+]_i$, and Na^+/K^+ pump current.

not result in a loss of the infra-slow membrane voltage fluctuations (figure 4.2A and B, right). Unlike the condition with fixed K^+, the Power spectrum of the mean membrane voltage in the network with constant Na^+ still revealed a distinct peak around 0.02 Hz. This suggests that fluctuations of K^+ play a major role in the generation of the resting-state activity, while Na^+ fluctuation may play a modulatory role.

We next explored the role the Na^+/K^+ pump current, glia K^+ buffering, and AMPA/GABA synaptic connections in regulating properties of the resting-state fluctuations. Increasing the strength of the Na^+/K^+ pump resulted in decreased fluctuation amplitude of the pump current as revealed by the reduced peak in the Power spectrum (figure 4.2C, black). This decrease in the fluctuation amplitude was accompanied by increase in the peak frequency (figure 4.2C, red). For higher strength of the Na^+/K^+ pump, the relative changes of the extracellular K^+ were reduced, leading to the smaller resting-state fluctuations. Similarly, decreasing the half activation concentration of $[K^+]_o$ in glia cells, that increased effectiveness of glia buffering, reduced the resting-state fluctuation amplitude (figure 4.2D). Thus, the slow dynamic processes controlling the progressive accumulation of the ions and their removal determined the amplitude and peak frequency of the infra-slow fluctuations. Further, increasing the strength of the AMPA connections between PY neurons increased the amplitude of the resting-state fluctuations while shifting peak frequency to the lower values (figure 4.2E). GABA, on the other hand, had minimal impact on the amplitude of the resting-state fluctuations, but shifted the peak frequency to the higher values (figure 4.2E). Increase in the fluctuation amplitude due to increase in the AMPA connection strength suggests that recurrent synaptic excitation promoted faster and higher-level buildup of the extracellular K^+ concentration thus leading to stronger and faster resting-state fluctuations. It should be noted that diffusion of ions in the extracellular space was

Figure 4.2 Ion concentrations, Na^+/K^+ pump, glial K^+ buffering, and AMPA/GABA strength influence properties of the resting-state fluctuations. A, Mean membrane voltages (black) and mean filtered membrane voltages (red) for the networks with either fixed K^+ (left) or fixed Na^+ (right). **B left,** Power spectrum peak power as a function of fixed K^+ concentration. Percentage is based on the mean $[K^+]_o$ in control network. Inset shows individual Power spectrums for different fixed K^+ conditions. Black line shows a control. Green box indicates time used to compute peak power. **B right,** Corresponding Power spectrum of the mean membrane voltage in fixed Na^+ condition in A. **C,** Peak power (black) and peak frequency (red) as a function of Na^+/K^+ pump current strength. **D,** Power spectrum peak power as a function of glia model half activation K^+ concentration. **E,** Power spectrum peak power as a function of AMPA and GABA connection strengths (left). Power spectrum peak frequency as a function of AMPA and GABA connection strengths (right).

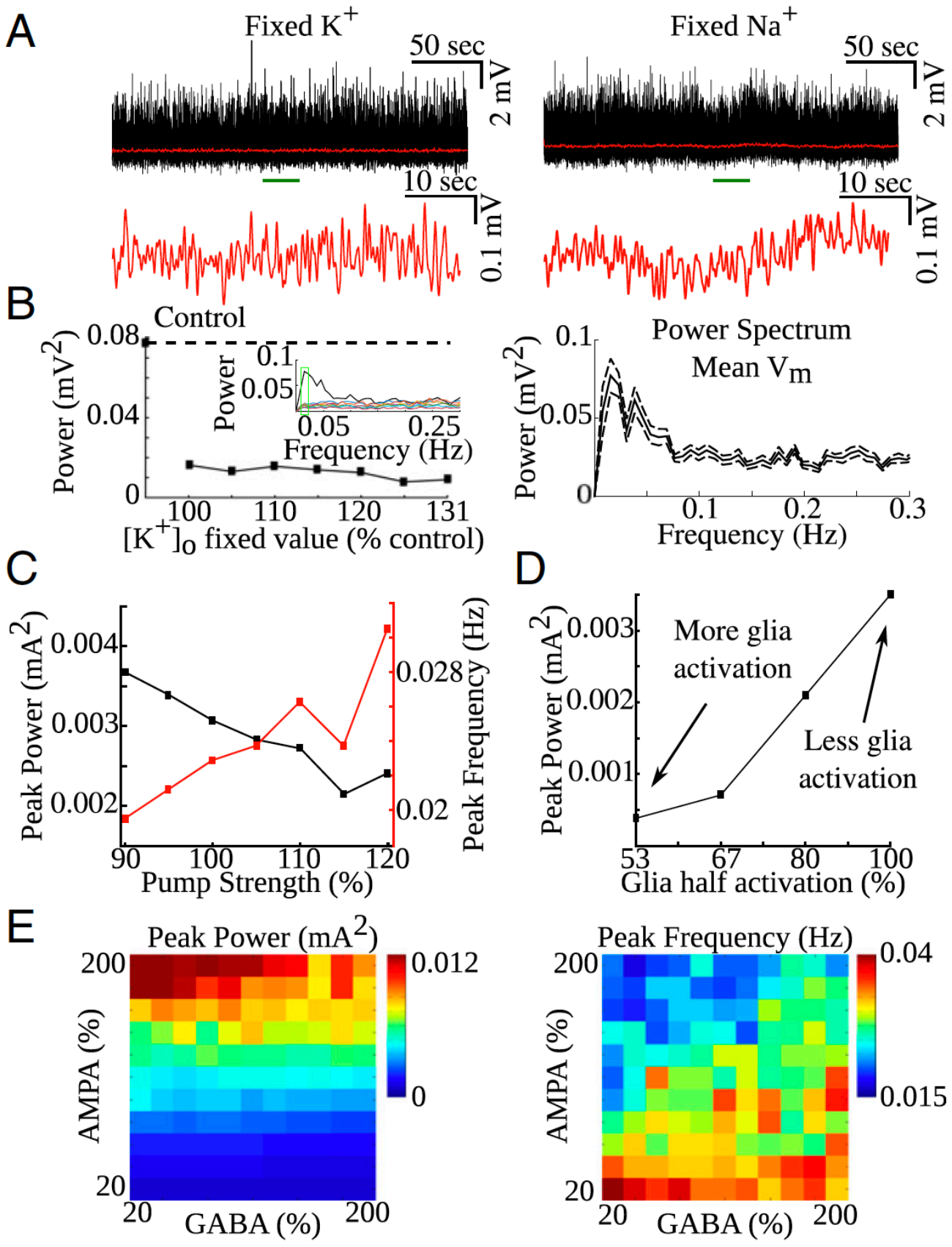
A
Fixed K+
50 sec
2 mV
10 sec
0.1 mV
Fixed Na+
50 sec
2 mV
10 sec
0.1 mV
B
Control
Power (mV2)
0.08
0.04
0
Power
0.1
0.05
0.05
0.25
Frequency (Hz)
100
110
120
131
[K+]o fixed value (% control)
Power Spectrum
Mean Vm
Power (mV2)
0.1
0.05
0
0.1
0.2
0.3
Frequency (Hz)
C
Peak Power (mA2)
0.004
0.003
0.002
0.028
0.02
Peak Frequency (Hz)
90
100
110
120
Pump Strength (%)
D
Peak Power (mA2)
0.003
0.002
0.001
More glia activation
Less glia activation
53
67
80
100
Glia half activation (%)
E
Peak Power (mA2)
200
20
AMPA (%)
20
200
GABA (%)
0.012
0
Peak Frequency (Hz)
200
20
AMPA (%)
20
200
GABA (%)
0.04
0.015

not required for the infra-slow activity, but removing diffusion reduced its amplitude (figure 4.3). Furthermore, the infra-slow fluctuations in the model could not be explained by the simulation protocol, such as, e.g., properties of the random number generator used to generate Poisson drive. Indeed: (a) The inter-arrival times of the Poisson input were very different from the time scale of the oscillations (figure 4.4G); (b) TTX like condition to remove Na^+ spikes also eliminated slow fluctuations (figure 4.4A-F).

To reveal mechanisms behind the infra-slow fluctuations, we examined the ion concentration dynamics in the Na^+/K^+ concentrations subspace of the network model phase space. In the plane of (a) extracellular K^+ vs intracellular Na^+ concentrations (figure 4.5B) or (b) the ratio of extracellular and intracellular ion concentrations (figure 4.5C) there were several regions with high density of the phase flow. A kernel density estimate (figure 4.5D) revealed the separation between these regions which suggests existence of an attractor-like dynamics and possibility of multistability between these attractors. We next detected the positive and negative peaks of the mean firing rate of the excitatory neurons (figure 4.5A). The mean time difference between the peaks (positive or negative) was 24.2 sec (with 13.27 sec standard deviation), which corresponds to 0.02-0.04 Hz in the frequency domain. Using these peaks in firing rate as time markers, we averaged the ion concentration changes during the time before and after the peaks (essentially plotting positive/negative firing rate peak triggered average). As shown in the figure 4.5F, during the time period before negative peak, the firing rate, concentrations of extracellular K^+, and intracellular Na^+ were elevated for up to ~20 sec ($p<0.001$ for t-test comparing values 20 sec before and after for all 3 variables). Similarly, the time periods (~20 sec) before positive peak (figure 4.5E) revealed reduced firing rate, concentrations of extracellular K^+, and intracellular Na^+ ($p<0.001$). We next identified the firing rate peaks and preceding 20 sec time intervals of the

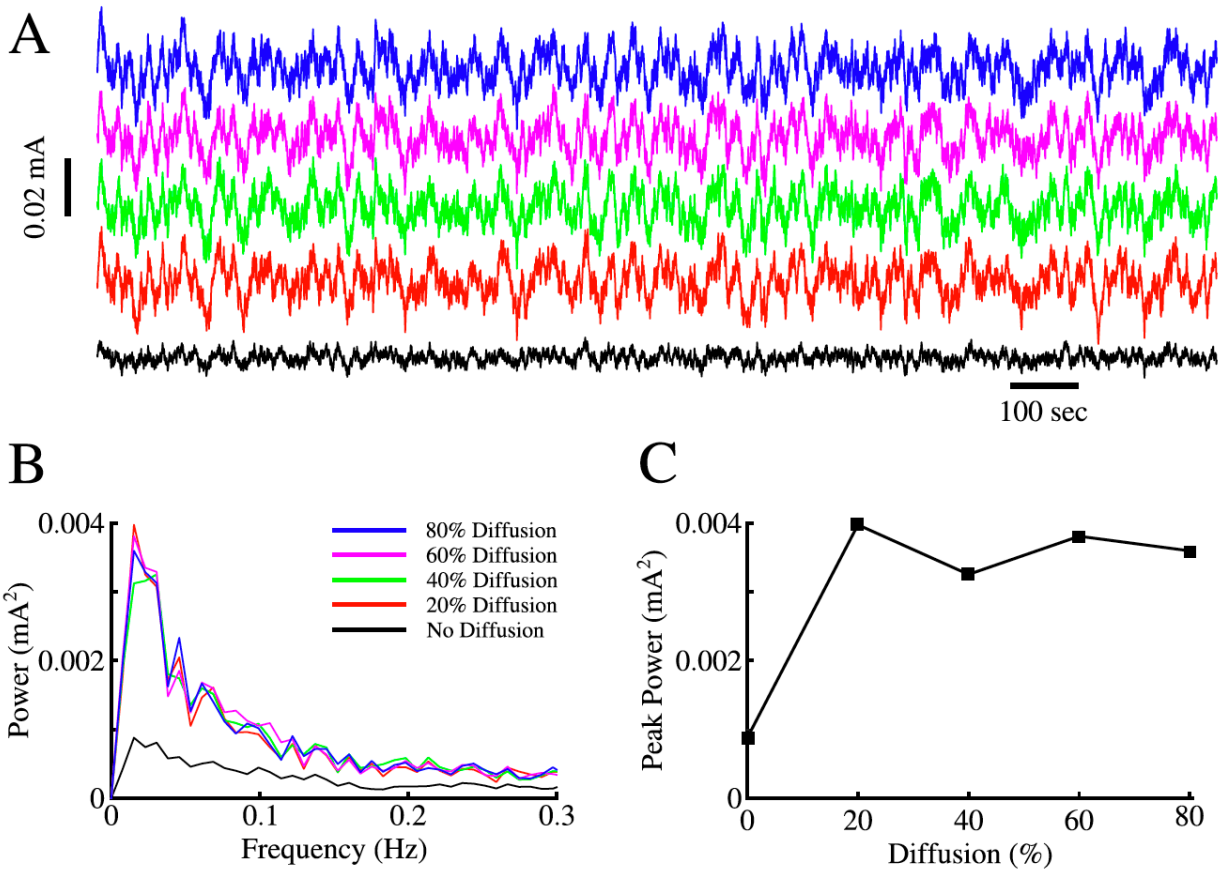

Figure 4.3 Role of diffusion in the infra-slow fluctuations. A, Mean Na^+/K^+ pump currents in the networks with different strength of diffusion. Color indicates the strength of diffusion compared to the baseline as indicated by the legend in B. **B,** Power spectrums of the Na^+/K^+ pump currents from simulations in A. **C,** Power spectrum peak power as a function of diffusion strength.

phase trajectories in the plane of extracellular K^+ and intracellular Na^+ concentrations (figure 4.5G,H). The time periods prior (after) to the positive and negative peaks were marked by red (green) in figure 4.5G-H. Importantly, these regions were clearly separated in the phase space. Together, it suggests that the observed infra-slow activity may raise from the combination of the positive and negative feedback interactions between $[K^+]_o$ /$[Na^+]_i$ and neuronal excitability, which depend on the absolute levels of the ion concentrations. Indeed, we showed before that the ion dynamics may promote positive feedbacks between the ion concentrations and neuronal excitability, while further elevation of $[K^+]_o$ and $[Na^+]_i$ may trigger negative feedbacks mediated

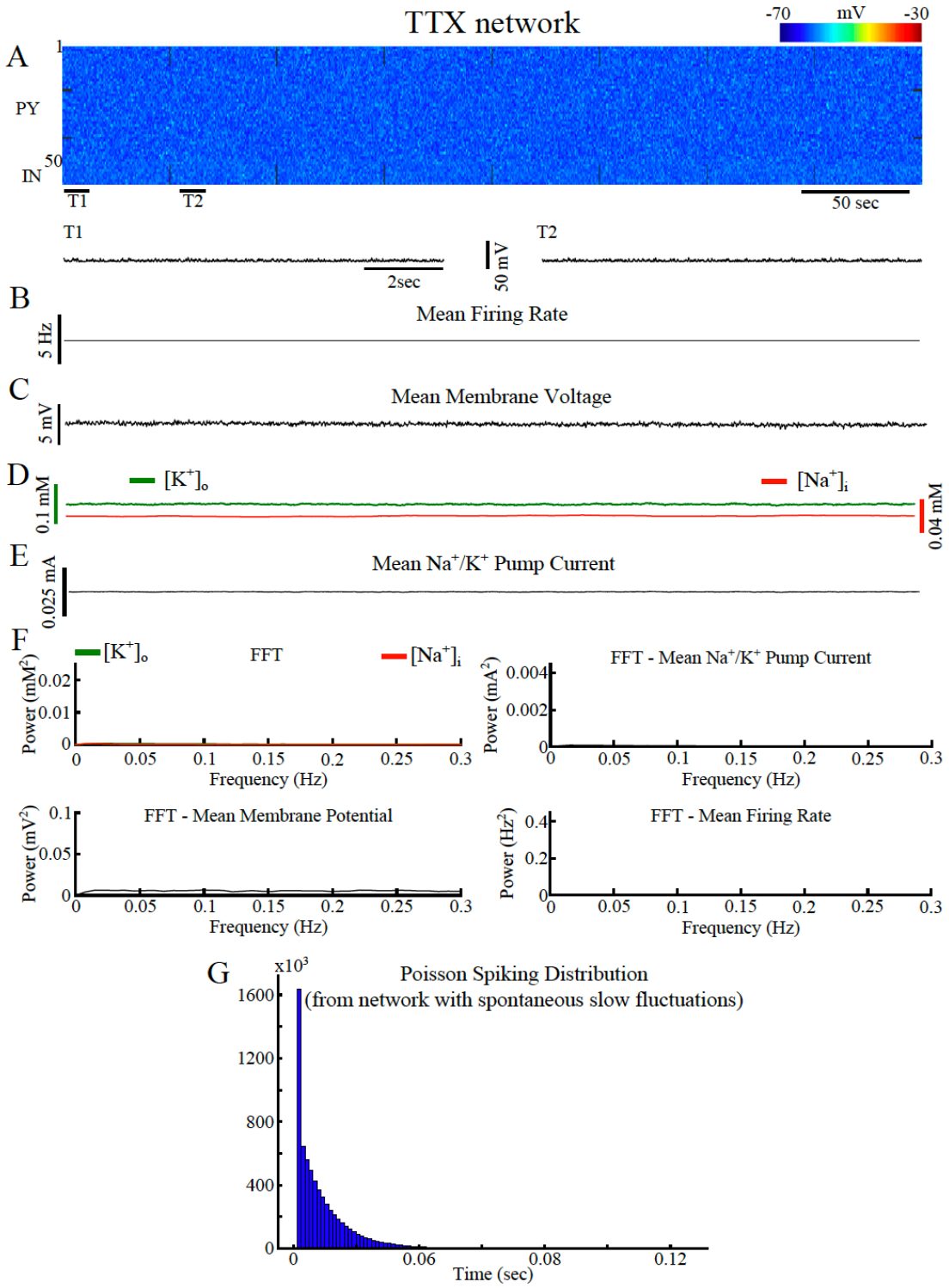

Figure 4.4 Blocking Na^+/K^+ currents responsible for cell spiking eliminates infra-slow fluctuations. A, Raster plot of spontaneous activity in a network of PY and IN neurons where all fast Na^+/K^+ currents necessary for cell spiking are blocked. T1 and T2 indicate time intervals zoomed below for the membrane voltage of a single PY neuron. **B-E,** Mean PY firing rate, mean filtered (0.001-0.1Hz) membrane voltage, $[K^+]_o$ and $[Na^+]_i$, and Na^+/K^+ pump current, respectively. Note, lack of oscillations. **F,** Power spectrums of the mean PY firing rate, membrane potential, $[K^+]_o$ and $[Na^+]_i$, and Na^+/K^+ pump current. **G,** Inter-arrival times of the Poisson process simulating synaptic release for all external synaptic inputs in the network.

by changes of the Na^+/K^+ reversal potentials and increase of the outward Na^+/K^+ pump current (Krishnan and Bazhenov, 2011).

This proposed mechanism was further verified in a simplified network model with DC input instead of stochastic Poisson drive (figure 4.6). We examined if the infra-slow fluctuations could arise in a simplified model with constant DC input, in place of the stochastic Poisson drive we have used in the rest of the simulations. Thus, we plotted the min and max values of the mean firing rate, extracellular K^+, and intracellular Na^+ concentrations as a function of the amplitude of DC input to the neurons (figure 4.6A). We observed three different regimes of activity due to constant DC input (figure 4.6A). For very low DC input, the network was silent because the input strength was below the spike generation threshold. For very high input levels (marked by red region in figure 4.6A), the network showed high frequency tonic firing. Finally, for the low intermediate inputs, the network model demonstrated oscillations between active and silent states (figure 4.6A green box; figure 4.6B). In this regime, during the silent (non-spiking) state the extracellular K^+ progressively increased because the neurons remained above the equilibrium potential for K^+. This eventually triggered a transition to the active state. During the active phase, the intracellular Na^+ progressively increased until it reached a high enough concentration that reduced intrinsic cellular excitability, due to the changes in the Na^+ reversal potentials and increase of the outward Na^+/K^+ pump current (Krishnan and Bazhenov, 2011), triggering termination of the active phase and onset of the new silent phase. Repetition of these cycles led to oscillations as confirmed by existence of the limit cycle in the phase space (figure 4.6C). This result confirms our hypothesis about the interaction of ionic and synaptic mechanism for the generation of infra-slow fluctuations in the full network with random Poisson input. We should note that the firing rates and the ion concentrations observed in the model with DC input were

Figure 4.5 Network dynamics in the phase space of ion concentrations. A, Average network firing rate (top), average $[K^+]_o$ (middle) and average $[Na^+]_i$ (bottom) of the excitatory neurons from a simulation of network with 50 excitatory and 10 inhibitory neurons. **B,** Projection of the phase space trajectories to the phase space in the plane of $[K^+]_o$ and $[Na^+]_i$. **C,** Projection of the phase space trajectories to the phase space in the plane of ratio of extracellular and intracellular ion concentrations for K^+ and Na^+. **D,** Gaussian kernel density estimate of the phase projection shown in subpanel C. **E-F,** Positive (panel E) and negative (panel F) peak triggered average of the firing rate of excitatory neurons, $[K^+]_o$, and $[Na^+]_i$ concentrations (from top to bottom). Peaks were detected by using a threshold of mean +/- 1.75 standard deviation on the firing rate. Average value is shown in black and standard deviation in blue. **G-H,** Phase space trajectories of the network dynamics in the phase space of the $[K^+]_o$ and $[Na^+]_i$ are marked in red (green) to indicate time window before (after) the positive (G) and negative (F) peaks of the firing rate.

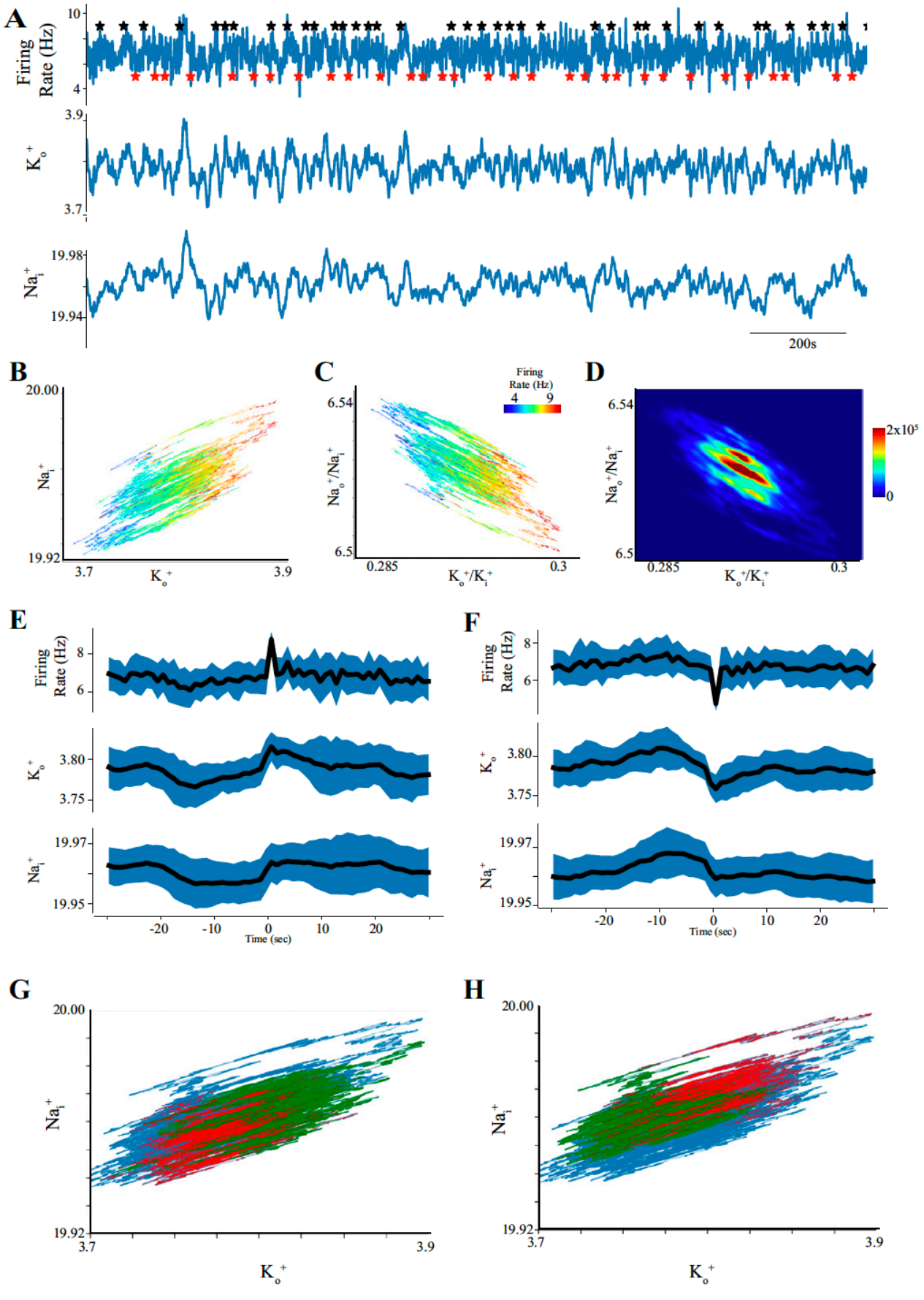
A
Firing Rate (Hz)
10
4
3.9
K_o^+
3.7
19.98
Na_i^+
19.94
200s
B
20.00
Na_i^+
19.92
3.7
K_o^+
3.9
C
Firing Rate (Hz)
4
9
6.54
Na_o^+/Na_i^+
6.5
0.285
K_o^+/K_i^+
0.3
D
6.54
Na_o^+/Na_i^+
6.5
0.285
K_o^+/K_i^+
0.3
2x10⁵
0
E
Firing Rate (Hz)
8
6
K_o^+
3.80
3.75
Na_i^+
19.97
19.95
-20
-10
0
10
20
Time (sec)
F
Firing Rate (Hz)
8
6
K_o^+
3.80
3.75
Na_i^+
19.97
19.95
-20
-10
0
10
20
Time (sec)
G
20.00
Na_i^+
19.92
3.7
K_o^+
3.9
H
20.00
Na_i^+
19.92
3.7
K_o^+
3.9

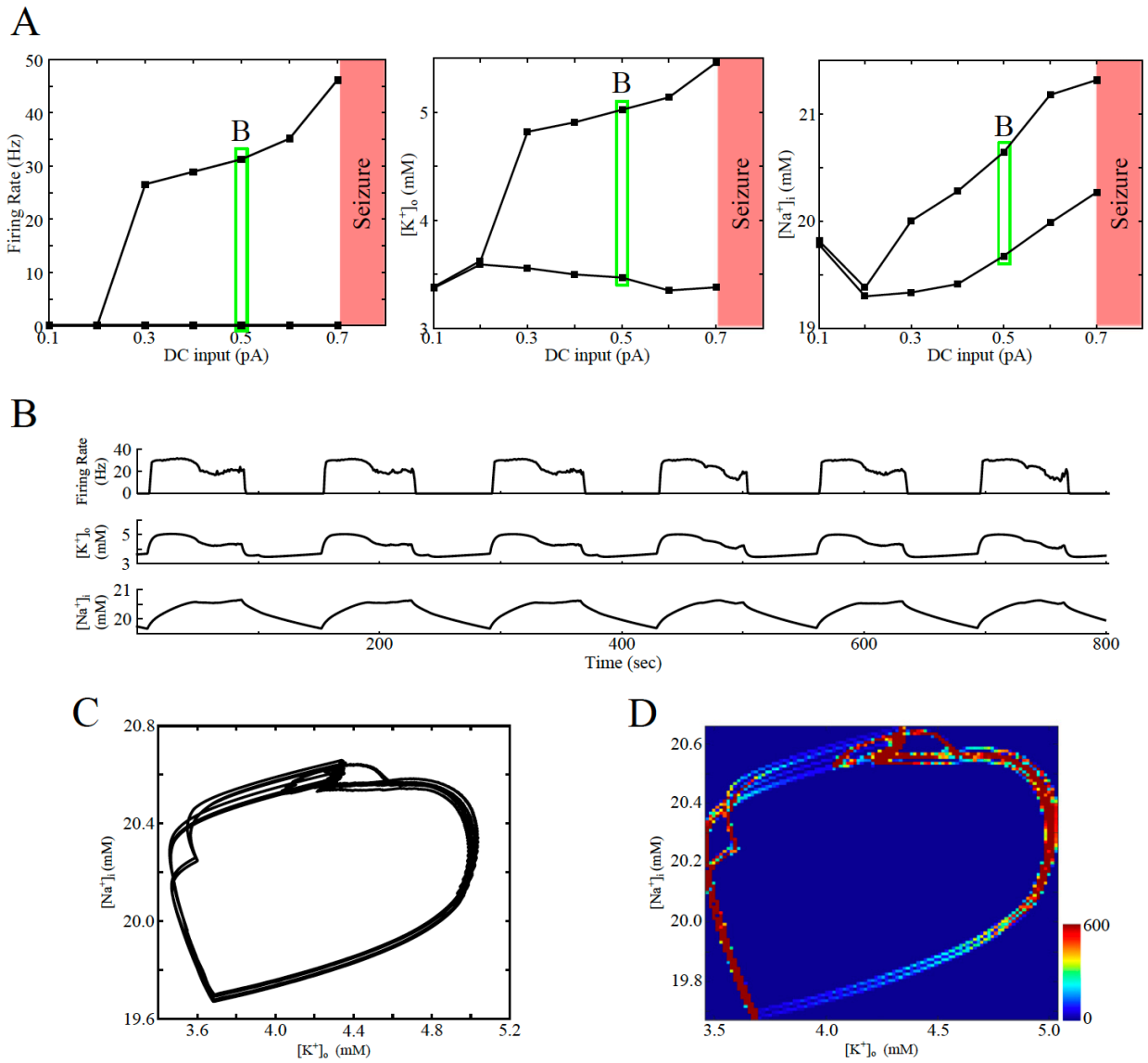

Figure 4.6 Network firing rate dynamics in response to input alternations. **A,** External input was elevated by 10% during 100 sec time window (black bar, 100-200s). Average firing rate across 10 trials is shown in red, standard deviation is shown in black. **B,** Time series of the firing rate from one trial during elevated input (black bar, 100-200s). **C,** Projection of phase trajectories to the phase plane of $[K^+]_o$ and $[Na^+]_i$ for the single trial shown in B. Color indicates different steady-states regimes and the transients to traverse between states in the phase space. **D-E,** Left, Average firing rate of excitatory neurons for different glial half activation (D) and pump strength (E) values. Firing rate traces (from top to bottom) correspond to 53, 67, 80, and 100% for D, and 90, 95, 105, 110% for E. Right, Firing rate change during the transient (100-125s) compare to the baseline (50-75s) period is plotted vs glial half activation (D) and pump strength (E).

where similar changes in the ion dynamics occurred (figure 4.5) but at a smaller degree.

To identify the time scale for variations in the ion concentration dynamics, we varied the rate of stochastic external input to the neurons in the network. In this experiment, external drive

to the network was elevated by 10% at time 100 sec and reduced to the original value at time 200 sec (figure 4.7A, solid black box indicates the period of high external input). Following increase (or decrease) in external input, the network firing rate and ion concentration displayed long transients before reaching the new steady-state values. The mean duration of the transients averaged across 10 trials was approximately 20 sec (figure 4.7A). Such transients could be also observed in the individual trials (example shown in figure 4.7B). We note that the transients observed in the individual trials closely resemble the slow fluctuations observed in the full network (compare figure 4.7B with 4.5A). In the phase space projection to the Na^+/K^+ subspace (figure 4.7C), these transients corresponded to the phase trajectories (marked by cyan and yellow) connecting regions representing network steady-states (low input – blue - and high input – green). Again, each such transient event lasted between 15-20 sec (figure 4.7C). We next examined how the transients vary with changes to the glia properties and Na^+/K^+ pump strength.

Increasing glial activation (figure 4.7D) or Na^+/K^+ pump strength (figure 4.7E) both reduced amplitude of the transients, suggesting that increasing uptake of K^+ impacts the network response characteristics. We would like to note that in this experiment we changed the input to the network as a way to reliably generate transients, however, spontaneously generated slow fluctuations in the baseline model do not arise from any changes in external input.

Does the network size affect generation of the resting-state activity? To answer this question, we increased the number of neurons in the network to 500, but kept the same network configuration as in figure 4.1 A1. Again, the network included only local connections (i.e. 5 neuron radius), and the ratio of PY to IN neurons was kept at 5:1. We found that the amplitude of the infra-slow fluctuations obtained from the averaged activity of the *entire* network was smaller than in our control 100 neurons network. To understand this phenomenon, we examined

Figure 4.7 Oscillations in the model with constant DC input. A, Min-max values of the firing rate (left), $[K^+]_o$ (middle) and $[Na^+]_i$ (right) are plotted for different levels of the DC input. **B,** Representative sample traces of the firing rate (top), $[K^+]_o$ (middle) and $[Na^+]_i$ (bottom) for DC input indicated by the green box in panel A. **C,** Projection of phase space trajectories to the plane of $[K^+]_o$ and $[Na^+]_i$ for DC input indicated by the green box in panel A. **D,** Kernel density estimate of the phase space projection shown in panel C.

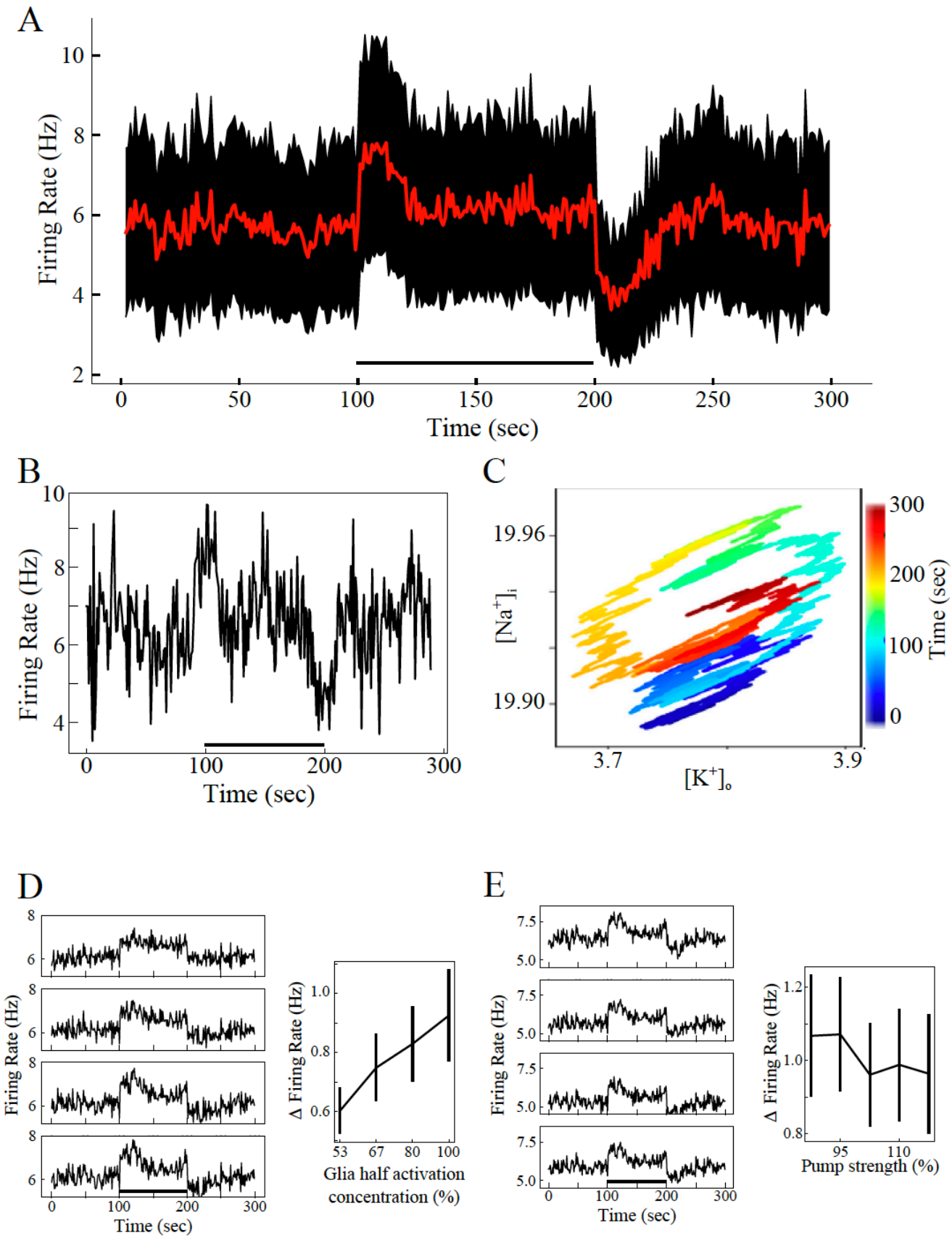
A
Firing Rate (Hz)
Time (sec)
B
Firing Rate (Hz)
Time (sec)
C
[Na+]i
[K+]o
Time (sec)
D
Firing Rate (Hz)
Time (sec)
Δ Firing Rate (Hz)
Glia half activation concentration (%)
E
Firing Rate (Hz)
Time (sec)
Δ Firing Rate (Hz)
Pump strength (%)

independently activity in the smaller subsets of neurons from the larger network (100 neurons subsets from the 500 neurons network). We observed in each such subnetwork the fluctuations of the same amplitude as we found in control small network (figure 4.8A-B). When random long-range connectivity was introduced in the 500 neurons network, we observed increase of spontaneous fluctuations. This suggests that local synaptic connections and ion diffusion were sufficient to synchronize the entire small (up to about 100 neurons) network but not the larger (e.g., 500 neurons) network. In the last case, the network activity broke into semi-independent clusters, where each cluster might oscillate out of phase with the other clusters. Long-range connections can synchronize distinct clusters. This was also further confirmed by a large-scale simulation using CoCoMac connectivity (see next section).

Feedforward connectivity influences correlations between infra-slow fluctuations

Structures comprising functional networks, such as the ventromedial prefrontal cortex (vmPFC) and posterior cingulate cortex (PCC) of the default mode network, have been shown to display coherent resting-state fluctuations (Buckner et al., 2008; Greicius et al., 2008; Broyd et al., 2009). Though fluctuations of the local ion concentrations, as proposed by our study, may underlie intrinsic fluctuations in these regions, the spatial separation of these regions makes sharing of the extracellular space between them unlikely. Therefore, these distinct regions should have independent dynamics of the local milieu of the ion concentrations. On the other hand, many brain regions are known to be connected through long-range synaptic projections. Thus, we next tested whether our model could also generate coherent fluctuations between distinct clusters of neurons connected through long-range synaptic connections where each cluster has local synaptic connectivity and local extracellular ion concentration dynamics. As depicted in figure 4.9 A1, our new network configuration consisted of two clusters of 50 excitatory neurons

Figure 4.8 Effects of network size on the resting-state fluctuation amplitude. A, Mean Na^+/K^+ pump currents from clusters of 100 neurons comprising the network of 500 neurons with only local connections. Note, lack of synchronization between individual clusters. **B,** Power spectrums calculated from the mean Na^+/K^+ pump currents in the individual clusters (colored lines match colors in A), and Power spectrum of the averaged Na^+/K^+ pump current from entire 500 neurons network (dashed line). **C,** Mean Na^+/K^+ pump current from the network of 500 neurons implementing both local and long-range connections. **D,** Power spectrum of Na^+/K^+ pump current from the network in C. Dashed lines represent SEM.

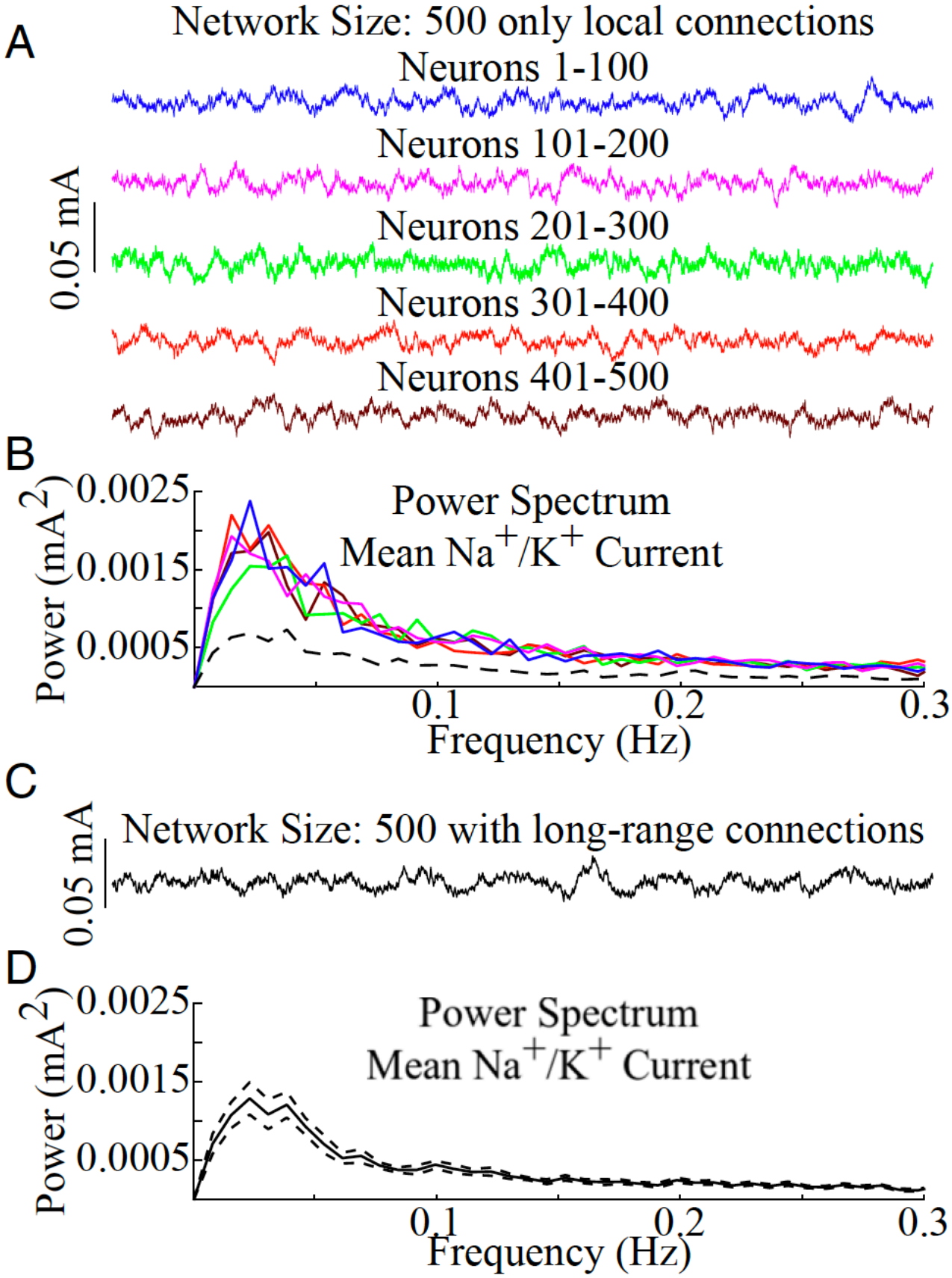
A
Network Size: 500 only local connections
Neurons 1-100
Neurons 101-200
Neurons 201-300
Neurons 301-400
Neurons 401-500
0.05 mA
B
Power Spectrum
Mean Na+/K+ Current
Power (mA2)
0.0025
0.0015
0.0005
0.1
0.2
0.3
Frequency (Hz)
C
0.05 mA
Network Size: 500 with long-range connections
D
Power Spectrum
Mean Na+/K+ Current
Power (mA2)
0.0025
0.0015
0.0005
0.1
0.2
0.3
Frequency (Hz)

and 10 inhibitory interneurons each. We kept the same connectivity scheme as the previous network configuration (figure 4.1 A1) within each neuron cluster but prevented ions from diffusing between the two clusters. Additionally, we added long-range sparse synaptic projections between two clusters through excitatory PY-PY connections. Again, the activity of the PY and IN neurons in either cluster appeared to be random (figure 4.9 A2 top). Individual traces from two PY neurons (one from each cluster) show spontaneous background activity in both clusters (figure 4.9 A2 bottom). The mean Na^+/K^+ pump current within each cluster revealed synchronized resting-state fluctuations (figure 4.9B). Power spectrum analysis of the mean Na^+/K^+ pump currents from both clusters revealed a power spectrum peak around 0.02 Hz (figure 4.9C left). Importantly, fluctuations of the mean membrane potential and mean Na^+/K^+ current of both clusters revealed positive cross-correlation (figure 4.9C middle & right respectively).

We next varied the AMPA connection strength of the long-range connections between the two clusters to test its effect on the synchronization between the resting fluctuations of the two clusters. We computed the phase-locking index (PLI) between the mean Na^+/K^+ pump currents of the two clusters for different AMPA strengths. Increasing the AMPA strength of the long-range connections resulted in higher phase-locking between the two signals (figure 4.9D left). Similarly, increasing connection probability between the two clusters resulted in an increase of the phase-locking (figure 4.9D right). Importantly, even for relatively low connection strength and probability, the PLI remained significantly higher than that for two completely disconnected clusters. Furthermore, two completely disconnected clusters did not exhibit a positive cross-correlation as seen in the connected clusters (figure 4.10).

Figure 4.9 Long-range connections synchronize resting-state fluctuations. A1, Cartoon of the network model with feedforward excitation. **A2,** Spontaneous activity in the neuron clusters connected by feedforward excitation. T1 and T2 indicate times of zoomed in single PY cell traces. **B,** Mean Na^+/K^+ pump currents for each cluster in A. **C,** Power spectrums of the Na^+/K^+ pump currents in B (left), cross-correlation of the mean filtered membrane potentials from clusters in A (middle), and cross-correlation of the mean Na^+/K^+ pump currents from B (right). **D,** Phase-locking index (PLI) as a function of feedforward AMPA strength (left) and connection probability (right). **E1,** Cartoon of the network model with feedforward inhibition. **E2,** Mean Na^+/K^+ pump currents for each cluster connected through feedforward inhibition. **F,** Power spectrums of Na^+/K^+ pump currents in E2 (left), cross-correlation of the mean filtered membrane potentials from clusters with feedforward inhibition (middle), and cross-correlation of the mean Na^+/K^+ pump currents from E2 (right).

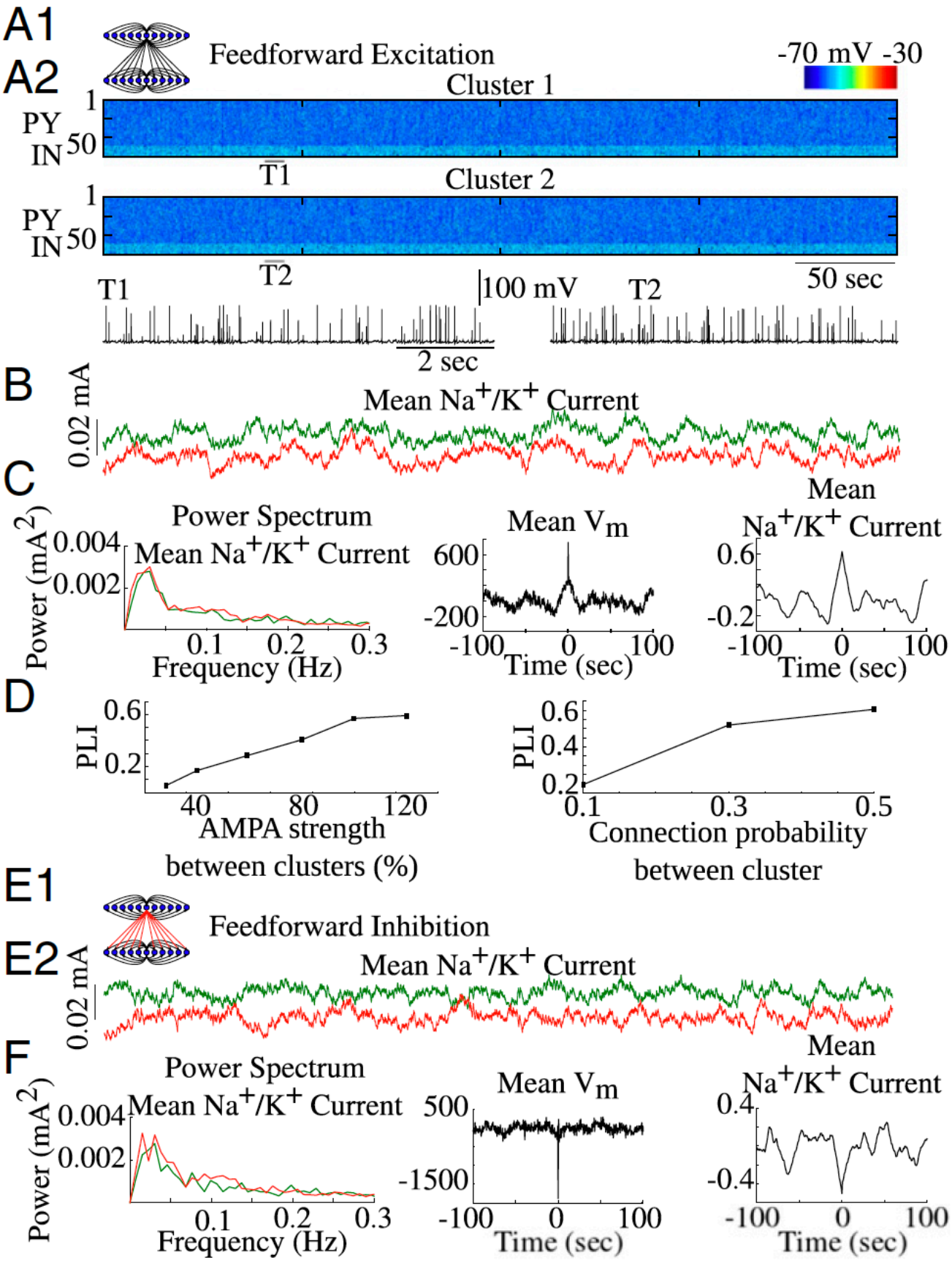
A1
A2
Feedforward Excitation
-70 mV -30
Cluster 1
PY
IN
1
50
T1
Cluster 2
T2
50 sec
100 mV
2 sec
B
0.02 mA
Mean Na+/K+ Current
C
Power Spectrum
Mean Na+/K+ Current
Power (mA2)
0.004
0.002
0.1
0.2
0.3
Frequency (Hz)
Mean Vm
600
-200
-100
0
100
Time (sec)
Mean
Na+/K+ Current
0.6
-0.2
D
PLI
0.6
0.2
40
80
120
AMPA strength
between clusters (%)
0.4
0.1
0.3
0.5
Connection probability
between cluster
E1
E2
Feedforward Inhibition
F
500
-1500
0.4
-0.4

In vivo, in addition to the positively correlated resting-state fluctuations in distinct regions, negatively or anti-correlated resting-state fluctuations have been observed (Greicius et al., 2003; Tian et al., 2007; Keller et al., 2015). We found that increasing the strength of the AMPA connection between excitatory PY neurons of the one cluster and the inhibitory IN neurons of another cluster resulted in negatively correlated resting-state fluctuations (figure 4.10E). This negatively correlated or anti-phasic activity was observed in both the filtered mean membrane potential and the mean Na^+/K^+ pump currents of the clusters (figure 4.10F, middle & right). Together, these findings suggest that the mechanisms proposed in our model can account for

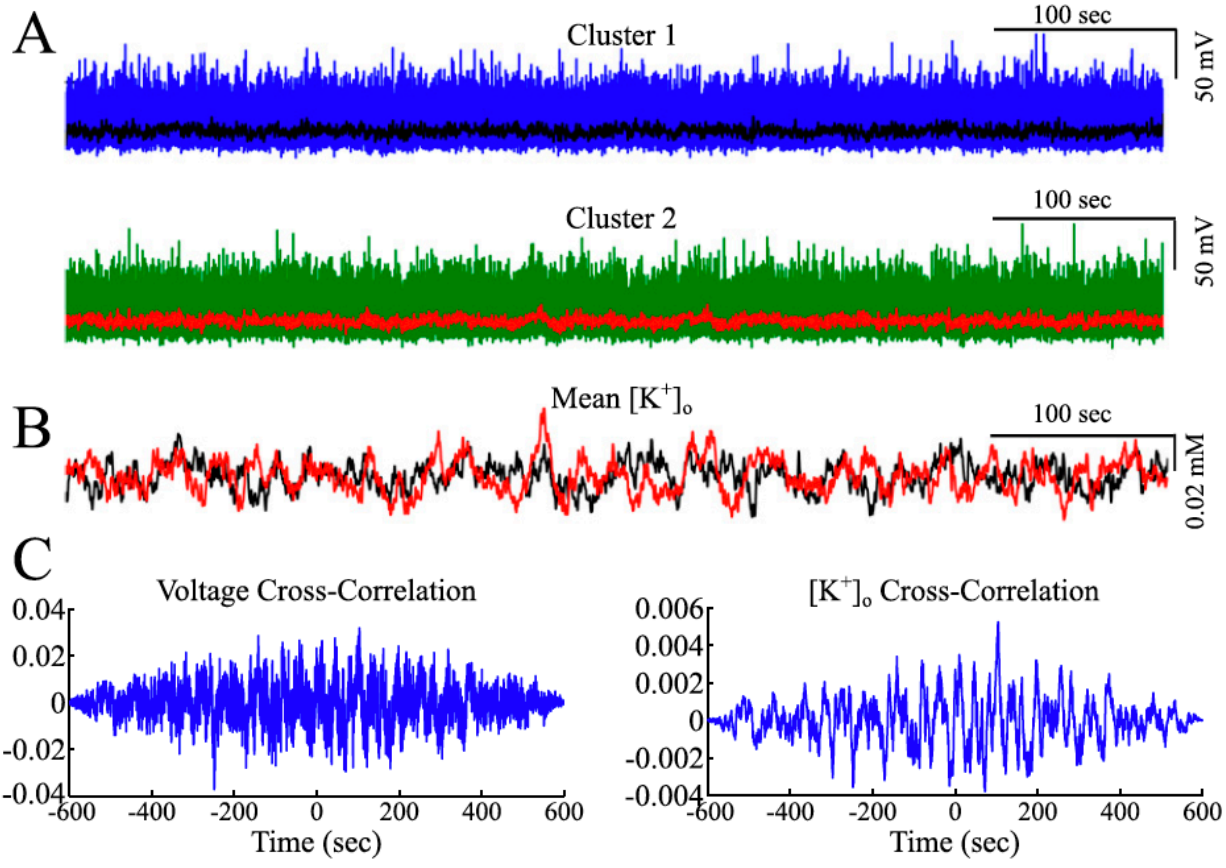

Figure 4.10 Network activity of two uncoupled clusters of neurons. A, Mean unfiltered (blue/green) and filtered (0.01-0.1 Hz) (black/red) membrane voltages from two clusters of 50PYs-10INs neurons (blue and green) with no connections between clusters. **B,** Mean $[K^+]_o$ dynamics from neuron cluster 1 (black) and 2 (red). Note lack of any synchrony between two clusters. **C,** Left, cross-correlation of the filtered mean membrane voltages of two neuron clusters 1 and 2 from A. Right, cross-correlation of the mean $[K^+]_o$ of two neuron clusters 1 and 2 from B.

individual cluster resting-state fluctuations as well as for positive and negatively correlated fluctuations between distinct brain regions.

Functional connectivity reflects the underlying structural connectivity

Finally, to test whether our model could explain *in vivo* data that revealed correlations between structural and functional connectivity in the Macaque brain (Honey et al., 2007; Deco et al., 2009; Greicius et al., 2009; Deco et al., 2011), we modeled 58 different brain regions of the Macaque brain using connectivity information gathered from the CoCoMac structural connectivity database (http://cocomac.g-node.org). Each of the 58 regions was modeled as a cluster of 50 excitatory neurons and 10 inhibitory interneurons with connectivity within a cluster identical to that shown in figure 4.1 A1. Long-range excitatory PY-PY connections were formed between clusters based on the CoCoMac structural connectivity data set (http://cocomac.g-node.org). We computed the correlation coefficient between Na^+/K^+ pump currents in different clusters for every possible pair of clusters. This analysis revealed the groups of clusters which showed high degree of correlation (figure 4.11A, middle panel). To quantify the relationship between structural and functional connectivity, we next computed the correlation coefficient between clusters (brain regions) showing significant correlation of the mean Na^+/K^+ pump currents (figure 4.11A, middle) and the clusters with strong structural connectivity (figure 4.11A, left panel). We found a significant correlation between the functional and structural connectivity ($r = 0.20508$) (figure 4.11A, right panel). Thus, we concluded that a network with local (cluster specific) ion concentration dynamics and long-range synaptic connectivity between clusters can account for the experimentally observed relationship between structural and functional connectivity. Recent data revealed the dynamic nature of functional connectivity (Hutchison et al., 2013b; Hutchison et al., 2013a; Allen et al., 2014; Shen et al., 2015). It has been shown that

Figure 4.11 Macaque simulations. A, Left, structural connectivity matrix for macaque network from the CoCoMac structural connectivity database (http://cocomac.g-node.org). Middle, functional connectivity calculated from the network model including 58 individual network clusters. Only significant correlations are shown (Bonferroni corrected for multiple comparisons). Right, correlation of functional and structural connectivity. **B,** Heatmaps, functional connectivity computed for consecutive 60sec time windows demonstrating the dynamic nature of the functional connectivity of the network model. Color indicates the correlation between infra-slow fluctuations in the simulated brain regions. Bottom plots, correlations between functional connectivity computed in corresponding heatmap and structural connectivity in A. Correlation coefficient and p-value are reported for comparison between the functional connectivity computed during each time bin and the structural connectivity in A.

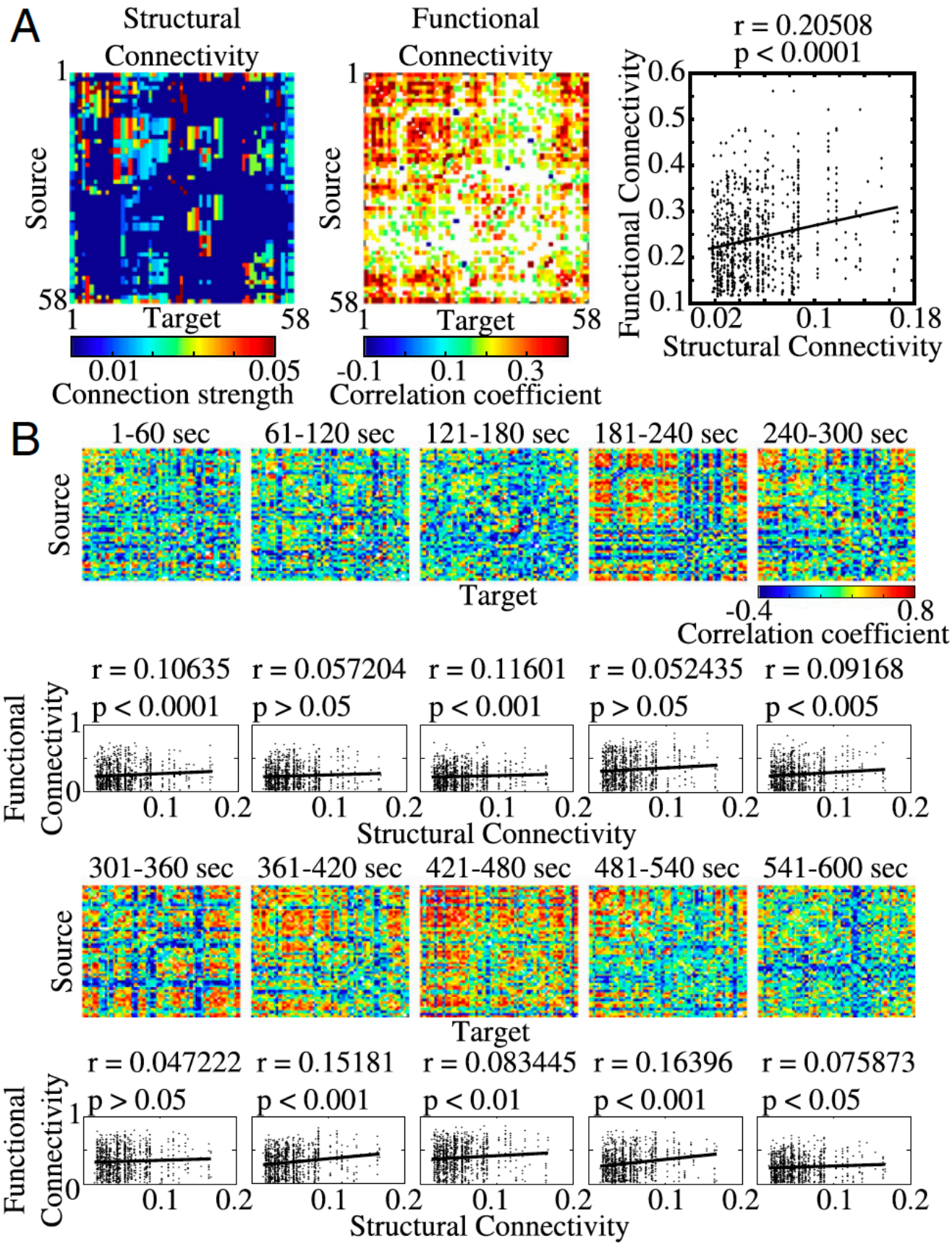
A
Structural Connectivity
Source
Target
1
58
0.01
0.05
Connection strength
Functional Connectivity
-0.1
0.1
0.3
Correlation coefficient
r = 0.20508
p < 0.0001
Functional Connectivity
Structural Connectivity
0.02
0.1
0.18
B
1-60 sec
61-120 sec
121-180 sec
181-240 sec
240-300 sec
-0.4
0.8
r = 0.10635
p < 0.0001
r = 0.057204
p > 0.05
r = 0.11601
p < 0.001
r = 0.052435
p > 0.05
r = 0.09168
p < 0.005
301-360 sec
361-420 sec
421-480 sec
481-540 sec
541-600 sec
r = 0.047222
p > 0.05
r = 0.15181
p < 0.001
r = 0.083445
p < 0.01
r = 0.16396
p < 0.001
r = 0.075873
p < 0.05

the strength of the functional connectivity computed from the resting-state fluctuations between regions comprising the default mode network was varying in time (Chang and Glover, 2010). To check for a similar characteristic in our model, we computed the correlation coefficients for ten subsequent 60sec bins (figure 4.11B). Similar to experimental findings, our model revealed dynamic changes of the functional connectivity (figure 4.11B). The network exhibited both instances of strong and weak functional connectivity between specific clusters at different time epochs. Interestingly, the regions that showed mostly weak functional connectivity could develop strong connectivity transiently in time before returning to a low connectivity state.

Discussion:

In this study, we tested the hypothesis that dynamics of the ion concentrations, regulated through the neuronal and glial activity, may form the basis of the resting-state fluctuations in the brain. Comprising only about 2% of the total body weight of an average adult human, the brain is responsible for up to 20% of the total energy consumption (Raichle, 2015). Task-evoked responses generally increase brain energy consumption by less than 5% (Raichle and Mintun, 2006). Though so much energy is consumed in order to maintain a baseline level of activity, little is known about its use, including spontaneous resting-state activity in the brain. It was first observed by Biswal et al. 1995 that the spontaneous background fluctuations recorded during fMRI scans were coherent between functionally related brain regions (Biswal et al., 1995). Since then, other studies have shown similar coherent resting-state activity between regions comprising functional networks such as the default mode network and executive control network (Fukunaga et al., 2006; Raichle and Mintun, 2006; Buckner et al., 2008; Greicius, 2008; Greicius et al., 2008; Broyd et al., 2009; Greicius et al., 2009; Larson-Prior et al., 2009; Raichle, 2011, 2015). Interestingly, infra-slow (<0.2Hz) resting-state fluctuations have been observed in various

cognitive states (Fukunaga et al., 2006; Greicius et al., 2008; Larson-Prior et al., 2009; Picchioni et al., 2011), and can exhibit modified temporal coherence patterns in various neurological and psychiatric disorders (Vanhatalo et al., 2004; Buckner et al., 2008; Greicius, 2008; Broyd et al., 2009; Zhang and Raichle, 2010). In our new study we proposed and tested the hypothesis that resting-state fluctuations may depend on the ion concentration dynamics, specifically $[K^+]_o$ fluctuations, and that the phase coherence of the infra-slow activities between distinct brain regions depends on the long-range synaptic connectivity between these regions. Our model based on the CoCoMac structural connectivity database explained the relationship between structural and functional connectivity revealed in the studies of the resting-state activity in the Macaque brain.

Ion fluctuations on the infra-slow time scale

The characteristic time scale of the resting-state fluctuations is of the order of 50-100sec. Very few neural processes are known to act at such slow time scale. In our new study, we demonstrate that the ion concentrations may spontaneously vary with a very slow time scale and could act as the modulator of the neural activity leading to emergence of resting-state fluctuations. The underlying mechanisms generating this infra-slow activity may rest in the slow processes leading to the gradual accumulation and removal of the extracellular K^+. Indeed, increase of the extracellular K^+ results in higher excitability of neurons which may then trigger further elevation of extracellular K^+, leading to the positive feedback loop (Frohlich and Bazhenov, 2006; Frohlich et al., 2008b; Krishnan and Bazhenov, 2011; González et al., 2015). Operation of this feedback depends on the intracellular Na^+; its increase leads to reduction of intrinsic excitability (Krishnan and Bazhenov, 2011). We propose here that the positive feedback mediates increase of the extracellular K^+ and its time scale can be arbitrarily slow being

determined by the balance of the inward and outward K^+ flux. Increase in the intracellular Na^+ terminates the positive feedback loop initiating a phase of progressive decrease of the ion concentrations and firing rate; this again can be arbitrarily slow. When intracellular Na^+ reduces sufficiently to recover the critical level of excitability, a new cycle of activity starts. Transitions between these phases depend on the Na^+/K^+ pump that becomes significantly more activated as the K^+ and Na^+ reach critical values leading to changes of the outward pump current and affecting intrinsic excitability. Indeed, experimental data suggested that the ion concentrations may have slow dynamics similar to the time course of the resting-state fluctuations (Moody et al., 1974; Pedley et al., 1974; McCreery and Agnew, 1983; Traynelis and Dingledine, 1988; Chub and O'Donovan, 2001; Somjen, 2002; Bazhenov et al., 2004; Chub et al., 2006; Frohlich and Bazhenov, 2006; Frohlich et al., 2008b; Wei et al., 2014a). Our previous modeling studies revealed that the ion concentration dynamics may lead to the slow (<0.2 Hz) quasi-periodic transitions between distinct network states (bursting and tonic firing) (Moody et al., 1974; Pedley et al., 1974; McCreery and Agnew, 1983; Traynelis and Dingledine, 1988; Somjen, 2002; Bazhenov et al., 2004; Frohlich and Bazhenov, 2006; Frohlich et al., 2006; Frohlich et al., 2008b; Krishnan and Bazhenov, 2011; Wei et al., 2014a). Other studies have suggested the role of slow processes involving ion dynamics and Na^+/K^+ pump activity in information processing (Arganda et al., 2007; Forrest, 2014).

The gradual accumulation of extracellular K^+ has been suggested to contribute to development of seizure-like discharges (Frohlich and Bazhenov, 2006; Frohlich et al., 2008b; Krishnan and Bazhenov, 2011; Wei et al., 2014a; González et al., 2015). Studies in patients with epilepsy revealed abnormal resting-state fluctuations (Vanhatalo et al., 2004; Lui et al., 2008; Gupta et al., 2017). Indeed, it has been demonstrated that the amplitude of resting-state

fluctuations in epileptic patients is increased as compared to the healthy individuals (Gupta et al., 2017). Interestingly, our previous work demonstrated that homeostatic up-regulation of excitatory connections, following trauma, may lead to rewiring long-range cortical connectivity and promote spontaneous seizures, along with relatively high amplitude very slow baseline fluctuations (González et al., 2015). Taken together, these results may explain differences in the resting-state fluctuation properties in epileptic patients and healthy individuals.

Relationship between structural and function connectivity

Studies in animals revealed a correlation between anatomical structural and functional connectivity (Honey et al., 2007; Deco et al., 2009; Greicius et al., 2009; Deco et al., 2011). It was proposed with computer models that the time scale of infra-slow fluctuations could be a result of transient bouts of synchrony between clusters of nodes, and that the functional connectivity arising in the network strongly reflected the underlying structural architecture (Honey et al., 2007; Deco et al., 2009). Phase-locking between distant network sites through long-range connections was reported in the mean-field type models (Honey et al., 2007; Ghosh et al., 2008; Greicius et al., 2009). For example, Honey et al (Honey et al., 2007) found that individual oscillating brain regions (modeled as Wilson-Cowen oscillators) may become synchronized in the presence of long-range synaptic connections. Nevertheless, phase-locking of the infra-slow activity in the network models implementing biophysical mechanisms of oscillation and sparse long-range connections, as described in our study, has not been previously reported. In agreement with previous data (Honey et al., 2007; Deco et al., 2009), functional connectivity in our model, computed over a long time window, reliably reflected the underlying structural connectivity.

Experimental work has shown that the lack of monosynaptic connections between brain regions does not accurately predict the absence of functional connectivity between those regions (Greicius et al., 2008). However, coupling strength between neuron clusters has been suggested to influence the strength of correlated and anti-correlated activity between nodes (Deco et al., 2009). In our model, the correlation and phase-locking of infra-slow fluctuations between clusters of neurons reflected the strength of excitatory connections between clusters (figure 4.9D). Stronger excitatory projections resulted in correlated activity and phase-locking of the infra-slow fluctuations. We found that feedforward inhibition could give rise to anti-correlated activity between neuronal clusters (figure 4.9E and F) and we observed dynamic changes of the functional connectivity over time, in agreement to the experimental studies (Hutchison et al., 2013b; Hutchison et al., 2013a; Allen et al., 2014; Shen et al., 2015).

Recent experimental work has shown that fluctuations in the fMRI BOLD signals are well correlated with the local field potentials (LFPs) (He et al., 2008; Khader et al., 2008; Raichle, 2010; Picchioni et al., 2011; Scheeringa et al., 2011; Palva and Palva, 2012; Pan et al., 2013; Hiltunen et al., 2014). Gamma band activity and slow cortical potentials (SCPs) have been shown to correlate with BOLD signals (Khader et al., 2008; Raichle, 2010, 2015). Similar to BOLD signals, SCPs show coherent activity patterns across various cognitive states. It has been suggested that the time scale of these SCPs may reflect slow metabolic processes occurring within populations of neurons (Raichle, 2010, 2015). Aerobic glycolysis accounts for ~15% of the glucose metabolized at rest (Raichle, 2010). The main glucose metabolite is ATP, a percentage of which is consumed by the Na^+/K^+ pump in order to maintain ionic gradients (Attwell and Laughlin, 2001; Cunningham et al., 2006). Other major energy demanding processes include neurotransmitter release and recycling, as well as lipid synthesis (Attwell and

Laughlin, 2001; Lennie, 2003). Modifying glucose concentration has been shown to modulate slow wave oscillations *in vitro* in rat entorhinal cortex (Cunningham et al., 2006). In agreement with these results, our model suggests that Na^+/K^+ pump activity may influence the properties of the infra-slow fluctuations. Na^+/K^+ pump activity is reflected in fMRI BOLD signals as oxygenated blood flow increases to brain regions exhibiting increased neuronal activity (Arthurs and Boniface, 2002). It suggests that taking into account effects of the ion concentrations and Na^+/K^+ pump dynamics, as implemented in our model, may be necessary to accurately capture the biophysical mechanisms leading to generation of infra-slow fluctuations in fMRI recordings.

Resting-state infra-slow fluctuations were originally observed during baseline recordings of the BOLD signals in fMRI studies (Raichle and Mintun, 2006; He et al., 2008; Raichle, 2010, 2011, 2015). Changes in oxygen consumption, a result of re-establishing ion gradients through active pumping following increases in activity, give rise to fluctuations in BOLD signals (Greicius et al., 2003; Greicius, 2008; Greicius et al., 2008; He et al., 2008; Raichle, 2011). Through oxidative phosphorylation, oxygen allows for the production of ATP, thereby providing the cells with energy necessary to, amongst other processes, re-establish ionic gradients through ion pumping (Wei et al., 2014b). As such, the production of ATP is limited by the time scale of oxygen consumption and the replenishing of oxygen/glucose reservoirs (Ingram et al., 2014; Wei et al., 2014b). The flux in glucose/oxygen consumption, and neuro-vascular coupling have been suggested to occur on a slow time scale leading to the slow network dynamics (Ingram et al., 2014; Wei et al., 2014b; Wei et al., 2014a; Longden et al., 2017). Our model does not explore the neuro-vascular coupling, but rather focuses on the mechanisms arising from the interaction between neuronal and ion concentration dynamics. Future work exploring the interaction between neuronal and vascular dynamics is needed to advance our understanding of the complex

mosaic of the interacting biophysical mechanisms underlying the BOLD signal and may provide insights into how altered brain and disease states influence resting-state oscillations.

Materials and Methods:

Computational Model. Our network model with dynamics ion concentrations has been described in detail elsewhere (Bazhenov et al., 2004; Frohlich and Bazhenov, 2006; Krishnan and Bazhenov, 2011; González et al., 2015). Briefly, our network consisted of populations of excitatory pyramidal (PY) neurons and inhibitory interneurons (IN) with a 5:1 ratio. Both neuron types were modeled as two-compartmental conductance-base neurons with an axosomatic and dendritic compartments and Hodgkin-Huxley type ionic currents. Ion concentration dynamics were implemented for intracellular and extracellular K^+ and Na^+, and intracellular Cl^- and Ca^{2+}. Na^+/K^+ pump Na^+ and K^+ regulation and KCC2 cotransporter Cl^- extrusion were included in both neuron types. Glial regulation of extracellular K^+ was modeled as a free buffer as described in our previous work (Krishnan and Bazhenov, 2011; González et al., 2015; Krishnan et al., 2015).

Excitatory synaptic connections were mediated through AMPA and NMDA conductances and inhibitory synaptic connections were mediated through $GABA_A$. Local connectivity (within a single cluster) was restricted to a radius of 5 neurons for PY-PY connections. Long-range connections between clusters (ie. feedforward excitation or inhibition) were mediated by AMPA and NMDA conductances between PYs from one cluster to PYs (feedforward excitation) or INs (feedforward inhibition) of second cluster with a twenty-five percent connection probability. For Macaque simulations, 58 brain regions were modeled as independent clusters of neurons with long-range connections between clusters based on structural connectivity data from CoCoMac database (http://cocomac.g-node.org). Functional

connectivity was computed as the correlation coefficients between mean Na^+/K^+ pump currents from the individual clusters.

Intrinsic properties and ion dynamics of excitatory and inhibitory neuron models. Our network model with dynamics ion concentrations has been described in detail elsewhere (Bazhenov et al., 2004; Frohlich and Bazhenov, 2006; Krishnan and Bazhenov, 2011; González et al., 2015; Krishnan et al., 2015). Briefly, both excitatory pyramidal cells (PYs) and inhibitory interneurons (INs) were modeled as two-compartment neurons with an axosomatic and a dendritic compartment. The evolution of voltage in time for each compartment was described by the following equations:

$$C_m \frac{dV_D}{dt} = -g_D^c(V_D - V_S) - I_D^{leak} - I_D^{pump} - I_D^{Int}$$

$$g_S^c(V_D - V_S) = -I_S^{leak} - I_S^{pump} - I_S^{Int}$$

where $V_{D,S}$ are the voltages of the dendritic and axosomatic compartments (respectively), I_D^{leak} and I_S^{leak} are the sum of the ionic leak currents, I_D^{pump} and I_S^{pump} are the sum of the Na^+ and K^+ currents through the Na^+/K^+ pump, and I_D^{Int} and I_S^{Int} are the intrinsic currents for the dendritic and axosomatic compartments respectively. Each of these compartments contained conductance-based Hodgkin-Huxley type ionic currents. The ionic current intrinsic to the dendritic compartment include the fast sodium (I_{Na}), persistent sodium current (I_{NaP}), slowly activating potassium current (I_{Km}), high-threshold calcium current (I_{Ca}), calcium-activated potassium current (I_{KCa}), hyperpolarization-activated depolarizing mix cationic currents (I_h), and leak currents (Krishnan and Bazhenov, 2011; González et al., 2015; Krishnan et al., 2015). The axosomatic compartment contains the fast sodium current (I_{Na}), the persistent sodium current (I_{NaP}), delayed-rectifier potassium current (I_{Kv}), and the sodium-activated potassium current (I_{KNa}). Na^+/K^+ pump Na^+ and K^+ regulation and KCC2 cotransporter Cl^- extrusion were included

in both neuron types. Additionally, dynamic ion concentrations for extracellular and intracellular Na^+ and K^+ as well as intracellular Cl^- and Ca^{2+} were determined by the intrinsic currents, transporter-mediated currents, leak currents, extracellular and intracellular diffusion, and glial $[K^+]_o$ buffering as described in the following equations:

$$\frac{d[K^+]_o}{dt} = \left(\frac{k}{Fd}\right)\left(I_K^{pump} + I_{\sum K}^{Int}\right) + \delta_o\left(\frac{([K^+]_{o-1} + [K^+]_{o+1})}{2} - [K^+]_o\right) + \delta_o([K^+]_{oc} - [K^+]_o) + G$$

$$G = k_1([B]_{max} - [B]) - k_2[K^+]_o[B]$$

$$\frac{d[B]}{dt} = k_1([B]_{max} - [B]) - k_2[K^+]_o[B]$$

$$\frac{d[K^+]_i}{dt} = -\left(\frac{k}{F}\right)\left(I_K^{pump} + I_{\sum K}^{Int}\right) + \delta_i([K^+]_{ic} - [K^+]_o)$$

$$\frac{d[Na^+]_o}{dt} = \left(\frac{k}{Fd}\right)\left(I_{Na}^{pump} + I_{\sum Na}^{Int}\right) + \delta_o\left(\frac{([Na^+]_{o-1} + [Na^+]_{o+1})}{2} - [Na^+]_o\right)$$

$$+ \delta_o([Na^+]_{oc} - [Na^+]_o)$$

$$\frac{d[Na^+]_i}{dt} = -\left(\frac{k}{F}\right)\left(I_{Na}^{pump} + I_{\sum Na}^{Int}\right) + \delta_i([Na^+]_{ic} - [Na^+]_o)$$

$$\frac{d[Cl^-]_i}{dt} = -\left(\frac{k}{F}\right) I_{\sum Cl}^{Int} + \left(\frac{[Cl^-]_{i\infty} + [Cl^-]_i}{\tau_{Cl}}\right)$$

$$\tau_{Cl} = \left(100 + \frac{\tau_{Cl\infty}}{\left(1 + \exp\left([Cl^-]_{i\infty} - \frac{[K^+]_o}{\tau_{KoCl}}\right)\right)}\right)$$

$$\frac{d[Ca^{2+}]_i}{dt} = \frac{(-5.1819 \times 10^{-5} I_{Ca})}{D_{Ca}} + \left(2.4 \times 10^{-4} - \frac{[Ca^{2+}]_i}{\tau_{Ca}}\right)$$

where F = 96489 C/mol, d = 0.15 is the ratio of the extracellular compartment volume to surface area, the conversion factor k = 10, δ_o is the scaled diffusion coefficient ($\delta_o = D/\Delta x$) where D = 6x10^{-6} cm^2/s is the diffusion constant and Δx = 100 μm is distance, $[K^+]_{oc}$ and $[Na^+]_{oc}$ are the

K^+ and Na^+ concentrations in the adjacent compartments, and $[K^+]_{o-1}$, $[K^+]_{o+1}$, $[Na^+]_{o-1}$, and $[Na^+]_{o+1}$ are the concentrations of K^+ and Na^+ in neighboring cells respectively. Glial buffering of extracellular K^+ (G) was modeled as a free buffer ($[B]$) with total buffer ($[B]_{max}$) = 500mM. The $[B]$ K^+ binding and unbinding rates (k_1 and k_2 respectively) were given by k_1 = 0.0008 and $k_2 = k_1/(1 + exp(([K^+]_o - [K^+]_{oth})/(-1.05)))$, where $[K^+]_{oth}$ = 15mM is the half activation concentration of $[K^+]_o$. $[Cl^-]_{i\infty}$ = 5mM, $\tau_{Cl\infty}$ = 2x10^4, and τ_{KoCl} = 0.08s. τ_{Ca} and D_{Ca} were set to 300ms and 0.85 respectively. Extracellular space in our model was constrained between neurons, and we modeled individual extracellular space for each neuron with local ion diffusion between nearest neighbors (ie. diffusion between PY-PYs and IN-INs). Additionally, the extracellular space was tightly bounded between the glia and neurons, and there was an instantaneous and direct impact of ion concentration changes in the extracellular space on the neuronal and glial activity. While equations for glial K^+ buffering and chloride transport include some slow time constants, these processes are much faster than the observed infra-slow neural dynamics arising in the network.

Network and synaptic properties. The network model was modeled as a one-dimensional network and consisted of 50 (or 500) excitatory PY neurons and 10 (or 100) inhibitory IN neurons. Each PY neuron made local excitatory connections onto 10 other PY neurons and received 10 excitatory connections from other PY neurons. PY neurons also formed excitatory connections onto inhibitory IN neurons. Each PY projected onto one IN and each IN formed inhibitory connections onto 5 PY neurons. Excitatory connections were mediated by AMPA and NMDA conductances (11 nS and 1 nS, respectively), and inhibitory connections were mediated by $GABA_A$ conductances (11 nS) such as those described previously (Krishnan and Bazhenov, 2011; González et al., 2015; Krishnan et al., 2015). Excitatory connections from PY neurons

onto IN neurons were mediated by AMPA and NMDA conductances (3.5 nS and 0.35 nS, respectively). To model *in vivo* conditions, all neurons of both types received additional afferent excitatory input as a random Poisson process.

Single and double cluster network connectivity. For single cluster networks, a 1:5 ratio of IN to PY neurons was kept, regardless of the network size. Slow fluctuations were also observed in a fully connected network. As previously mentioned, local diffusion of K^+ was allowed between PY-PY and IN-IN but not between PY and IN neurons.

To study synchronization between clusters of neurons, we generated a network model consisting of two clusters. Each cluster included 50 PY neurons and 10 INs. Additionally, ion diffusion was not allowed between the clusters. In order to connect two clusters, PY neurons were allowed to make long-range PY-PY and PY-IN connections between clusters with twenty-five percent connection probability (unless otherwise stated). Results of varying the probability of long-range connections are shown in Figure 4.9. Long-range connection probabilities and strengths were varied in ordered to study how these connection properties influence correlation between cluster oscillations.

Phase-locking analysis. Phase-locking was used to study the synchrony between two fluctuations in two clusters. The phase-locking index (PLI) between two clusters (x_1 and x_2) was computed as follows:

$$\delta_\phi = angle\big(H(x_1)\big) - angle\big(H(x_2)\big)$$

$$PLI = | < e^{i\delta_\phi} >_t |$$

where H is the Hilbert transform, and δ_ϕ is the difference in angle between the two time series. Both time series were band-pass filtered between 0.001 and 0.1 Hz before the Hilbert transform was applied.

Macaque simulations. We developed the network model implementing the structural connectivity among 58 macaque brain regions. Connection strengths between brain regions were extracted from the CoCoMac database (http://cocomac.g-node.org). Functional connectivity was computed as the correlation coefficients between mean Na^+/K^+ pump currents from the individual clusters. Significance values were Bonferroni corrected to correct for multiple comparisons. For analysis of the dynamic nature of the resting-state fluctuations, 60sec time windows were used to compute correlation coefficients. An agglomerative hierarchical clustering (using ward distance metric) was applied to the correlation coefficient matrix consisting of all combination of clusters and was used for visualization used in Figure 4.11.

Acknowledgements

Chapter 4, in full, is a reprint of the material as it appears in Origin of Slow Spontaneous Resting-State Neuronal Fluctuations in Brain Networks 2018. Krishnan, Giri P.; González, Oscar C.; Bazhenov, Maxim. The dissertation author was the primary co-author of this paper.

Chapter 5: Conclusion

Summary:

Ionic and synaptic phenomena underlie the various electrical properties of neurons. They allow for the fast transmission of information between groups of neurons, and provide means by which brain networks can perform various computational tasks such as the processing of sensory input, transitions between various cognitive brain states, consolidation of memories, and generalization of these new memories for their incorporation into the brain's working model of the world. Because of their crucial role in various electrical properties of neurons, there exists many homeostatic mechanisms which aim to maintain healthy physiological levels of ion concentrations and synaptic currents. Though these homeostatic mechanisms are meant to

stabilize network dynamics and prevent pathological brain states in healthy brain networks, in a pathological brain, one riddled with K^+-channel defects or suffering traumatic brain injury, these mechanisms may actually destabilize the network and facilitate transitions between healthy network dynamics and pathological brain activity. Here, we explored how ionic and synaptic homeostatic mechanisms give rise to and regulate network-wide dynamics. We first described how homeostatic synaptic scaling, a negative feedback bidirectional mechanism meant to stabilize Hebbian plasticity, may underlie the epileptogenic period of post-traumatic epilepsy priming traumatized brain networks for the development of spontaneous recurrent seizures. Additionally, we predict that age-dependent impairment in the bidirectionality of this homeostatic mechanism may explain the age-related differences in susceptibility to post-traumatic epilepsy. We then explored the contribution of the KCC2 co-transporter, a homeostatic regulator of intracellular Cl^- and K^+ concentration, in the development of seizures in K^+-channelopathy-dependent genetic epilepsies. Finally, we explored how natural fluctuations in ion concentrations may underlie infra-slow resting state network fluctuations observed in fMRI and EEG. We predict that local fluctuations in extracellular K^+ concentrations may be responsible for synchronizing local populations of neurons and setting the infra-slow time scale of these resting state fluctuations, while feedforward excitatory (inhibitory) connections between ionically isolated brain regions may underlie correlated (anti-correlated) infra-slow fluctuations between brain regions comprising functionally related (opposing) brain networks such as the default mode network.

Future Directions:

Though the presence of spontaneous recurrent seizures is a hallmark of an epileptic disorder, epilepsy often presents with comorbid psychiatric disorders and cognitive impairments.

Unfortunately, much of the focus around the study of epilepsy has been on the prediction and control of seizures, while the cognitive impairments that occur during interictal or ictal periods have received much less attention. Along these lines, there is now growing evidence for altered resting state infra-slow fluctuations amongst brain regions forming functional networks involved in memory consolidation, regulation of emotion, attentional networks, etc. As such, it is likely that these altered resting state fluctuations may underlie some of the cognitive impairments observed in patients suffering from epilepsy. In my future work I aim to study how impairments in ionic and synaptic homeostasis may play a crucial role in altered infra-slow resting state fluctuations observed in epileptic patients, and how these may relate to impaired cognitive abilities such as memory impairment and hallucinations. This work may also extend to other neurological disorders such as Alzheimer's disease. Alzheimer's patients may present with sub-clinical seizure which, I suspect, may impact functional connectivity between brain regions comprising memory networks thereby impacting memory consolidation and retrieval.

Recently, I have started work on exploring the role of sleep in memory consolidation. Our recent work suggests that non-REM stage 3 slow-wave sleep may aid in the consolidation of overlapping, competing memory traces through memory replay during cortical Up-states. This, in turn, results in a restructuring of the underlie synaptic connectivity such that the same population of neurons can support the storage of overlapping memory traces without damaging either memory. Though there is growing evidence for the role of sleep in memory consolidation, the exact biophysical mechanisms underlying the biasing of network dynamics toward natural memory replay during cortical Up-states or the ionic regulation of sleep-wake transitions remains to be fully understood. I hope to bridge this gap in our knowledge by studying how changes in neuromodulatory tone during various stages of sleep impact ionic concentration dynamics

leading to changes in network dynamics allowing for memory reactivation. Additionally, altered sleep has been observed in a number of psychiatric and neurological disorders including epilepsy. To this end, I intend study how the breakdown in the regulation of ionic concentrations may lead to altered sleep architecture and how these changes may contribute to (i) seizures commonly observed at sleep-wake transitions, (ii) memory deficits, and (iii) various cognitive impairments observed not only in epilepsy but also other neurological and psychiatric disorders.

References

Achilles K, Okabe A, Ikeda M, Shimizu-Okabe C, Yamada J, Fukuda A, Luhmann HJ, Kilb W (2007) Kinetic properties of Cl uptake mediated by Na+-dependent K+-2Cl cotransport in immature rat neocortical neurons. J Neurosci 27:8616-8627.

Agrawal A, Timothy J, Pandit L, Manju M (2006) Post-traumatic epilepsy: an overview. Clinical neurology and neurosurgery 108:433-439.

Allen EA, Damaraju E, Plis SM, Erhardt EB, Eichele T, Calhoun VD (2014) Tracking whole-brain connectivity dynamics in the resting state. Cereb Cortex 24:663-676.

Angeleri F, Majkowski J, Cacchio G, Sobieszek A, D'Acunto S, Gesuita R, Bachleda A, Polonara G, Krolicki L, Signorino M, Salvolini U (1999) Posttraumatic epilepsy risk factors: one-year prospective study after head injury. Epilepsia 40:1222-1230.

Annegers JF, Hauser WA, Coan SP, Rocca WA (1998) A population-based study of seizures after traumatic brain injuries. The New England journal of medicine 338:20-24.

Arganda S, Guantes R, de Polavieja GG (2007) Sodium pumps adapt spike bursting to stimulus statistics. Nat Neurosci 10:1467-1473.

Arthurs OJ, Boniface S (2002) How well do we understand the neural origins of the fMRI BOLD signal? Trends Neurosci 25:27-31.

Asikainen I, Kaste M, Sarna S (1999) Early and late posttraumatic seizures in traumatic brain injury rehabilitation patients: brain injury factors causing late seizures and influence of seizures on long-term outcome. Epilepsia 40:584-589.

Attwell D, Laughlin SB (2001) An energy budget for signaling in the grey matter of the brain. J Cereb Blood Flow Metab 21:1133-1145.

Avoli M, de Curtis M (2011) GABAergic synchronization in the limbic system and its role in the generation of epileptiform activity. Prog Neurobiol 95:104-132.

Avoli M, Barbarosie M, Lucke A, Nagao T, Lopantsev V, Kohling R (1996) Synchronous GABA-mediated potentials and epileptiform discharges in the rat limbic system in vitro. J Neurosci 16:3912-3924.

Avoli M, de Curtis M, Gnatkovsky V, Gotman J, Kohling R, Levesque M, Manseau F, Shiri Z, Williams S (2016) Specific imbalance of excitatory/inhibitory signaling establishes seizure onset pattern in temporal lobe epilepsy. J Neurophysiol 115:3229-3237.

Avramescu S, Timofeev I (2008) Synaptic strength modulation after cortical trauma: a role in epileptogenesis. J Neurosci 28:6760-6772.

Barnwell LF, Lugo JN, Lee WL, Willis SE, Gertz SJ, Hrachovy RA, Anderson AE (2009) Kv4.2 knockout mice demonstrate increased susceptibility to convulsant stimulation. Epilepsia 50:1741-1751.

Bartolomei F, Chauvel P, Wendling F (2008) Epileptogenicity of brain structures in human temporal lobe epilepsy: a quantified study from intracerebral EEG. Brain 131:1818-1830.

Bartolomei F, Khalil M, Wendling F, Sontheimer A, Regis J, Ranjeva JP, Guye M, Chauvel P (2005) Entorhinal cortex involvement in human mesial temporal lobe epilepsy: an electrophysiologic and volumetric study. Epilepsia 46:677-687.

Bazhenov M, Timofeev I, Steriade M, Sejnowski TJ (2002) Model of thalamocortical slow-wave sleep oscillations and transitions to activated States. J Neurosci 22:8691-8704.

Bazhenov M, Timofeev I, Steriade M, Sejnowski TJ (2004) Potassium model for slow (2-3 Hz) in vivo neocortical paroxysmal oscillations. J Neurophysiol 92:1116-1132.

Bean BP (2007) The action potential in mammalian central neurons. Nat Rev Neurosci 8:451-465.

Ben-Ari Y, Krnjević K, Reinhardt W (1979) Hippocampal seizures and failure of inhibition. Canadian Journal of Physiology and Pharmacology 57:1462-1466.

Ben-Ari Y, Gaiarsa JL, Tyzio R, Khazipov R (2007) GABA: a pioneer transmitter that excites immature neurons and generates primitive oscillations. Physiological reviews 87:1215-1284.

Biswal B, Yetkin FZ, Haughton VM, Hyde JS (1995) Functional connectivity in the motor cortex of resting human brain using echo-planar MRI. Magn Reson Med 34:537-541.

Braganza O, Bedner P, Huttmann K, von Staden E, Friedman A, Seifert G, Steinhauser C (2012) Albumin is taken up by hippocampal NG2 cells and astrocytes and decreases gap junction coupling. Epilepsia 53:1898-1906.

Brodie MJ, French JA (2000) Management of epilepsy in adolescents and adults. Lancet 356:323-329.

Brodie MJ, Kwan P (2001) The star systems: overview and use in determining antiepileptic drug choice. CNS Drugs 15:1-12; discussion 13-15.

Brown RE, Basheer R, McKenna JT, Strecker RE, McCarley RW (2012) Control of sleep and wakefulness. Physiological reviews 92:1087-1187.

Broyd SJ, Demanuele C, Debener S, Helps SK, James CJ, Sonuga-Barke EJ (2009) Default-mode brain dysfunction in mental disorders: a systematic review. Neurosci Biobehav Rev 33:279-296.

Buchin A, Chizhov A, Huberfeld G, Miles R, Gutkin BS (2016) Reduced Efficacy of the KCC2 Cotransporter Promotes Epileptic Oscillations in a Subiculum Network Model. J Neurosci 36:11619-11633.

Buckner RL, Andrews-Hanna JR, Schacter DL (2008) The brain's default network: anatomy, function, and relevance to disease. Ann N Y Acad Sci 1124:1-38.

Burrone J, Murthy VN (2003) Synaptic gain control and homeostasis. Curr Opin Neurobiol 13:560-567.

Carmichael ST, Chesselet MF (2002) Synchronous neuronal activity is a signal for axonal sprouting after cortical lesions in the adult. J Neurosci 22:6062-6070.

Cataldi M, Avoli M, de Villers-Sidani E (2013) Resting state networks in temporal lobe epilepsy. Epilepsia 54:2048-2059.

Chang BS, Lowenstein DH, Quality Standards Subcommittee of the American Academy of N (2003) Practice parameter: antiepileptic drug prophylaxis in severe traumatic brain injury: report of the Quality Standards Subcommittee of the American Academy of Neurology. Neurology 60:10-16.

Chang C, Glover GH (2010) Time-frequency dynamics of resting-state brain connectivity measured with fMRI. Neuroimage 50:81-98.

Chauvette S, Soltani S, Seigneur J, Timofeev I (2016) In vivo models of cortical acquired epilepsy. J Neurosci Methods 260:185-201.

Chever O, Djukic B, McCarthy KD, Amzica F (2010) Implication of Kir4.1 channel in excess potassium clearance: an in vivo study on anesthetized glial-conditional Kir4.1 knock-out mice. J Neurosci 30:15769-15777.

Christensen J, Pedersen MG, Pedersen CB, Sidenius P, Olsen J, Vestergaard M (2009) Long-term risk of epilepsy after traumatic brain injury in children and young adults: a population-based cohort study. Lancet 373:1105-1110.

Chub N, O'Donovan MJ (2001) Post-episode depression of GABAergic transmission in spinal neurons of the chick embryo. J Neurophysiol 85:2166-2176.

Chub N, Mentis GZ, O'Donovan M J (2006) Chloride-sensitive MEQ fluorescence in chick embryo motoneurons following manipulations of chloride and during spontaneous network activity. J Neurophysiol 95:323-330.

Cohen I, Navarro V, Clemenceau S, Baulac M, Miles R (2002) On the origin of interictal activity in human temporal lobe epilepsy in vitro. Science 298:1418-1421.

Coulter DA, Steinhauser C (2015) Role of astrocytes in epilepsy. Cold Spring Harb Perspect Med 5:a022434.

Cressman JR, Jr., Ullah G, Ziburkus J, Schiff SJ, Barreto E (2009) The influence of sodium and potassium dynamics on excitability, seizures, and the stability of persistent states: I. Single neuron dynamics. J Comput Neurosci 26:159-170.

Crochet S, Chauvette S, Boucetta S, Timofeev I (2005) Modulation of synaptic transmission in neocortex by network activities. Eur J Neurosci 21:1030-1044.

Cunningham MO, Pervouchine DD, Racca C, Kopell NJ, Davies CH, Jones RS, Traub RD, Whittington MA (2006) Neuronal metabolism governs cortical network response state. Proc Natl Acad Sci U S A 103:5597-5601.

D'Adamo MC, Catacuzzeno L, Di Giovanni G, Franciolini F, Pessia M (2013) K(+) channelepsy: progress in the neurobiology of potassium channels and epilepsy. Frontiers in cellular neuroscience 7:134.

D'Ambrosio R, Maris DO, Grady MS, Winn HR, Janigro D (1999) Impaired K(+) homeostasis and altered electrophysiological properties of post-traumatic hippocampal glia. J Neurosci 19:8152-8162.

D'Ambrosio R, Fender JS, Fairbanks JP, Simon EA, Born DE, Doyle DL, Miller JW (2005) Progression from frontal-parietal to mesial-temporal epilepsy after fluid percussion injury in the rat. Brain 128:174-188.

Dazzo E, Santulli L, Posar A, Fattouch J, Conti S, Loden-van Straaten M, Mijalkovic J, De Bortoli M, Rosa M, Millino C, Pacchioni B, Di Bonaventura C, Giallonardo AT, Striano S, Striano P, Parmeggiani A, Nobile C (2015) Autosomal dominant lateral temporal epilepsy (ADLTE): novel structural and single-nucleotide LGI1 mutations in families with predominant visual auras. Epilepsy Res 110:132-138.

de Curtis M, Avoli M (2016) GABAergic networks jump-start focal seizures. Epilepsia 57:679-687.

de Lanerolle NC, Lee TS, Spencer DD (2010) Astrocytes and epilepsy. Neurotherapeutics 7:424-438.

Deco G, Jirsa VK, McIntosh AR (2011) Emerging concepts for the dynamical organization of resting-state activity in the brain. Nat Rev Neurosci 12:43-56.

Deco G, Jirsa V, McIntosh AR, Sporns O, Kotter R (2009) Key role of coupling, delay, and noise in resting brain fluctuations. Proc Natl Acad Sci U S A 106:10302-10307.

Dingledine R, Gjerstad L (1980) Reduced inhibition during epileptiform activity in the in vitro hippocampal slice. The Journal of physiology 305:297-313.

Dinner D (1993) Posttraumatic epilepsy. The Treatment of Epilepsy: Principles:654-658.

Djukic B, Casper KB, Philpot BD, Chin LS, McCarthy KD (2007) Conditional knock-out of Kir4.1 leads to glial membrane depolarization, inhibition of potassium and glutamate uptake, and enhanced short-term synaptic potentiation. J Neurosci 27:11354-11365.

Dzhala VI, Talos DM, Sdrulla DA, Brumback AC, Mathews GC, Benke TA, Delpire E, Jensen FE, Staley KJ (2005) NKCC1 transporter facilitates seizures in the developing brain. Nat Med 11:1205-1213.

Echegoyen J, Neu A, Graber KD, Soltesz I (2007) Homeostatic plasticity studied using in vivo hippocampal activity-blockade: synaptic scaling, intrinsic plasticity and age-dependence. PLoS One 2:e700.

Fahoum F, Lopes R, Pittau F, Dubeau F, Gotman J (2012) Widespread epileptic networks in focal epilepsies: EEG-fMRI study. Epilepsia 53:1618-1627.

Fertziger AP, Ranck JB, Jr. (1970) Potassium accumulation in interstitial space during epileptiform seizures. Exp Neurol 26:571-585.

Filatov G, Krishnan GP, Rulkov NF, Bazhenov M (2011) Dynamics of epileptiform activity in mouse hippocampal slices. J Biol Phys 37:347-360.

Forrest MD (2014) The sodium-potassium pump is an information processing element in brain computation. Front Physiol 5:472.

Fragoso-Veloz J, Massieu L, Alvarado R, Tapia R (1990) Seizures and wet-dog shakes induced by 4-aminopyridine, and their potentiation by nifedipine. Eur J Pharmacol 178:275-284.

Friedman A, Kaufer D, Heinemann U (2009) Blood-brain barrier breakdown-inducing astrocytic transformation: novel targets for the prevention of epilepsy. Epilepsy Res 85:142-149.

Frohlich F, Bazhenov M (2006) Coexistence of tonic firing and bursting in cortical neurons. Phys Rev E Stat Nonlin Soft Matter Phys 74:031922.

Frohlich F, Bazhenov M, Sejnowski TJ (2008a) Pathological effect of homeostatic synaptic scaling on network dynamics in diseases of the cortex. J Neurosci 28:1709-1720.

Frohlich F, Sejnowski TJ, Bazhenov M (2010) Network bistability mediates spontaneous transitions between normal and pathological brain states. J Neurosci 30:10734-10743.

Frohlich F, Bazhenov M, Timofeev I, Sejnowski TJ (2005) Maintenance and termination of neocortical oscillations by dynamic modulation of intrinsic and synaptic excitability. Thalamus Relat Syst 3:147-156.

Frohlich F, Bazhenov M, Iragui-Madoz V, Sejnowski TJ (2008b) Potassium dynamics in the epileptic cortex: new insights on an old topic. Neuroscientist 14:422-433.

Frohlich F, Bazhenov M, Timofeev I, Steriade M, Sejnowski TJ (2006) Slow state transitions of sustained neural oscillations by activity-dependent modulation of intrinsic excitability. J Neurosci 26:6153-6162.

Fukunaga M, Horovitz SG, van Gelderen P, de Zwart JA, Jansma JM, Ikonomidou VN, Chu R, Deckers RH, Leopold DA, Duyn JH (2006) Large-amplitude, spatially correlated fluctuations in BOLD fMRI signals during extended rest and early sleep stages. Magn Reson Imaging 24:979-992.

Gaitatzis A, Trimble MR, Sander JW (2004) The psychiatric comorbidity of epilepsy. Acta Neurol Scand 110:207-220.

Galvan M, Grafe P, ten Bruggencate G (1982) Convulsant actions of 4-aminopyridine on the guinea-pig olfactory cortex slice. Brain Res 241:75-86.

Ghosh A, Rho Y, McIntosh AR, Kotter R, Jirsa VK (2008) Noise during rest enables the exploration of the brain's dynamic repertoire. PLoS Comput Biol 4:e1000196.

Giaume C, Koulakoff A, Roux L, Holcman D, Rouach N (2010) Astroglial networks: a step further in neuroglial and gliovascular interactions. Nat Rev Neurosci 11:87-99.

Goel A, Lee HK (2007) Persistence of experience-induced homeostatic synaptic plasticity through adulthood in superficial layers of mouse visual cortex. J Neurosci 27:6692-6700.

González OC, Krishnan GP, Chauvette S, Timofeev I, Sejnowski T, Bazhenov M (2015) Modeling of Age-Dependent Epileptogenesis by Differential Homeostatic Synaptic Scaling. The Journal of Neuroscience 35:13448-13462.

González OC, Shiri Z, Krishnan GP, Myers TL, Williams S, Avoli M, Bazhenov M (2018) Role of KCC2-dependent potassium efflux in 4-Aminopyridine-induced Epileptiform synchronization. Neurobiol Dis 109:137-147.

Grand L, Ftomov S, Timofeev I (2013) Long-term synchronized electrophysiological and behavioral wireless monitoring of freely moving animals. Journal of neuroscience methods 212:237-241.

Grasse DW, Karunakaran S, Moxon KA (2013) Neuronal synchrony and the transition to spontaneous seizures. Experimental neurology 248:72-84.

Greicius M (2008) Resting-state functional connectivity in neuropsychiatric disorders. Curr Opin Neurol 21:424-430.

Greicius MD, Krasnow B, Reiss AL, Menon V (2003) Functional connectivity in the resting brain: a network analysis of the default mode hypothesis. Proc Natl Acad Sci U S A 100:253-258.

Greicius MD, Supekar K, Menon V, Dougherty RF (2009) Resting-state functional connectivity reflects structural connectivity in the default mode network. Cereb Cortex 19:72-78.

Greicius MD, Kiviniemi V, Tervonen O, Vainionpaa V, Alahuhta S, Reiss AL, Menon V (2008) Persistent default-mode network connectivity during light sedation. Hum Brain Mapp 29:839-847.

Grisar T, Guillaume D, Delgado-Escueta AV (1992) Contribution of Na+,K(+)-ATPase to focal epilepsy: a brief review. Epilepsy Res 12:141-149.

Gupta L, Janssens R, Vlooswijk MC, Rouhl RP, de Louw A, Aldenkamp AP, Ulman S, Besseling RM, Hofman PA, van Kranen-Mastenbroek VH, Hilkman DM, Jansen JF, Backes WH (2017) Towards prognostic biomarkers from BOLD fluctuations to differentiate a first epileptic seizure from new-onset epilepsy. Epilepsia 58:476-483.

Gustafsson B, Galvan M, Grafe P, Wigstrom H (1982) A transient outward current in a mammalian central neurone blocked by 4-aminopyridine. Nature 299:252-254.

Haj-Yasein NN, Jensen V, Vindedal GF, Gundersen GA, Klungland A, Ottersen OP, Hvalby O, Nagelhus EA (2011) Evidence that compromised K+ spatial buffering contributes to the epileptogenic effect of mutations in the human Kir4.1 gene (KCNJ10). Glia 59:1635-1642.

Hamidi S, Avoli M (2015) KCC2 function modulates in vitro ictogenesis. Neurobiol Dis 79:51-58.

He BJ, Snyder AZ, Zempel JM, Smyth MD, Raichle ME (2008) Electrophysiological correlates of the brain's intrinsic large-scale functional architecture. Proc Natl Acad Sci U S A 105:16039-16044.

Heinemann U, Lux HD (1977) Ceiling of stimulus induced rises in extracellular potassium concentration in the cerebral cortex of cat. Brain Res 120:231-249.

Hernandez TD (1997) Preventing post-traumatic epilepsy after brain injury: weighing the costs and benefits of anticonvulsant prophylaxis. Trends in pharmacological sciences 18:59-62.

Heuser K, Eid T, Lauritzen F, Thoren AE, Vindedal GF, Tauboll E, Gjerstad L, Spencer DD, Ottersen OP, Nagelhus EA, de Lanerolle NC (2012) Loss of perivascular Kir4.1 potassium channels in the sclerotic hippocampus of patients with mesial temporal lobe epilepsy. J Neuropathol Exp Neurol 71:814-825.

Hiltunen T, Kantola J, Abou Elseoud A, Lepola P, Suominen K, Starck T, Nikkinen J, Remes J, Tervonen O, Palva S, Kiviniemi V, Palva JM (2014) Infra-slow EEG fluctuations are correlated with resting-state network dynamics in fMRI. J Neurosci 34:356-362.

Honey CJ, Kotter R, Breakspear M, Sporns O (2007) Network structure of cerebral cortex shapes functional connectivity on multiple time scales. Proc Natl Acad Sci U S A 104:10240-10245.

Hou Q, Zhang D, Jarzylo L, Huganir RL, Man HY (2008) Homeostatic regulation of AMPA receptor expression at single hippocampal synapses. Proc Natl Acad Sci U S A 105:775-780.

Houweling AR, Bazhenov M, Timofeev I, Steriade M, Sejnowski TJ (2005) Homeostatic synaptic plasticity can explain post-traumatic epileptogenesis in chronically isolated neocortex. Cereb Cortex 15:834-845.

Huberfeld G, Blauwblomme T, Miles R (2015) Hippocampus and epilepsy: Findings from human tissues. Rev Neurol (Paris) 171:236-251.

Huberfeld G, Wittner L, Clemenceau S, Baulac M, Kaila K, Miles R, Rivera C (2007) Perturbed chloride homeostasis and GABAergic signaling in human temporal lobe epilepsy. J Neurosci 27:9866-9873.

Hutchison RM, Womelsdorf T, Gati JS, Everling S, Menon RS (2013a) Resting-state networks show dynamic functional connectivity in awake humans and anesthetized macaques. Hum Brain Mapp 34:2154-2177.

Hutchison RM, Womelsdorf T, Allen EA, Bandettini PA, Calhoun VD, Corbetta M, Della Penna S, Duyn JH, Glover GH, Gonzalez-Castillo J, Handwerker DA, Keilholz S, Kiviniemi V, Leopold DA, de Pasquale F, Sporns O, Walter M, Chang C (2013b) Dynamic functional connectivity: promise, issues, and interpretations. Neuroimage 80:360-378.

Ibata K, Sun Q, Turrigiano GG (2008) Rapid synaptic scaling induced by changes in postsynaptic firing. Neuron 57:819-826.

Ingram J, Zhang C, Cressman JR, Hazra A, Wei Y, Koo YE, Ziburkus J, Kopelman R, Xu J, Schiff SJ (2014) Oxygen and seizure dynamics: I. Experiments. J Neurophysiol 112:205-212.

Jaerve A, Schiwy N, Schmitz C, Mueller HW (2011) Differential effect of aging on axon sprouting and regenerative growth in spinal cord injury. Exp Neurol 231:284-294.

Jensen MS, Yaari Y (1997) Role of intrinsic burst firing, potassium accumulation, and electrical coupling in the elevated potassium model of hippocampal epilepsy. J Neurophysiol 77:1224-1233.

Jin X, Prince DA, Huguenard JR (2006) Enhanced excitatory synaptic connectivity in layer v pyramidal neurons of chronically injured epileptogenic neocortex in rats. J Neurosci 26:4891-4900.

Jin X, Huguenard JR, Prince DA (2011) Reorganization of inhibitory synaptic circuits in rodent chronically injured epileptogenic neocortex. Cereb Cortex 21:1094-1104.

Jyoti A, Sethi P, Sharma D (2009) Aging accelerates the progression and manifestation of seizures in post-traumatic model of epilepsy. Neuroscience letters 453:86-91.

Kager H, Wadman WJ, Somjen GG (2000) Simulated seizures and spreading depression in a neuron model incorporating interstitial space and ion concentrations. J Neurophysiol 84:495-512.

Keller JB, Hedden T, Thompson TW, Anteraper SA, Gabrieli JD, Whitfield-Gabrieli S (2015) Resting-state anticorrelations between medial and lateral prefrontal cortex: association with working memory, aging, and individual differences. Cortex 64:271-280.

Khader P, Schicke T, Roder B, Rosler F (2008) On the relationship between slow cortical potentials and BOLD signal changes in humans. Int J Psychophysiol 67:252-261.

Kjaerby C, Rasmussen R, Andersen M, Nedergaard M (2017) Does Global Astrocytic Calcium Signaling Participate in Awake Brain State Transitions and Neuronal Circuit Function? Neurochem Res 42:1810-1822.

Kobayashi E, Bagshaw AP, Benar CG, Aghakhani Y, Andermann F, Dubeau F, Gotman J (2006) Temporal and extratemporal BOLD responses to temporal lobe interictal spikes. Epilepsia 47:343-354.

Kollevold T (1976) Immediate and early cerebral seizures after head injuries. Part I. Journal of the Oslo city hospitals 26:99-114.

Krishnamoorthy ES, Trimble MR, Blumer D (2007) The classification of neuropsychiatric disorders in epilepsy: a proposal by the ILAE Commission on Psychobiology of Epilepsy. Epilepsy Behav 10:349-353.

Krishnan GP, Bazhenov M (2011) Ionic dynamics mediate spontaneous termination of seizures and postictal depression state. J Neurosci 31:8870-8882.

Krishnan GP, Filatov G, Shilnikov A, Bazhenov M (2015) Electrogenic properties of the Na(+)/K(+) ATPase control transitions between normal and pathological brain states. J Neurophysiol 113:3356-3374.

Kusmierczak M, Lajeunesse F, Grand L, Timofeev I (2015) Changes in long-range connectivity and neuronal reorganization in partial cortical deafferentation model of epileptogenesis. Neuroscience 284:153-164.

Larson-Prior LJ, Zempel JM, Nolan TS, Prior FW, Snyder AZ, Raichle ME (2009) Cortical network functional connectivity in the descent to sleep. Proc Natl Acad Sci U S A 106:4489-4494.

Lascano AM, Korff CM, Picard F (2016) Seizures and Epilepsies due to Channelopathies and Neurotransmitter Receptor Dysfunction: A Parallel between Genetic and Immune Aspects. Mol Syndromol 7:197-209.

Lee KF, Soares C, Beique JC (2014) Tuning into diversity of homeostatic synaptic plasticity. Neuropharmacology 78:31-37.

Lemieux M, Chen JY, Lonjers P, Bazhenov M, Timofeev I (2014) The impact of cortical deafferentation on the neocortical slow oscillation. J Neurosci 34:5689-5703.

Lennie P (2003) The cost of cortical computation. Curr Biol 13:493-497.

Leslie KR, Nelson SB, Turrigiano GG (2001) Postsynaptic depolarization scales quantal amplitude in cortical pyramidal neurons. J Neurosci 21:RC170.

Levesque M, Salami P, Behr C, Avoli M (2013) Temporal lobe epileptiform activity following systemic administration of 4-aminopyridine in rats. Epilepsia 54:596-604.

Levesque M, Herrington R, Hamidi S, Avoli M (2016) Interneurons spark seizure-like activity in the entorhinal cortex. Neurobiol Dis 87:91-101.

Liao W, Zhang Z, Pan Z, Mantini D, Ding J, Duan X, Luo C, Lu G, Chen H (2010) Altered functional connectivity and small-world in mesial temporal lobe epilepsy. PLoS One 5:e8525.

Liao W, Zhang Z, Pan Z, Mantini D, Ding J, Duan X, Luo C, Wang Z, Tan Q, Lu G, Chen H (2011) Default mode network abnormalities in mesial temporal lobe epilepsy: a study combining fMRI and DTI. Hum Brain Mapp 32:883-895.

Librizzi L, Losi G, Marcon I, Sessolo M, Scalmani P, Carmignoto G, de Curtis M (2017) Interneuronal network activity at the onset of seizure-like events in entorhinal cortex slices. The Journal of Neuroscience.

Lillis KP, Kramer MA, Mertz J, Staley KJ, White JA (2012) Pyramidal cells accumulate chloride at seizure onset. Neurobiol Dis 47:358-366.

Lommatzsch M, Zingler D, Schuhbaeck K, Schloetcke K, Zingler C, Schuff-Werner P, Virchow JC (2005) The impact of age, weight and gender on BDNF levels in human platelets and plasma. Neurobiology of aging 26:115-123.

Longden TA, Dabertrand F, Koide M, Gonzales AL, Tykocki NR, Brayden JE, Hill-Eubanks D, Nelson MT (2017) Capillary K(+)-sensing initiates retrograde hyperpolarization to increase local cerebral blood flow. Nat Neurosci 20:717-726.

Lopantsev V, Avoli M (1998) Participation of GABAA-mediated inhibition in ictallike discharges in the rat entorhinal cortex. J Neurophysiol 79:352-360.

Lorincz ML, Geall F, Bao Y, Crunelli V, Hughes SW (2009) ATP-dependent infra-slow (<0.1 Hz) oscillations in thalamic networks. PLoS One 4:e4447.

Lui S, Ouyang L, Chen Q, Huang X, Tang H, Chen H, Zhou D, Kemp GJ, Gong Q (2008) Differential interictal activity of the precuneus/posterior cingulate cortex revealed by resting state functional MRI at 3T in generalized vs. partial seizure. J Magn Reson Imaging 27:1214-1220.

Lukawski K, Andres-Mach M, Czuczwar M, Luszczki JJ, Kruszynski K, Czuczwar SJ (2018) Mechanisms of epileptogenesis and preclinical approach to antiepileptogenic therapies. Pharmacol Rep 70:284-293.

Mainen ZF, Sejnowski TJ (1996) Influence of dendritic structure on firing pattern in model neocortical neurons. Nature 382:363-366.

McCreery DB, Agnew WF (1983) Changes in extracellular potassium and calcium concentration and neural activity during prolonged electrical stimulation of the cat cerebral cortex at defined charge densities. Exp Neurol 79:371-396.

Mitterdorfer J, Bean BP (2002) Potassium currents during the action potential of hippocampal CA3 neurons. J Neurosci 22:10106-10115.

Moody WJ, Futamachi KJ, Prince DA (1974) Extracellular potassium activity during epileptogenesis. Exp Neurol 42:248-263.

Nadkarni S, Arnedo V, Devinsky O (2007) Psychosis in epilepsy patients. Epilepsia 48 Suppl 9:17-19.

Nita DA, Cisse Y, Timofeev I, Steriade M (2006) Increased propensity to seizures after chronic cortical deafferentation in vivo. J Neurophysiol 95:902-913.

Nita DA, Cisse Y, Timofeev I, Steriade M (2007) Waking-sleep modulation of paroxysmal activities induced by partial cortical deafferentation. Cereb Cortex 17:272-283.

Nobile C, Michelucci R, Andreazza S, Pasini E, Tosatto SC, Striano P (2009) LGI1 mutations in autosomal dominant and sporadic lateral temporal epilepsy. Hum Mutat 30:530-536.

O'Leary T, van Rossum MC, Wyllie DJ (2010) Homeostasis of intrinsic excitability in hippocampal neurones: dynamics and mechanism of the response to chronic depolarization. The Journal of physiology 588:157-170.

Olsen ML, Sontheimer H (2008) Functional implications for Kir4.1 channels in glial biology: from K+ buffering to cell differentiation. J Neurochem 107:589-601.

Ortinski P, Meador KJ (2004) Cognitive side effects of antiepileptic drugs. Epilepsy Behav 5 Suppl 1:S60-65.

Ottman R, Winawer MR, Kalachikov S, Barker-Cummings C, Gilliam TC, Pedley TA, Hauser WA (2004) LGI1 mutations in autosomal dominant partial epilepsy with auditory features. Neurology 62:1120-1126.

Palva JM, Palva S (2012) Infra-slow fluctuations in electrophysiological recordings, blood-oxygenation-level-dependent signals, and psychophysical time series. Neuroimage 62:2201-2211.

Pan WJ, Thompson GJ, Magnuson ME, Jaeger D, Keilholz S (2013) Infraslow LFP correlates to resting-state fMRI BOLD signals. Neuroimage 74:288-297.

Patel DC, Tewari BP, Chaunsali L, Sontheimer H (2019) Neuron-glia interactions in the pathophysiology of epilepsy. Nat Rev Neurosci 20:282-297.

Pathak D, Guan D, Foehring RC (2016) Roles of specific Kv channel types in repolarization of the action potential in genetically identified subclasses of pyramidal neurons in mouse neocortex. J Neurophysiol 115:2317-2329.

Payne JA, Rivera C, Voipio J, Kaila K (2003) Cation-chloride co-transporters in neuronal communication, development and trauma. Trends Neurosci 26:199-206.

Pedley TA, Fisher RS, Futamachi KJ, Prince DA (1976) Regulation of extracellular potassium concentration in epileptogenesis. Fed Proc 35:1254-1259.

Pedley TA, Fisher RS, Moody WJ, Futamachi KJ, Prince DA (1974) Extracellular potassium activity during epileptogenesis: a comparison between neocortex and hippocampus. Trans Am Neurol Assoc 99:41-45.

Perucca E, Tomson T (2011) The pharmacological treatment of epilepsy in adults. Lancet Neurol 10:446-456.

Perucca P, Gilliam FG (2012) Adverse effects of antiepileptic drugs. Lancet Neurol 11:792-802.

Picchioni D, Horovitz SG, Fukunaga M, Carr WS, Meltzer JA, Balkin TJ, Duyn JH, Braun AR (2011) Infraslow EEG oscillations organize large-scale cortical-subcortical interactions during sleep: a combined EEG/fMRI study. Brain Res 1374:63-72.

Ping X, Jin X (2016) Chronic Posttraumatic Epilepsy following Neocortical Undercut Lesion in Mice. PLoS One 11:e0158231.

Poskanzer KE, Yuste R (2016) Astrocytes regulate cortical state switching in vivo. Proc Natl Acad Sci U S A 113:E2675-2684.

Pozo K, Goda Y (2010) Unraveling mechanisms of homeostatic synaptic plasticity. Neuron 66:337-351.

Prince DA, Tseng GF (1993) Epileptogenesis in chronically injured cortex: in vitro studies. J Neurophysiol 69:1276-1291.

Pumain R, Kurcewicz I, Louvel J (1983) Fast extracellular calcium transients: involvement in epileptic processes. Science 222:177-179.

Raichle ME (2010) Two views of brain function. Trends Cogn Sci 14:180-190.

Raichle ME (2011) The restless brain. Brain Connect 1:3-12.

Raichle ME (2015) The restless brain: how intrinsic activity organizes brain function. Philos Trans R Soc Lond B Biol Sci 370.

Raichle ME, Mintun MA (2006) Brain work and brain imaging. Annu Rev Neurosci 29:449-476.

Remme MW, Wadman WJ (2012) Homeostatic scaling of excitability in recurrent neural networks. PLoS Comput Biol 8:e1002494.

Rich MM, Wenner P (2007) Sensing and expressing homeostatic synaptic plasticity. Trends Neurosci 30:119-125.

Rivera C, Voipio J, Kaila K (2005) Two developmental switches in GABAergic signalling: the K+-Cl- cotransporter KCC2 and carbonic anhydrase CAVII. The Journal of physiology 562:27-36.

Rivera C, Voipio J, Thomas-Crusells J, Li H, Emri Z, Sipila S, Payne JA, Minichiello L, Saarma M, Kaila K (2004) Mechanism of activity-dependent downregulation of the neuron-specific K-Cl cotransporter KCC2. J Neurosci 24:4683-4691.

Rivera C, Li H, Thomas-Crusells J, Lahtinen H, Viitanen T, Nanobashvili A, Kokaia Z, Airaksinen MS, Voipio J, Kaila K, Saarma M (2002) BDNF-induced TrkB activation down-regulates the K+-Cl- cotransporter KCC2 and impairs neuronal Cl- extrusion. J Cell Biol 159:747-752.

Rutherford LC, Nelson SB, Turrigiano GG (1998) BDNF has opposite effects on the quantal amplitude of pyramidal neuron and interneuron excitatory synapses. Neuron 21:521-530.

Ruusuvuori E, Li H, Huttu K, Palva JM, Smirnov S, Rivera C, Kaila K, Voipio J (2004) Carbonic anhydrase isoform VII acts as a molecular switch in the development of synchronous gamma-frequency firing of hippocampal CA1 pyramidal cells. J Neurosci 24:2699-2707.

Salazar AM, Jabbari B, Vance SC, Grafman J, Amin D, Dillon JD (1985) Epilepsy after penetrating head injury. I. Clinical correlates: a report of the Vietnam Head Injury Study. Neurology 35:1406-1414.

Salin P, Tseng GF, Hoffman S, Parada I, Prince DA (1995) Axonal sprouting in layer V pyramidal neurons of chronically injured cerebral cortex. J Neurosci 15:8234-8245.

Schauwecker PE, Cheng HW, Serquinia RM, Mori N, McNeill TH (1995) Lesion-induced sprouting of commissural/associational axons and induction of GAP-43 mRNA in hilar and CA3 pyramidal neurons in the hippocampus are diminished in aged rats. J Neurosci 15:2462-2470.

Scheeringa R, Fries P, Petersson KM, Oostenveld R, Grothe I, Norris DG, Hagoort P, Bastiaansen MC (2011) Neuronal dynamics underlying high- and low-frequency EEG oscillations contribute independently to the human BOLD signal. Neuron 69:572-583.

Schulte U, Thumfart JO, Klocker N, Sailer CA, Bildl W, Biniossek M, Dehn D, Deller T, Eble S, Abbass K, Wangler T, Knaus HG, Fakler B (2006) The epilepsy-linked Lgi1 protein assembles into presynaptic Kv1 channels and inhibits inactivation by Kvbeta1. Neuron 49:697-706.

Schwartzkroin PA, Prince DA (1980) Changes in excitatory and inhibitory synaptic potentials leading to epileptogenic activity. Brain Res 183:61-76.

Seiffert E, Dreier JP, Ivens S, Bechmann I, Tomkins O, Heinemann U, Friedman A (2004) Lasting blood-brain barrier disruption induces epileptic focus in the rat somatosensory cortex. J Neurosci 24:7829-7836.

Seigneur J, Timofeev I (2010) Synaptic impairment induced by paroxysmal ionic conditions in neocortex. Epilepsia 52:132-139.

Sessolo M, Marcon I, Bovetti S, Losi G, Cammarota M, Ratto GM, Fellin T, Carmignoto G (2015) Parvalbumin-Positive Inhibitory Interneurons Oppose Propagation But Favor Generation of Focal Epileptiform Activity. J Neurosci 35:9544-9557.

Shen K, Hutchison RM, Bezgin G, Everling S, McIntosh AR (2015) Network structure shapes spontaneous functional connectivity dynamics. J Neurosci 35:5579-5588.

Shiri Z, Manseau F, Levesque M, Williams S, Avoli M (2016) Activation of specific neuronal networks leads to different seizure onset types. Ann Neurol 79:354-365.

Singh B, Ogiwara I, Kaneda M, Tokonami N, Mazaki E, Baba K, Matsuda K, Inoue Y, Yamakawa K (2006) A Kv4.2 truncation mutation in a patient with temporal lobe epilepsy. Neurobiol Dis 24:245-253.

Somjen GG (2002) Ion regulation in the brain: implications for pathophysiology. Neuroscientist 8:254-267.

Somjen GG, Kager H, Wadman WJ (2008) Computer simulations of neuron-glia interactions mediated by ion flux. J Comput Neurosci 25:349-365.

Steinhauser C, Seifert G, Bedner P (2012) Astrocyte dysfunction in temporal lobe epilepsy: K+ channels and gap junction coupling. Glia 60:1192-1202.

Stewart TH, Eastman CL, Groblewski PA, Fender JS, Verley DR, Cook DG, D'Ambrosio R (2010) Chronic dysfunction of astrocytic inwardly rectifying K+ channels specific to the neocortical epileptic focus after fluid percussion injury in the rat. J Neurophysiol 104:3345-3360.

Sun Q, Turrigiano GG (2011) PSD-95 and PSD-93 play critical but distinct roles in synaptic scaling up and down. J Neurosci 31:6800-6808.

Szaflarski JP, Nazzal Y, Dreer LE (2014) Post-traumatic epilepsy: current and emerging treatment options. Neuropsychiatric disease and treatment 10:1469-1477.

Temkin NR (2003) Risk factors for posttraumatic seizures in adults. Epilepsia 44 Suppl 10:18-20.

Temkin NR (2009) Preventing and treating posttraumatic seizures: the human experience. Epilepsia 50 Suppl 2:10-13.

Temkin NR, Haglund MM, Winn HR (1995) Causes, prevention, and treatment of post-traumatic epilepsy. New horizons 3:518-522.

Thimm J, Mechler A, Lin H, Rhee S, Lal R (2005) Calcium-dependent open/closed conformations and interfacial energy maps of reconstituted hemichannels. J Biol Chem 280:10646-10654.

Tian GF, Azmi H, Takano T, Xu Q, Peng W, Lin J, Oberheim N, Lou N, Wang X, Zielke HR, Kang J, Nedergaard M (2005) An astrocytic basis of epilepsy. Nat Med 11:973-981.

Tian L, Jiang T, Liu Y, Yu C, Wang K, Zhou Y, Song M, Li K (2007) The relationship within and between the extrinsic and intrinsic systems indicated by resting state correlational patterns of sensory cortices. Neuroimage 36:684-690.

Timofeev I, Steriade M (2004) Neocortical seizures: initiation, development and cessation. Neuroscience 123:299-336.

Timofeev I, Grenier F, Steriade M (2002a) The role of chloride-dependent inhibition and the activity of fast-spiking neurons during cortical spike-wave electrographic seizures. Neuroscience 114:1115-1132.

Timofeev I, Bazhenov M, Sejnowski T, Steriade M (2002b) Cortical hyperpolarization-activated depolarizing current takes part in the generation of focal paroxysmal activities. Proceedings of the National Academy of Sciences of the United States of America 99:9533-9537.

Timofeev I, Bazhenov M, Avramescu S, Nita DA (2010) Posttraumatic epilepsy: the roles of synaptic plasticity. Neuroscientist 16:19-27.

Timofeev I, Bazhenov M, Seigneur J, Sejnowski T (2012) Neuronal Synchronization and Thalamocortical Rhythms in Sleep, Wake and Epilepsy. In: Jasper's Basic Mechanisms of the Epilepsies (th, Noebels JL, Avoli M, Rogawski MA, Olsen RW, Delgado-Escueta AV, eds). Bethesda (MD).

Timofeev I, Grenier F, Bazhenov M, Sejnowski TJ, Steriade M (2000) Origin of slow cortical oscillations in deafferented cortical slabs. Cereb Cortex 10:1185-1199.

Timofeev I, Sejnowski TJ, Bazhenov M, Chauvette S, Grand LB (2013) Age dependency of trauma-induced neocortical epileptogenesis. Frontiers in cellular neuroscience 7:154.

Topolnik L, Steriade M, Timofeev I (2003a) Hyperexcitability of intact neurons underlies acute development of trauma-related electrographic seizures in cats in vivo. Eur J Neurosci 18:486-496.

Topolnik L, Steriade M, Timofeev I (2003b) Partial cortical deafferentation promotes development of paroxysmal activity. Cereb Cortex 13:883-893.

Toyoda I, Fujita S, Thamattoor AK, Buckmaster PS (2015) Unit activity of hippocampal interneurons before spontaneous seizures in an animal model of temporal lobe epilepsy. Journal of Neuroscience 35:6600-6618.

Trasande CA, Ramirez JM (2007) Activity deprivation leads to seizures in hippocampal slice cultures: is epilepsy the consequence of homeostatic plasticity? J Clin Neurophysiol 24:154-164.

Traynelis SF, Dingledine R (1988) Potassium-induced spontaneous electrographic seizures in the rat hippocampal slice. J Neurophysiol 59:259-276.

Turrigiano GG (2008) The self-tuning neuron: synaptic scaling of excitatory synapses. Cell 135:422-435.

Ullah G, Cressman JR, Jr., Barreto E, Schiff SJ (2009) The influence of sodium and potassium dynamics on excitability, seizures, and the stability of persistent states. II. Network and glial dynamics. J Comput Neurosci 26:171-183.

Uva L, Breschi GL, Gnatkovsky V, Taverna S, de Curtis M (2015) Synchronous inhibitory potentials precede seizure-like events in acute models of focal limbic seizures. J Neurosci 35:3048-3055.

van Vliet EA, da Costa Araujo S, Redeker S, van Schaik R, Aronica E, Gorter JA (2007) Blood-brain barrier leakage may lead to progression of temporal lobe epilepsy. Brain 130:521-534.

Vanhatalo S, Palva JM, Holmes MD, Miller JW, Voipio J, Kaila K (2004) Infraslow oscillations modulate excitability and interictal epileptic activity in the human cortex during sleep. Proc Natl Acad Sci U S A 101:5053-5057.

Viitanen T, Ruusuvuori E, Kaila K, Voipio J (2010) The K+-Cl cotransporter KCC2 promotes GABAergic excitation in the mature rat hippocampus. The Journal of physiology 588:1527-1540.

Volman V, Bazhenov M, Sejnowski TJ (2011a) Pattern of trauma determines the threshold for epileptic activity in a model of cortical deafferentation. Proc Natl Acad Sci U S A 108:15402-15407.

Volman V, Sejnowski TJ, Bazhenov M (2011b) Topological basis of epileptogenesis in a model of severe cortical trauma. J Neurophysiol 106:1933-1942.

Wallraff A, Kohling R, Heinemann U, Theis M, Willecke K, Steinhauser C (2006) The impact of astrocytic gap junctional coupling on potassium buffering in the hippocampus. J Neurosci 26:5438-5447.

Watanabe M, Fukuda A (2015) Development and regulation of chloride homeostasis in the central nervous system. Frontiers in cellular neuroscience 9:371.

Wei Y, Ullah G, Schiff SJ (2014a) Unification of neuronal spikes, seizures, and spreading depression. J Neurosci 34:11733-11743.

Wei Y, Ullah G, Ingram J, Schiff SJ (2014b) Oxygen and seizure dynamics: II. Computational modeling. J Neurophysiol 112:213-223.

Wierenga CJ, Ibata K, Turrigiano GG (2005) Postsynaptic expression of homeostatic plasticity at neocortical synapses. J Neurosci 25:2895-2905.

Xiong W, Ping X, Gao J, Jin X (2011) Preparing undercut model of posttraumatic epileptogenesis in rodents. J Vis Exp.

Yamaguchi S, Rogawski MA (1992) Effects of anticonvulsant drugs on 4-aminopyridine-induced seizures in mice. Epilepsy Res 11:9-16.

Yekhlef L, Breschi GL, Lagostena L, Russo G, Taverna S (2015) Selective activation of parvalbumin- or somatostatin-expressing interneurons triggers epileptic seizurelike activity in mouse medial entorhinal cortex. J Neurophysiol 113:1616-1630.

Zhang D, Raichle ME (2010) Disease and the brain's dark energy. Nat Rev Neurol 6:15-28.

Zhang Z, Lu G, Zhong Y, Tan Q, Liao W, Wang Z, Wang Z, Li K, Chen H, Liu Y (2010a) Altered spontaneous neuronal activity of the default-mode network in mesial temporal lobe epilepsy. Brain Res 1323:152-160.

Zhang Z, Lu G, Zhong Y, Tan Q, Chen H, Liao W, Tian L, Li Z, Shi J, Liu Y (2010b) fMRI study of mesial temporal lobe epilepsy using amplitude of low-frequency fluctuation analysis. Hum Brain Mapp 31:1851-1861.

Ziburkus J, Cressman JR, Schiff SJ (2013) Seizures as imbalanced up states: excitatory and inhibitory conductances during seizure-like events. J Neurophysiol 109:1296-1306.

Zuckermann EC, Glaser GH (1968) Hippocampal epileptic activity induced by localized ventricular perfusion with high-potassium cerebrospinal fluid. Exp Neurol 20:87-110.